GOLD NANOPARTICLES AS CONTRAST AGENTS FOR NONLINEAR MICROSCOPY

NAVEEN KUMAR BALLA
(*B.Tech, Indian Institute of Technology Madras*)

A THESIS SUBMITTED

FOR THE DEGREE OF DOCTOR OF PHILOSOPHY

IN COMPUTATION AND SYSTEMS BIOLOGY (CSB)

SINGAPORE-MIT ALLIANCE

NATIONAL UNIVERSITY OF SINGAPORE

2012

DECLARATION

I hereby declare that this thesis is my original work and it has been written by me in its entirety. I have duly acknowledged all the sources of information which have been used in the thesis.

This thesis has also not been submitted for any degree in any university previously

Naveen Kumar Balla
25 October 2012

Acknowledgements

I started my doctoral studies with almost no knowledge of optics. All I knew about light at that time was its speed, 299792458 m/s in vacuum. I memorized this number from my physics course at high school and later used it as a password. But I have enjoyed the five and half years of my grad life. I was fortunate to meet some wonderful people during this time who were kind and helpful. This is right opportunity to express my gratitude towards them.

Firstly, I would like to thank my supervisors Prof. Sheppard and Prof. So for their guidance and patience. They gave me enough time to explore and learn things on my own. Prof. Sheppard spent most of his time with us in lab, explaining to us various optical phenomena and how they link with one another. His passion for research was a great source of inspiration for us. Prof. So is a great experimentalist. Though I spent only a short time with him in lab, I greatly benefited from his knowledge about optical instrumentation. His guidance in design and execution of experiments was valuable.

During my doctoral studies, I learnt a lot of experimental skills from people at lab. Elijah, Fa Ke, Dimitrios and Shakil frequently helped me with the optical set-up. Wai Teng and Shalin helped me with Matlab coding. Sounderya helped me with cell culture work and antibody conjugation. Anupama taught me gold nanorod synthesis. I would like thank these people and all others at the two labs.

I would also like thank my big family back in India who has been very supportive all these years. I would like to specially thank my parents and my sister for believing in me.

I am grateful to Prof Jerome Mertz for his valuable comments on my manuscript.

Finally I would like to thank SMA for the financial support and SMA office staff for helping us out with the paper work from time to time.

Table of Contents

Chapter 1: Introduction

Chapter 2: Discrete Dipole Approximation for Second harmonic Scattering

Chapter 3: Comparison between Coupled and Uncoupled Dipole Models for Nonlinear Scattering.

Chapter 4: Bio-inspired nano contrast agents for second harmonic generation microscopy

Chapter 5: Surface Modification and Multiphoton Luminescence Microscopy of Gold Nanorods

Summary

Gold nanoparticles interact strongly with visible and near infrared wavelengths because of their shape dependent plasmon resonance. These nanoparticles can be potential contrast agents for nonlinear optical microscopy. But nonlinear scattering from small particles with different shapes is difficult to predict by analytical methods. We have developed a numerical method which assumes the scatterer to be made of dipoles. In our model, the dipoles of a scatterer interact with each other and with external radiation. Previous dipole models for nonlinear scattering failed to take into account interaction between the dipoles. We show here that the dipole coupling is necessary for predicting the effects of shape and size of a nanoparticle on its nonlinear optical properties. The coupling between dipoles increases with increase in the magnitude of refractive index of the scatterer. Similarly dipole coupling becomes important in regions where there is a sharp change in refractive index like edges.

Gold nanoparticles synthesized by wet chemistry are generally symmetric in shape and therefore they are not good candidates of second harmonic generation (SHG). The coupled dipole model was used to design and optimize a gold nano-helix for SHG. For a given excitation wavelength, the geometry of the helix can be tuned to yield maximum SHG. The gold nano-helix was found to be 65 times better than a comparable gold nanorod

for SHG. The approach for designing SHG scatterers can be extended to any other type nonlinear scattering.

A generic methodology for modifying the surface of gold nanoparticles was developed. Gold nanorods were used as sample gold nanoparticles. Gold nanorods were coated with PEG to keep them stable in biological buffers. The nanorods were conjugated with antibodies to target specific cell types. The concentration of the antibody on the gold nanorods was optimized to reduce non-specific binding. Multiphoton luminescence (MPL) microscope was used for imaging gold nanorods targeted to cancer cells. When gold nanorods with longitudinal plasmon resonance (LPR) close to the laser wavelength (824 nm) were used, the nanorods got heated up very quickly even with 1 mW of excitation power. But when long excitation wavelengths (1200 nm) were used, the heating of nanorods was significantly reduced and this allowed imaging for longer period of time. Therefore longer excitation wavelengths, away from LPR of nanorods might be a better choice for MPL microscopy of gold nanorods.

List of Figures

List of Abbreviations

3D	Three dimensional
2PF	Two photon fluorescence
3PF	Three photon fluorescence
CARS	Coherent anti-Stokes Raman scattering
SHG	Second harmonic generation
THG	Third harmonic generation
PSF	Point spread function
NA	Numerical aperture
OCT	Optical coherence tomography
HRS	Hyper Rayleigh scattering
DDA	Discrete dipole approximation
CDM	Coupled dipole model
PDM	Polarizable dipole model
UDM	Uncoupled dipole model
NIR	Near infrared
TMV	Tobacco mosaic virus
CPMV	Cowpea mosaic virus
LPR	Longitudinal plasmon resonance
MPL	Multiphoton luminescence
PEG	Polyethylene glycol
CTAB	Cetyl trimethylammonium bromide
DD	Double distilled
SKBM	Skeletal myoblasts
DMEM	Dubelco's modified eagle's medium
PBS	Phosphate buffer saline
EGFR	Epidermal growth factor receptor
BSA	Bovine serum albumin

List of Symbols

a	Absorption coefficient
I	Intensity
$\mathbf{n}$	Refractive index
$\mathbf{p}$	Molecular polarization
$\boldsymbol{\alpha}$	Molecular polarizability of first order
$\boldsymbol{\beta}$	Molecular polarizability of second order or first hyperpolarizability
$\boldsymbol{\gamma}$	Molecular polarizability of third order or second hyperpolarizability
$\mathbf{P}$	Macroscopic polarization
$\boldsymbol{\chi}$	Susceptibility
ε_o	Permitivity of free space
$\mathbf{E}$	Electric field
k	Wave number
λ	Wavelength
C_{ext}	Extinction cross-section
C_{abs}	Absorption cross-section
J_n	Bessel function of n^{th} order

Chapter 1

Introduction

1.1 Motivation

Optical microscopy is a very important tool for biologists. It has played a key role in many biological discoveries including the discovery of cell, the fundamental unit of life. Optical microscopes are mostly non-invasive and they provide sub-cellular resolution which is sufficient for tackling most of biological problems. However, the focus of biological research is moving from single cell to collection of cells in complex three dimensional (3D) environments like tissues or small animals. Observation of cells in such environments requires microscopes which can overcome scattering by the sample and resolve objects in 3D. Scattering and absorption of light by biological specimen decrease as wavelength increases [1]. But longer wavelengths decrease the resolution of a microscope. Nonlinear optical microscopy is one of the solutions to this multi-faceted problem. Nonlinear optical microscopes use near-infrared excitation that can penetrate deeper into biological specimens. The nonlinear interaction of light with the sample provides high resolution in 3D.

Another important challenge for optical microscopy is source of contrast in biological samples. Cells and tissues in general do not have specific optical signatures which stand out of the background. Moreover, the ability to monitor a specific component in the sample is important. Therefore external contrast agents like fluorescent dyes or nanoparticles are necessary. These contrast agents should be small enough to be able to target cells. The optical signature from these contrast agents should be strong and it should allow for long term monitoring of the samples. Hence there is a need for better contrast agent for nonlinear optical microscopy.

1.2 Nonlinear Optics

Nonlinear optical microscopy refers to a collection of microscopy techniques which rely on nonlinear interaction between light and matter. When light interacts with a material without changing the optical properties of the material, it is called a linear interaction. Nonlinear interaction, on the other hand, occurs when the optical properties of the material are transiently changed by the light itself [2]. To observe such nonlinear phenomena, a very high intensity of light is necessary and therefore almost all non-linear optics was developed after the invention of the ruby laser [3]. However, antecedents of nonlinear optics can be found in electro-optic effects like the Kerr effect [4] and the Pockels effect. In the experiments leading to the discovery of these effects, a strong electric field was used to change the optical properties of a sample and a polarized light source was used to probe the extent of these changes. After the invention of laser, researchers were able to induce changes in optical properties of some materials by using only light.

There are a number of nonlinear optical phenomena but the ones important to microscopy are two photon fluorescence (2PF), three photon fluorescence (3PF), second harmonic generation (SHG), third harmonic generation (THG) and coherent anti-Stokes Raman scattering (CARS). 2PF was described theoretically by Maria Goppert-Mayer [5] in 1931. Before Goppert-Mayer's work, it was believed that an electron could absorb only one photon to get excited to a higher energy level. The light emitted on relaxation of the excited electron to its ground state is called one (or single) photon fluorescence (1PF) (Fig. 1.1(a)). Goppert- Mayer showed that an electron can absorb two photons to get excited to a higher energy level. Two photon absorption is an intensity dependent absorption which can be described by equation (1.1).

$$a = a_0 + a_2 I. \tag{1.1}$$

where a is the total absorption coefficient, a_0 is the linear absorption coefficient, a_2 is the two photon absorption coefficient and I is the intensity of excitation light. Generally, in order for the term a_2I to be comparable in magnitude to a_0, high intensities are required. The fluorescence resulting from two photon absorption is called 2PF (Fig. 1.1(b)). The first experimental 2PF was observed from $CaF_2:Eu^{2+}$ crystals in 1961 [6]. Three photon absorption is an extension of this concept. It should be noted here that the emitted photons are completely independent of how the excitation has occurred.

The nonlinear optical phenomena like SHG, THG and CARS are types of nonlinear scattering. In SHG, two incident photons are jointly scattered by an electron to give a single photon whose energy is the sum of energies of the incident photons (Fig. 1.2). During this process, the refractive index of the sample is modulated by amplitude of the electric field (Eq. 1.2).

$$\mathbf{n} = \mathbf{n_0} + \mathbf{n_1}\mathbf{E}. \tag{1.2}$$

where $\mathbf{n}$ is the net refractive index of the material, $\mathbf{n_0}$ is the linear refractive index, $\mathbf{n_1}$ is the first order refractive index of the material and $\mathbf{E}$ is the amplitude electric field in the incident field. $\mathbf{n_0}$ and $\mathbf{n_1}$ are tensors and $\mathbf{E}$ is a vector. In scattering processes, no real energy levels are involved. Since all the energy of the incident photons is converted into energy of the emitted photon, there is no energy loss to the sample. SHG was demonstrated experimentally for the first time in 1961 [7].

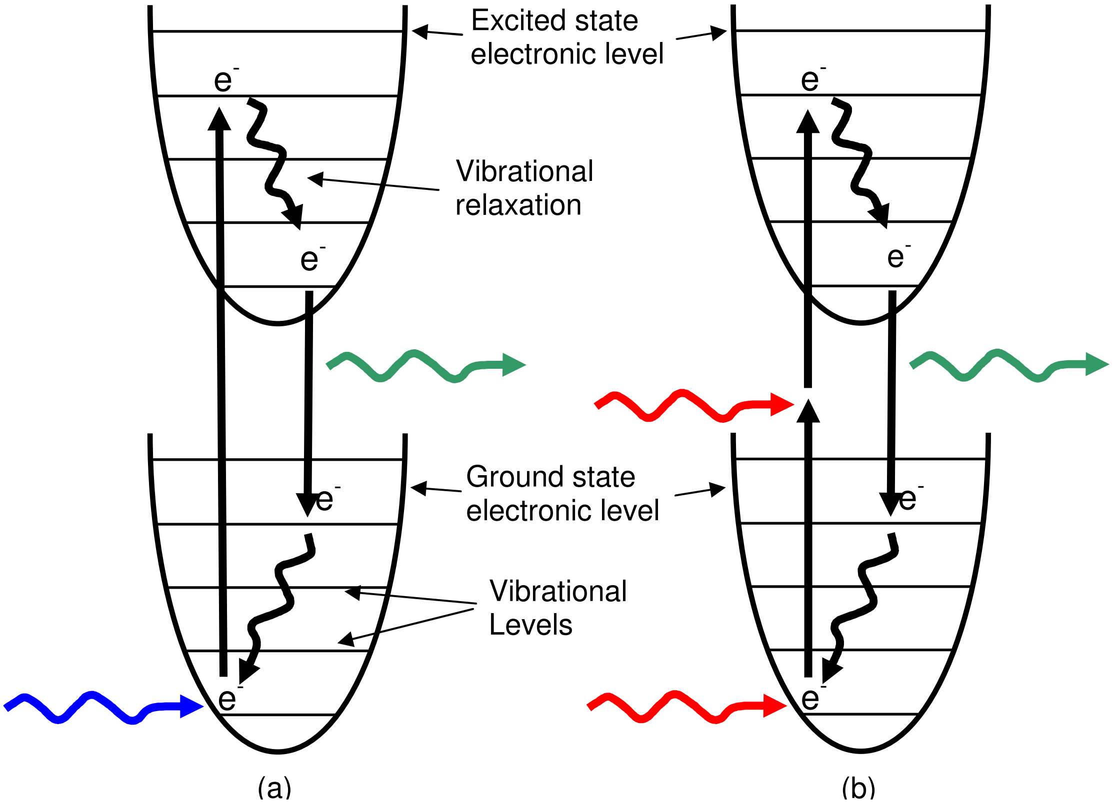

Figure 1.1. Jablonski diagram of electronic transitions during (a) one photon and (b) two photon fluorescence.

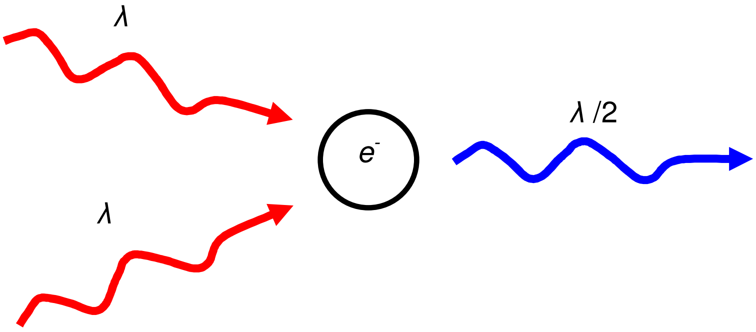

Figure. 1.2 Cartoon of second harmonic generation. λ refers to the wavelength of light. e^- represents an electron.

In any material, the elementary scatterer of light is an electron which is bound to a nucleus. The polarization induced in a single electron-nucleus pair is defined by equation (1.3):

$$\begin{aligned}\mathbf{p} &= \boldsymbol{\alpha}\mathbf{E} + \boldsymbol{\beta}\mathbf{EE} + \boldsymbol{\gamma}\mathbf{EEE} + \ldots \\ &= \mathbf{p}^{(1)} + \mathbf{p}^{(2)} + \mathbf{p}^{(3)} + \ldots\end{aligned} \tag{1.3}$$

where $\boldsymbol{\alpha}$, β and γ are first, second and third order polarizabilities of the electron-nucleus pair respectively, **E** is the incident local electric field and **p** is the induced dipole moment which includes linear dipole moment ($\mathbf{p}^{(1)}$) and the nonlinear dipole moments ($\mathbf{p}^{(2)}$, $\mathbf{p}^{(3)}$,..). This dipole moment is responsible for all scattering processes. It should be noted that all these parameters are tensors. For example, second order polarization ($\mathbf{p}^{(2)}$) which is responsible for SHG can be decomposed into its components as follows

$$\begin{bmatrix} p_x^{(2)} \\ p_y^{(2)} \\ p_z^{(2)} \end{bmatrix} = \begin{bmatrix} \beta_{xxx} & \beta_{xyy} & \beta_{xzz} & \beta_{xxy} & \beta_{xyz} & \beta_{xzx} \\ \beta_{yxx} & \beta_{yyy} & \beta_{yzz} & \beta_{yxy} & \beta_{yyz} & \beta_{yzx} \\ \beta_{zxx} & \beta_{zyy} & \beta_{zzz} & \beta_{zxy} & \beta_{zyz} & \beta_{zzx} \end{bmatrix} \begin{bmatrix} E_xE_x \\ E_yE_y \\ E_zE_z \\ E_xE_y \\ E_yE_z \\ E_zE_x \end{bmatrix}. \tag{1.4}$$

Scattering is a coherent process which implies that the scattered light has well defined phase relation with the incident photons as well as with the sample. The scattering of light, which is experimentally observed in the laboratory, is a vectorial summation from different dipoles within a sample. Therefore the structure of the sample and distribution of its optical properties play a very important role in the determining the nature of the scattered light. The macroscopic scattering observed can be described by equation (1.5) which is expressed in terms of macroscopic properties:

$$\mathbf{P} = \varepsilon_0 \left(\boldsymbol{\chi}^{(1)} + \boldsymbol{\chi}^{(2)}\mathbf{E} + \boldsymbol{\chi}^{(3)}\mathbf{EE} + \ldots \right)\mathbf{E} \;, \tag{1.5}$$

where ε_0 is the permittivity of free space, $\boldsymbol{\chi}^{(1)}$, $\boldsymbol{\chi}^{(2)}$ and $\boldsymbol{\chi}^{(3)}$ are first, second and third order susceptibilities respectively, of the scatterer. In a strict sense, the electric field **E** in equation (1.5) is not the local field but the incident electric field assuming the sample is absent. Susceptibilities are macroscopic quantities and they are related to atomic polarizabilities by a vectorial sum (Eqs.1.6-1.8):

$$\boldsymbol{\chi}^{(1)} = \frac{1}{\varepsilon_0}\sum_N \boldsymbol{\alpha}_\mathbf{i} \;, \tag{1.6}$$

$$\boldsymbol{\chi}^{(2)} = \frac{1}{\varepsilon_0}\sum_N \boldsymbol{\beta}_\mathbf{i} \;, \tag{1.7}$$

$$\chi^{(3)} = \frac{1}{\varepsilon_0}\sum_N \gamma_i \ , \tag{1.8}$$

where N is the number density of dipoles in the scatterer. The summation in equations (1.6-1.8) takes into account the spatial organization of atomic dipoles in the scatterer. As a result $\chi^{(2)}$ is zero for centrosymmetric scatterers [8]. However SHG has been observed at the surface of centrosymmetric materials [9] and theoretically explained [10]. Here it is sufficient to say that when the local field gradient is strong, SHG can be observed even in centrosymmetric scatterers. It should also be mentioned that the theory presented above is the dipole theory and the equations are presented in their simplified versions.

1.3 Nonlinear Microscopy

2PF and SHG have proved to be excellent contrast mechanisms for imaging biological specimen. The design of a nonlinear laser scanning microscope for SHG and 2PF was described by Sheppard and Kompfner [11]. The first nonlinear laser scanning microscope was a second harmonic microscope, built by Gannaway and Sheppard in 1978 [12]. In this microscope, non-linear crystals were scanned through a focused laser beam and the SHG was recorded to form image pixel-by-pixel. This set-up remains fundamentally unchanged even today, with the main difference being that a focused laser beam is scanned across static samples in most cases. The invention of femtosecond pulsed lasers with high repetition rates [13] gave a major boost to the development nonlinear microscopy. Femtosecond pulses provide high instantaneous intensities but keep the average power low. The first 2PF microscope was built in Denk and coworkers [14]. Starting in 1990s, nonlinear microscopy emerged as the most preferred imaging modality for thick biological samples. Nonlinear laser scanning microscopy has intrinsic 3D imaging ability because the signal is generated only from the focal region. Therefore, unlike a confocal microscope, there is no need for pinhole in nonlinear microscopes. This makes the design of nonlinear microscopes much simpler. The radial (*r*) and axial (*z*) point spread function (PSF) of a nonlinear microscope which uses nonlinear signal of order *n* can be calculated from equations (1.9) and (1.10) respectively [15]:

$$PSF_{radial} \propto \left[\frac{2J_1(v)}{v} \right]^{2n} \quad , \tag{1.9}$$

$$PSF_{axial} \propto \left[\frac{\sin(u/4)}{u/4} \right]^{2n}, \tag{1.10}$$

where $v = k\,NA\,r$, $u = 4\,k\,NA^2\,z$ and $k = 2\pi/\lambda$. *NA* is numerical aperture of the lens and λ is the central wavelength of excitation laser. Nonlinear microscopes use infrared lasers for excitation, which penetrate deeper into tissues. Since spatial localization is a result of the nonlinear excitation process, the signal from the depths, though highly scattered, does not have to be descanned or passed through a pinhole. Instead, the signal can be directly collected by a detector. Both these factors improve the imaging depth of nonlinear microscopes. In the case of 2PF microscope where fluorophores are involved, excitation of fluorophores occurs only in the focal region and hence photobleaching is reduced. This allows for long term imaging with minimal loss in fluorescence signal.

The ability of 2PF and SHG microscopes to image deeper into the sample at sub-cellular resolution has contributed significantly to the development of various fields of biology [15-18]. For example, Miller and coworkers [19] used 2PF to look into a lymph node of live mice and studied interactions of lymphocytes with the antigen presenting cells. Sandoval and Molitoris [20] reviewed 2PF technique for studying the functioning of a mouse kidney. Due to relatively high transparency of brain tissue to light, 2PF has been extensively used in neurobiology [16, 21]. The technique is so benign to biological tissue that *in vivo* nonlinear microscopy has been performed on human skin [22, 23]. Unlike 2PF microscopy which mostly relies on external fluorophores for contrast, SHG microscopy mainly uses endogenous contrast in biological tissue. SHG microscopy has been used to image collagen, myosin and microtubule arrays in dividing cells [24]. Collagen type I has been extensively imaged using SHG microscopy [25, 26]. Detailed images of cornea

[27] and optic nerve head [28] were obtained because these structures are primarily made up of collagen. Diagnosis of a fibrotic liver can be performed based on second harmonic images of the liver [29]. Second harmonic imaging of cell membrane stained with polar dye molecules has also been reported [30].

1.4 **SHG Microscopy**

SHG has certain advantages over 2PF. Since no energy is absorbed in SHG, there are no issues of photo-bleaching or photo-toxicity. Therefore SHG imaging can be performed over extended periods of time with no drop in signal intensity. In 2PF, dye molecules can easily get saturated beyond a certain excitation power or pulse repetition rate. This is one of the limitations on signal intensity in 2PF microscopy. SHG microscopy does not suffer from sample saturation as no real energy levels are involved. SHG is a narrow band emission as compared to fluorescence. The narrow band of SHG is also easy to distinguish from the broad autofluorescence background in biological samples. Quantum efficiency of fluorescent dyes which emit in the red region of the spectrum is very low due to non-radiative decay. This is a serious limitation for deep tissue imaging. Red wavelengths are less scattered by tissue and therefore availability of efficient probes which emit in the red region of the spectrum is highly desirable. There is no non-radiative decay in SHG and therefore SHG probes designed for red region of the spectrum should be efficient. The main limitation for SHG and THG in the infrared region is absorption by water which increases sharply for wavelengths above 1000 nm. A new class of contrast agents for SHG microscopy has recently emerged [31]. Some inorganic nanoparticles made of metals or metal oxides have been found to be strong scatterers for SHG. Bariuam titanate ($BaTiO_3$) nanocrystals have been used as probes for *in vivo* second harmonic imaging [32, 33]. Strong SHG has been observed from zinc oxide (ZnO) nanocrystals. Individual silver nanoparticle or in groups can be strong scatterers for SHG [34]. Similarly SHG microscopy using gold particles has been reported [35].

1.5 Gold Nanoparticles

Gold nanoparticles have been extensively used as contrast agents for optical microscopy because of their superior optical properties, simple surface chemistry and biocompatibility. Gold nanoparticles, like other metallic nanoparticles, have free electrons on their surface which oscillate collectively at certain characteristic frequency surface plasmon resonance (SPR) frequency. Gold nanoparticles absorb and scatter light strongly around their SPR frequency. SPR of gold nanoparticles depend on the size. For example, the SPR of gold nanospheres shows a red shift with increase in the size of the nanospheres [36, 37]. Another way to change the SPR of gold nanoparticles is by changing the shape of the particle [38]. If we are looking at aggregates of gold nanoparticles, then again depending on the size and shape of the aggregates, the optical properties change [39]. The flexibility to tune the optical properties of gold nanoparticles make them good probes for optical microscopy. Gold, being an inert metal, does not interact with the sample. It has been shown in multiple studies than gold nanoparticles are not toxic to cells or tissues [40, 41]. Gold nanospheres (Fig. 1.3(a)) are the simplest form of gold nanoparticles. Since these particles strongly scatter light they were used as contrast agents for confocal reflectance microscopy (Fig. 1.4). Antibody conjugated gold nanospheres were used to image cancer cells in culture [42] as well as in *ex vivo* tissue [43]. Gold nanoshells (Fig. 1.3(b)) are better at scattering light in the near infrared region [44], and hence these nanoparticles have been used as contrast agents for optical coherence tomography (OCT) [45]. Gold nanorods are another kind of gold nanoparticles which exhibit strong photoluminescence [46], and these nanoparticles have been used for multiphoton luminescence microscopy [47].

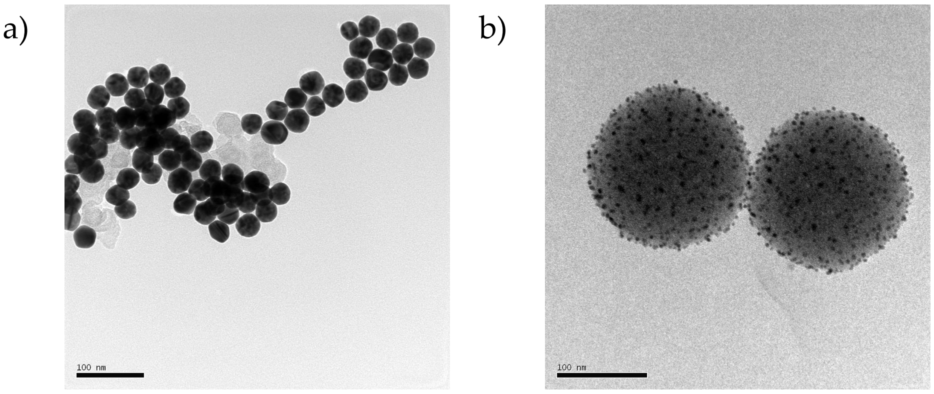

Figure 1.3. Transmission electron microscope images of gold nanospheres (a) and gold nanoshells (b).

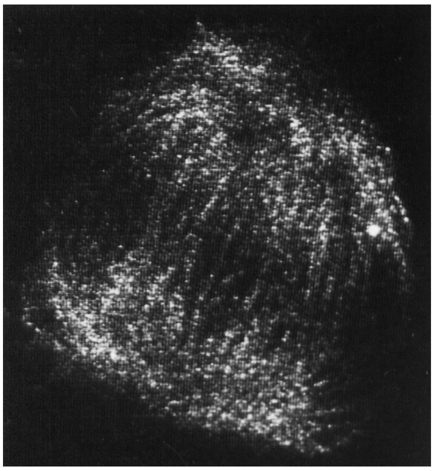

Figure 1.4. Confocal reflection image of dividing cells which have been stained with gold nanospheres (*Courtesy: Prof Colin Sheppard*).

Given the strong scattering ability of gold nanoparticles, it might appear that these nanoparticles would be promising contrast agents for SHG. Unfortunately that is not the case. Most common types of gold nanoparticles made in the laboratory have a symmetric structure that attenuates SHG. Gold nanospheres dried on a coverslip can be imaged by SHG (Fig. 1.5(a)) owing to the sharp change in refractive index at the point of contact with glass. When this difference in refractive index is reduced by adding water, the intensity of SHG drops sharply (Fig. 1.5(b)).

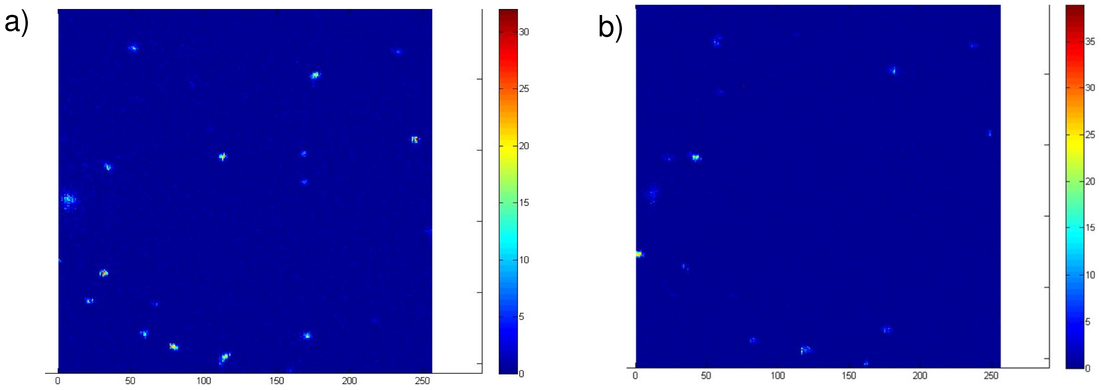

Figure 1.5. Second harmonic images of 30 nm gold nanospheres dried on a coverslip. From top the particles were (a) open to air and (b) submerged in DI water.

Similarly, nonlinear spectra of gold nanorods (Fig. 1.6) excited by femtosecond pulses centered at 800 nm show a small SHG signal at 400 nm and strong multiphoton luminescence, which includes three photon luminescence at wavelengths smaller than 400 nm and two photon luminescence at wavelengths greater than 400 nm. This spectrum was acquired from a gold nanorod suspension in a cuvette. The low magnitude of SHG can be attributed to the centrosymmetric shape of gold nanorods. If the symmetry is broken, as in a cluster of gold nanospheres (Fig. 1.7), strong SHG can be obtained. These results agree well with hyper-Rayleigh scattering results from gold nanospheres [48]. Hyper-Rayleigh scattering is an incoherent form of SHG.

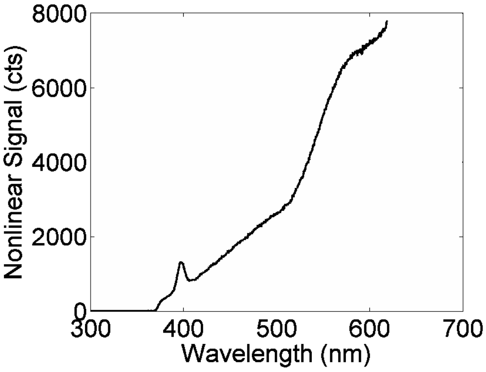

Figure 1.6. Nonlinear spectrum of gold nanorods when excited with femtosecond pulses centered around 800 nm.

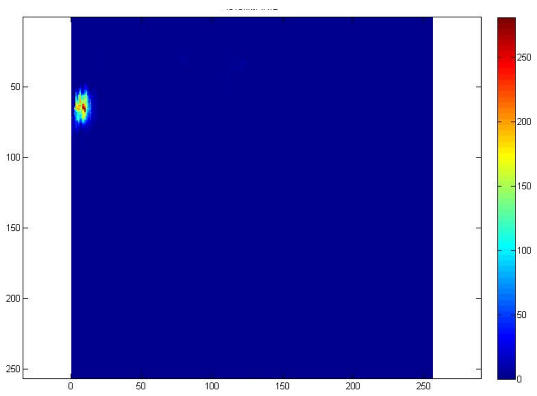

Figure 1.7 Intense second harmonic signal from a cluster of gold nanospheres. The particles lie sandwiched between two layers low melting agarose (0.5%).

1.6 Overview of Thesis

Conventional forms of gold nanoparticles are not good as contrast agents for SHG due to their symmetric structure. Therefore asymmetric gold nanoparticles are required for SHG. Such asymmetric gold nanoparticles are not readily available for experimental studies. However it is possible to theoretically design asymmetric gold nanoparticles which will strongly scatter second harmonic light. In other words, we can design artificial nonlinear molecules [49]. I have developed a numerical model to simulate nonlinear scattering from small structures of any arbitrary shape and size (Chapter 2). My numerical model is derived from Discrete Dipole Approximation (DDA) [50] and another dipole model for nonlinear scattering [30]. The previous dipole model for nonlinear scattering does not take into account interactions between dipoles. I used the concept of dipole coupling from DDA to create a new dipole model for nonlinear scattering. I have shown that my model can be used for different types nonlinear scattering and that it gives better predictions than the previous model (Chapter 3). Using my model I have proposed the design of a chiral gold nanoparticle which will be a strong scatterer for SHG (Chapter 4). The design of this scatterer is based on a biological scaffold which makes the structure very robust. Further, using gold nanorods I have developed methodology to functionalize gold nanoparticles of any kind (Chapter 5). I have also demonstrated multiphoton luminescence of cancer cells targeted with functionalized gold nanorods.

Chapter 2

Discrete Dipole Approximation for Second Harmonic Scattering

2.1 Introduction

The scattering of light by small particles has been an active area of research for over a century. The initial light scattering problems focused primarily on spherical particles but with the progress made by materials scientists and chemists it is possible to synthesize small particles with different shapes, in different sizes and in complex assemblies [38]. Light scattered by a particle depends on various factors – wavelength of the light, refractive index of the particle relative to its surroundings, the particle's shape, size and orientation, and distribution (intensity, direction and polarization) of the incident light. A simple a computational model for light scattering that can readily account for these factors has become all the more important. The most common form of light scattering is linear scattering where there is no change in the frequency of scattered light and the scattered light intensity is directly proportional to the incident light intensity. However we are interested nonlinear scattering of light because of its applications to bioimaging as discussed in chapter 1. Nonlinear optical properties, specifically second harmonic generation (SHG) from small particles are highly dependent on the particle geometry. It is well known that under the dipolar approximation, SHG is forbidden from a centrosymmetric medium. At an interface where this symmetry breaks, SHG can be observed. However, in the case of spherical particles which are small relative to the excitation wavelength, SHG generated from one part of the particle surface is cancelled out by SHG generated from the other parts of the particle surface. An expression for second order polarization in a centrosymmetric medium, proposed by Adler [51], forms the basis of most bulk models of SHG from small spheres. Agarwal and Jha [52] proposed the first model for SHG from small metal spheres, predicting a dipolar bulk response and a quadrupolar surface response from the particles. Others have taken into account the dynamics of electrons within a small sphere [53, 54] to predict its second harmonic scattering properties. SHG from an array of quantum dots was calculated by modeling each quantum dot as a particle in a box which is being perturbed by excitation light [55]. All the above works consider the bulk of the particle as a source of SHG. The surface of a spherical particle can also cause SHG provided the particle is not small as compared to the excitation wavelength or if the excitation field is not uniform across the particle. Under such conditions, the phase of the incident wave changes significantly as it travels across the particle. As a result the surface SHG does not exactly cancel out. The theory of SHG from small spheres under inhomogeneous illumination has been reported [56, 57]. For spherical particles whose size is comparable to the excitation wavelength, the charge induced on the surface by incident light can give rise to higher harmonics [58]. Polar molecules immobilized on the surface of small polystyrene beads, when excited scatter second harmonic light which is polarized and has a specific angular distribution [59-61]. Second harmonic response from small spheres with arbitrary surface response was calculated by Dadap *et al.* [62, 63]. All these analytical models give us an insight into the interaction of light with small particles. While these models are important, they are restricted to spherical particles in a relatively homogeneous environment. With the increasing importance of non-spherical metal nanoparticles being recognized [64-66], it is necessary to have a computational frame work that can efficiently predict the SHG properties of these non-spherical particles. In addition to particle geometry, the illumination conditions may also be far from simple with significant field gradient or complex polarization distribution. To add to this complexity, the local environment of the nanoparticles may be heterogeneous, especially for biomedical applications. Numerical methods are better equipped to solve these problems.

Here we use a numerical method called the discrete dipole approximation (DDA) [67] to calculate second harmonic scattering properties of small particles. This method was formulated to simulate linear scattering and absorption by interstellar dust particles [67, 68]. In DDA, a scatterer is assumed to be made up of small polarizable dipoles (Fig. 2.1) which interact among themselves and with the external field. The optical properties of the scatterer are given by the summation of the optical properties of all the constituent dipoles. Draine and coworkers developed an efficient Fourier transforms based algorithm for DDA to facilitate fast computation of scattered fields by particles of various geometries [50, 69]. The algorithm is implemented in FORTRAN language and it is available as a free program - DDSCAT[70]. Hoekstra *et al.* developed a parallel computing version of DDA which made it possible to simulate light scattering by large particles [71, 72]. DDA has been used in different areas of research but with different names, like the coupled dipole method (CDM) [73] and the polarizable dipole model (PDM) [74].

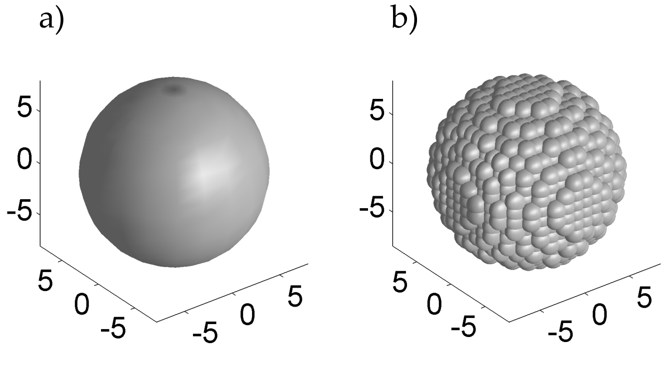

Figure 2.1. Approximation of a sphere (a) as an arrangement of sub-volumes on a cubic lattice (b). Each sub-volume behaves as an individual dipole.

One of the main advantages of DDA is its ability to handle arbitrary shapes of scatterers. The method is easy to implement and it is computationally undemanding. Although DDA was developed for materials with moderate magnitudes of refractive index, it can be used to calculate scattering properties of metal nanoparticles which have high magnitudes of refractive index [75]. The results predicted in the far field and in the highly sensitive near field regions agree well with results from other numerical methods. As such, it has been extensively used to calculate linear optical properties of noble metal nanoparticles, especially for non-spherical shapes, clusters of nanoparticles and nanoparticles in heterogeneous local environments [39, 76-78]. DDA has also been adapted to calculate scattering by a wide variety of objects like periodic scatterers [79], photonic crystals [80], magnetic nanoparticles [81], metamaterials [82] and blood cells [83]. Apart from scattering, this method has also been used to calculate optical forces on nanoparticles [84]. All these applications of DDA consider linear interaction of light with matter. We have shown here that by taking into account nonlinear interaction between light and matter, DDA can be extended to predict nonlinear optical scattering from small particles. We have formulated the relevant mathematical expressions to calculate second harmonic scattering from small particles of different kinds. We compared our computational results with experimental results reported earlier.

2.2 Theory

When a nanoparticle is excited by an electromagnetic wave, a strong near field is created around the particle. This strong field is ideal for nonlinear interaction of light and matter. DDA has been used to calculate field enhancement around nanoparticles [76] but nonlinear scattering from small particles using this method has never been reported. We have achieved this by extending the DDA to calculate induced nonlinear dipoles within small particles when excited by light. Here we briefly describe the linear model and then extend it to the nonlinear regime. To begin with, a scatterer can be assumed to be made up of *N* small sub-volumes which are arranged on a cubic lattice. If $\mathbf{E}_{inc,i}$ is the incident field and $\mathbf{P}^{(1)}_i$ is the first order polarization induced at the center of the *i*th sub-volume, then these quantities are related by equation (2.1):

$$\mathbf{P}_i^{(1)} = \boldsymbol{\alpha}_{i,\omega}\left(\mathbf{E}_{inc,i}^{(1)} - \sum_{j\neq i}^{N}\mathbf{A}_{ij}^{(1)}\mathbf{P}_j^{(1)}\right). \qquad (2.1)$$

The superscript in braces refers to the order of the process. $\boldsymbol{\alpha}_{i,\omega}$ is the linear polarizability of the *i*th dipole at angular frequency ω. $\mathbf{A}^{(1)}_{ij}$ is the term defining interaction between *i*th and *j*th dipoles at frequency ω. If $\mathbf{r}_i$ is the position vector of the i^{th} dipole, then the expression for $\mathbf{A}^{(1)}{}_{ij}$ is given by equation (2.2):

$$\left.\begin{aligned}
&\mathbf{A}_{ij}^{(1)}\mathbf{P}_j^{(1)} = \frac{\exp(ikr_{ij})}{r_{ij}^{\;3}}\Big[k^2\mathbf{r}_{ij}\times(\mathbf{r}_{ij}\times\mathbf{P}_j^{(1)}) + \\
&\quad \frac{(1-ikr_{ij})}{r_{ij}^{\;2}}\left\{r_{ij}^{\;2}\mathbf{P}_j^{(1)} - 3\mathbf{r}_{ij}\left(\mathbf{r}_{ij}.\mathbf{P}_j^{(1)}\right)\right\}\Big],\ \text{for } j \neq i; \\
&\mathbf{A}_{ij}^{(1)} = \boldsymbol{\alpha}_{i,\omega}^{\;\;-1},\ \text{for } j = i.
\end{aligned}\right\}, \tag{2.2}$$

where $k = \omega/v$, ω and v being angular frequency and velocity respectively, of the incident light in the ambient medium; $\mathbf{r}_{ij} = \mathbf{r}_i - \mathbf{r}_j$ and $r_{ij} = |\mathbf{r}_i - \mathbf{r}_j|$. By combining $\mathbf{A}^{(1)}{}_{ij}$ and $\mathbf{A}^{(1)}{}_{ii}$ terms we can define $\mathbf{A}$ matrix and rewrite equation (1) in a compact form (Eq. 2.3):

$$\sum_{j=1}^{N}\mathbf{A}_{ij}^{(1)}\mathbf{P}_j^{(1)} = \mathbf{E}_{inc,i}^{(1)}. \tag{2.3}$$

Finding exact solution to Eq. (2.3) is a challenging task because of the large size of matrix **A**. But approximate solutions to this equation can be calculated by various forms of conjugate gradient methods which are fast in finding solutions to reasonable accuracy [85, 86]. Once the induced dipole moments are known, the scattered field is given by superposition of the individual dipoles fields. One can also calculate extinction cross-section (C_{ext}) and absorption cross-section (C_{abs}) of the scatterer [68].

$$C_{ext} = \frac{4\pi k}{|\mathbf{E}_{inc}|^2} \sum_{j=1}^{N} \mathrm{Im}(\mathbf{E}_{inc,j}^{(1)*}.\mathbf{P}_j^{(1)}) \ . \tag{2.4}$$

$$C_{abs} = \frac{4\pi k}{|\mathbf{E}_{inc}|^2} \sum_{j=1}^{N} \left[\mathrm{Im}\left\{ \mathbf{P}_j^{(1)} \cdot (\alpha_j^{-1})^* \mathbf{P}_j^{(1)*} \right\} - (2/3) k^3 |\mathbf{P}_j^{(1)}|^2 \right] \ . \tag{2.5}$$

All the above equations describe the linear phenomena and we have reproduced them here for the purpose of clarity. We extended this dipole approximation from Eq. (2.1) to calculate nonlinear scattering by the scatterer. Linear local field at a dipole can be derived from the linear polarizability induced at that dipole (Eq. 2.6):

$$\begin{aligned} \mathbf{E}_{loc,i}^{(1)} &= \boldsymbol{\alpha}_i^{-1} \mathbf{P}_i^{(1)}, \\ &= \left(\mathbf{E}_{inc,i} - \sum_{j \neq i}^{N} \mathbf{A}_{ij} \mathbf{P}_j^{(1)} \right) \ . \end{aligned} \tag{2.6}$$

This linear local field is the actual driving force for the various orders of polarization. Typically, we neglect the higher orders of local field relative to the first order local field because they are comparatively much smaller in magnitude. Since we are interested in second harmonic scattering, we focused on the second order polarization, $\mathbf{P}^{(2)}$. If $\boldsymbol{\beta}_i$ is the first hyperpolarizability of the i^{th} sub-volume, then

$$\mathbf{P}_i^{(2)} = \boldsymbol{\alpha}_{i,2\omega}\left(\boldsymbol{\alpha}_{i,2\omega}^{-1}\boldsymbol{\beta}_i\mathbf{E}_{loc,i}^{(1)}\mathbf{E}_{loc,i}^{(1)} - \sum_{j\neq i}^{N}\mathbf{A}_{ij}^{(2)}\mathbf{P}_j^{(2)}\right), \tag{2.7}$$

$$\sum_{j=1}^{N}\mathbf{A}_{ij}^{(2)}\mathbf{P}_j^{(2)} = \boldsymbol{\alpha}_{i,2\omega}^{-1}\boldsymbol{\beta}_i\mathbf{E}_{loc,i}^{(1)}\mathbf{E}_{loc,i}^{(1)} \ . \tag{2.8}$$

Equation (2.8) differs from equation (2.3) mainly in the driving force for the induced polarizations, which appears on the right hand side of these equations. For the second harmonic polarization, the driving force is proportional to the square of the linear local field weighted by first hyperpolarizability tensor. It should also be noted that the interaction term $\mathbf{A}^{(2)}_{ij}$ in equations (2.7) and (2.8) is a function of the second harmonic wave number and not the excitation wave number. Incidentally, similar models for SHG from surfaces were reported by Wijers *et al.* [87] and Poliakov *et al.* [88]. Wijers *et al.* assumed a silicon wafer surface to be made up of 20-80 stacked layers where each layer acts as a dipole. In Wijers' model, the geometry is simple – a linear arrangement of dipoles. On the other hand, Poliakov *et al.* [40] used their model to calculate various types of induced nonlinear polarization in molecules adsorbed on rough metallic surfaces. The present work, however, differs from these two earlier reports because here we have focused on far field second harmonic scattering properties of nanoparticles of different types and geometries. Shape and size of a nanoparticle play important roles in its second order optical properties and we have demonstrated this effect by means of simple examples. We have also shown here that our method can be used for nanoparticle composites. Another dipole model [30, 89] worth mentioning here considers the dipoles to be independent of each other and driven only by the incident field. This model can be termed as uncoupled dipole model and it is an approximation to our nonlinear coupled dipole model. The coupled dipole model is a two step improvement of the uncoupled dipole model. The coupled dipole model first takes into account the corrected linear local field rather than the incident field itself. Then it calculates the corrected second order polarization rather than obtaining it directly by squaring the linear local field.

Since our model is an extension of DDA, it can be used for scatterers of random shapes. The dipole size (d) should be such that the $|m|kd < 1$, where m is the refractive index of the scatterer and k wave number of the scattering wavelength involved. In the case of nonlinear scattering, multiple wavelengths are involved and therefore, we should consider the wavelength for which $|m|k$ is maximum. This ensures that the dipole size is good for all other wavelengths. In our case, the second harmonic wavelength is the smallest wavelength. The size of the dipole should also be small enough to roughly approximate the shape of the scatterer. This criterion is difficult to quantify, especially when the shape of the scatterer is irregular. The refractive index of gold nanoparticles was obtained from Blanchard *et al.* [90]. The exact value of hyperpolarizability ($\boldsymbol{\beta}$) of gold is not known. However we can say that the surface of the particle is asymmetric and hence hyperpolarizability for dipoles on the surface is non-zero. We have considered only one component ($\boldsymbol{\beta}_{surf,\perp\perp\perp}$) of the hyperpolarizability tensor which acts on the electric field normal to the surface ($\mathbf{E}_{loc,surf,\perp}$) and yields a second order polarization in the same direction [91]:

$$\begin{aligned} \boldsymbol{\beta}_{bulk} &= 0 , \\ \boldsymbol{\beta}_{surf} &= \boldsymbol{\beta}_{surf,\perp\perp\perp} \neq 0 . \end{aligned} \tag{2.9}$$

2.3 Results & discussion

Based on the algorithm proposed by Draine and coworkers [69], we have developed a MATLAB code to implement the nonlinear DDA model. Second harmonic scattering from a nanosphere is widely discussed in literature. Therefore it is good sample scatterer to test our model. We calculated the distribution of scattered second harmonic light from a gold nanosphere of 15 nm diameter. The excitation source is a plane polarized wave of wavelength 800 nm, polarized along x-axis and propagating along positive z-axis. The nanosphere is located at the origin of the coordinate axes and it is assumed to be made up of dipoles which are 1 nm apart on a cubic lattice. We calculated the induced second order dipole moments ($\mathbf{P}^{(2)}{}_i$'s) and the scattered second harmonic field was calculated from these dipoles.

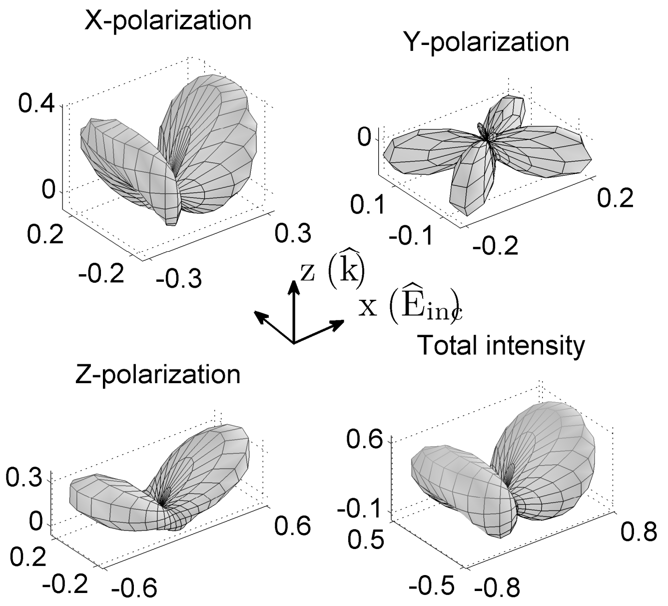

Figure 2.2. Spatial distribution of scattered second harmonic light from a 14nm gold nanosphere when excited by plane polarized light.

The three polarization components (*x*, *y* and *z*) and the total intensity of the scattered second harmonic field are represented on a polar plot (Fig. 2.2). The distance from the origin represents the magnitude of second harmonic scattering in a given orientation. The magnitudes have been normalized with the maximum intensity value to give an estimate of relative strengths of field components. These results are in good agreement with the theoretical analysis of second harmonic scattering from small spherical particles reported earlier [63].

Extending our work to a less trivial case, we applied this DDA formalism to calculate the SHG from non-spherical scatterers. Although DDA models a scatterer as a collection of dipoles, the overall scattering depends on the geometry of the scatterer among other factors. The geometry of the scatterer influences the interaction between the dipoles and therefore the overall scattering profile is a superposition of various multipoles such as a dipole, quadrupole and so on. This is clearly evident in the hyper Rayleigh scattering (HRS) experiments on gold and silver nanospheres [92, 93]. In our experimental setup incident light propagates along the positive z-axis. The polarization of the incident light is rotated in the xy plane and the polarization angle was measured with respect to the positive x-axis. At each incident polarization angle, the intensity of x-polarized scattered second harmonic light from a suspension of nanospheres was measured along the y-axis. Figure (2.3) is schematic of the hypothetical set up.

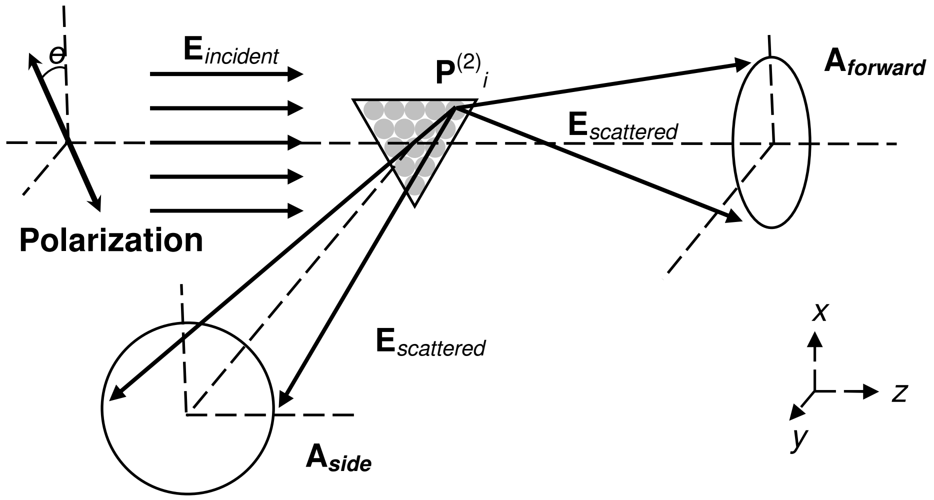

Figure 2.3. Schematic of hypothetical set-up where scattering from a scatterer is measured over a forward aperture ($A_{forward}$) and a side aperture (A_{side}).

In this schematic, a triangular scatter is represented to highlight the fact that shape is not a constraint. The triangular scatterer is approximated by a collection of dipoles and the scattering of each dipole in a desired direction is calculated. In the real experiments, small metal nanospheres are not perfectly spherical. Due to this asymmetry in shape, the scattered second harmonic light is predominantly dipolar in nature as long as the nanospheres are small. With increase in size of a nanosphere, retardation effects make the quadrupolar scattering stronger than the dipolar scattering. A finite element analysis of this HRS experiment showed that even small metal nanoparticles which are perfectly spherical in shape show quadrupolar scattering but a slight deviation from spherical shape in these small metal nanoparticles gives rise to a dipolar scattering [91]. The perfect spherical shape leads to a cancellation of dipolar scattering. Therefore, quadrupolar scattering, though weak in small nanoparticles, shows up. In metal nanoparticles which are not perfectly spherical, the dipolar behavior dominates as long as the nanoparticle is small. With increasing size, the quadrupolar behavior becomes stronger than the dipolar behavior. We simulated these HRS experiments using our nonlinear DDA model. In figure (2.4) we show the effect of shape of a nanoparticle on the scattered second harmonic light. The samples were a gold nanosphere, 16 nm in diameter and two types of nanorods, each 12 nm in diameter but with lengths of 14 nm and 16 nm. To account for the free rotation of the particle in a suspension, we averaged the intensity of scattered second harmonic light over six different orientations of the particle for each incident polarization angle. These six directions correspond to axes joining the six diametrically opposite pairs of vertices in an icosahedron. Since an icosahedron is one of the five Platonic solids, its vertices sample the entire solid angle of 4π equally. Figure (2.4) shows the strength of x-polarized second harmonic light, calculated along positive y-axis, as we change the polarization angle of incident light in the xy-plane. The second harmonic scattering from nanospheres is predominantly quadrupolar in nature. On the other hand, second harmonic scattering from the gold nanorods tends to be dipolar with increasing aspect ratio of the rods.

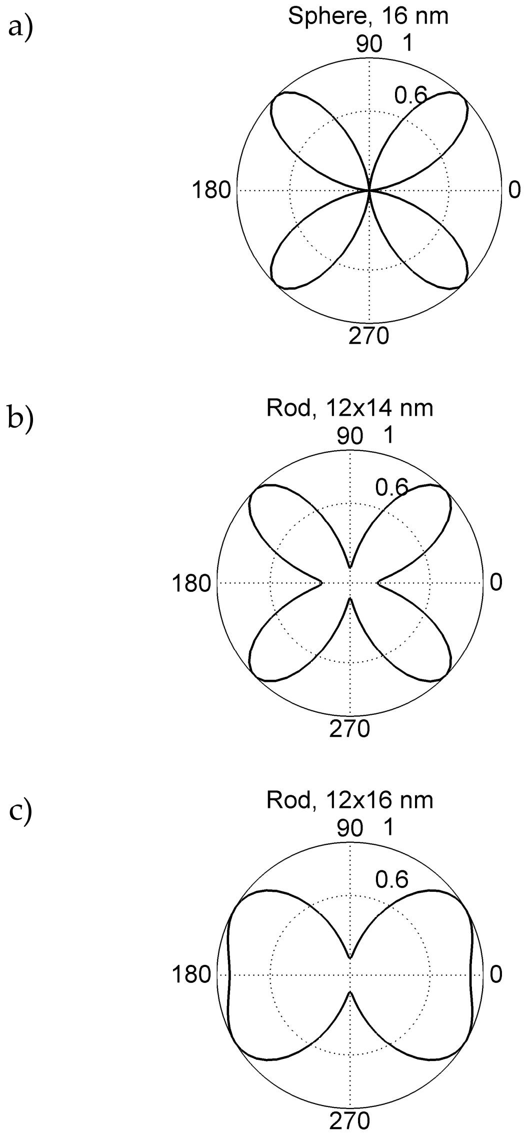

Figure 2.4. Distribution of *x*-polarized second harmonic scattering from nanosphere and two types of nanorods with different aspect ratios as a function of the incident polarization angle with respect to the *x*-axis. The scattered second harmonic light intensity was calculated along *y*-axis and the incident light was propagating along positive *z*-axis.

To compare our results with experimental results, we simulated HRS experiments on silver nanospheres [93]. The excitation wavelength was set at 780 nm. Scattering samples were silver nanospheres of diameters 40 nm, 60 nm and 80 nm. To match the experimental conditions closely our simulated nanospheres should have all forms of surface and bulk asymmetries which occur in silver nanospheres used for experiments. This, however, is not possible because of the large number of asymmetries. Therefore we used just one asymmetry [91], elongation in one direction, for all three sizes of nanospheres. With increase in size of the spheres, the degree of asymmetry decreases and the quadrupolar behavior dominates as can be seen in second harmonic scattering patterns (Fig. 2.5). All these results are in good agreement with the experimental results [93] and numerical simulations [91].

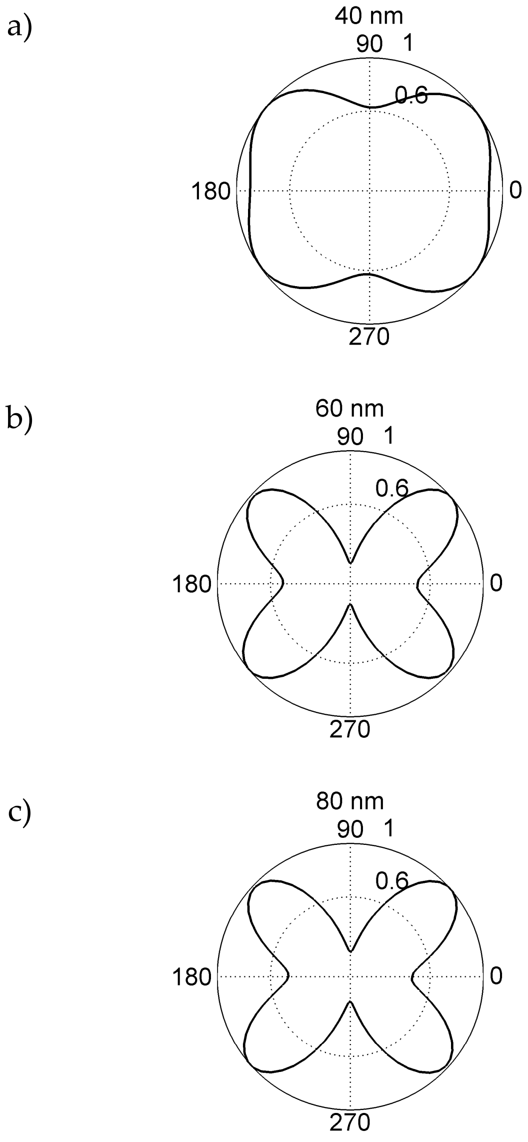

Fig. 2.5. Distribution of x-polarized second harmonic scattering from silver nanospheres of diameters 40 nm (a), 60nm (b) and 80 (c) nm as a function of the incident polarization angle with respect to the x-axis. The scattered second harmonic light intensity was calculated along y-axis and the incident light was propagating along positive z-axis.

So far we have compared the results from our model with theoretical and experimental results for metal nanoparticles. But our model can also predict nonlinear scattering from dielectric particles. Yang *et al.* [61] reported

HRS from a water suspension of polystyrene beads which were coated with malachite green molecules. They used polystyrene beads of 510 nm, 700 nm and 980 nm in diameter and measured position dependent *p*-polarized second harmonic scattering for *s*- and *p*-polarized incident light. In Yang's experiments, the detector was rotated about the sample from the positive *z*-direction ($+\hat{\mathbf{k}}$) to the negative *z*-direction ($-\hat{\mathbf{k}}$) to measure the spatial distribution of HRS. To test our model, we simulated these experiments using polystyrene beads of diameters 510 nm, 680 nm and 986 nm. The incident wavelength was set at 840 nm to match the experimental conditions. Owing to the low refractive index of polystyrene, we set the distance between dipoles as 17 nm. The excitation light can be either *s*- or *p*-polarized, and the second harmonic scattering is a combination of *s*- and *p*-polarizations. The experimental results [61] show that for *p*-polarized excitation, the *p*-polarized HRS becomes more forward directed with increase in size of the beads (Fig. 2.6). It was also reported that the *p*-polarized HRS becomes weaker and spatially less localized when the polarization of excitation light is changed from *p* to *s* (Fig. 2.6).

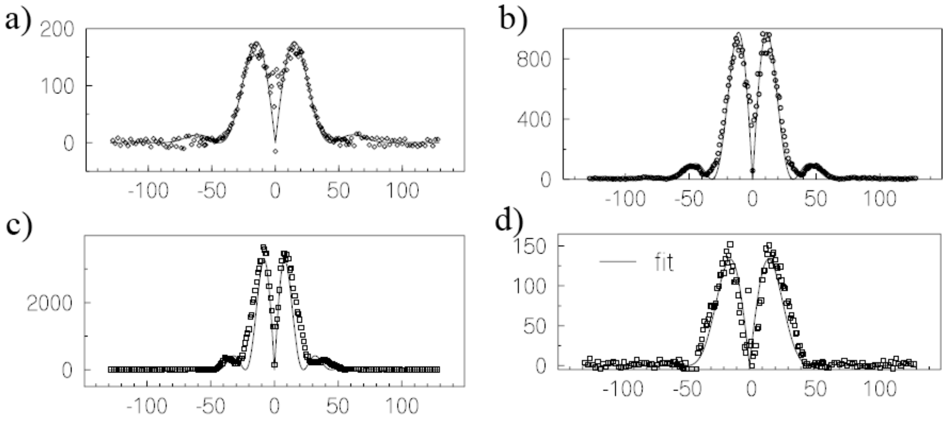

Figure 2.6. Angular distribution of *p*-polarized HRS from polystyrene beads coated with malachite green molecules. Size of the polystyrene beads is 510nm (a), 700nm (b & d) and 980nm (c). The exciting light is *p*-polarized in (a), (b), (c), and it is *s*-polarized in (d). The angle (θ) of the detector is zero at positive *z*-axis (+$\hat{k}$) and it goes to □180° at negative *z*-axis (-$\hat{k}$).

Reprinted figures (3) and (4) with permission from N. Yang, W. E. Angerer, and A. G. Yodh, Physical Review Letters 87, 103902 (2001). Copyright (2001) by the American Physical Society.

The results from our simulations (Fig. 2.7) agree well with the experimental results (Fig. 2.6). The angular localization of the main lobes and the first side lobes, and relative strengths of the HRS intensities match well with the experimental results [61]. For example, the magnitudes of *p*-polarized HRS from 686 nm beads when excited with *s*-polarized light and that from 510 nm beads when excited with *p*-polarized light are comparable. One aspect of our results which does not match with the Yang's results is the size of side lobes. This mismatch is partly due to the fact that the polarizability of malachite green molecules is not known quantitatively. We observed that as we increased the polarizability of the surface bound molecules, the side lobes decreased in size. But higher refractive index implies higher computational costs, especially when we have to find the right polarizability by iteration. It is possible to match the experimental results by iteratively choosing the right polarizability but due to the marginal improvement in results, we avoided this extra computational cost.

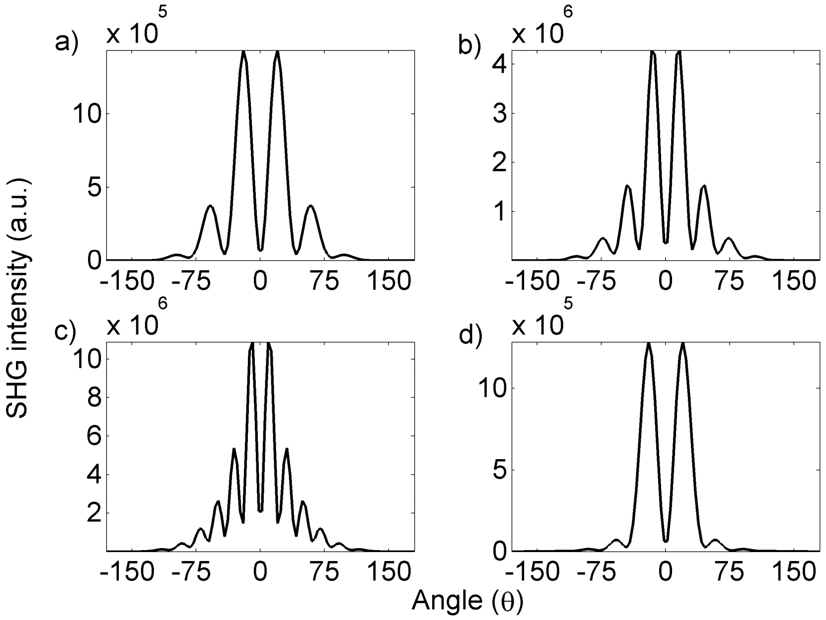

Figure 2.7. Angular distribution of *p*-polarized HRS from polystyrene beads coated with malachite green molecules. Size of the polystyrene beads is 510nm (a), 680nm (b & d) and 986nm (c). The exciting light is *p*-polarized in (a), (b), (c), and it is *s*-polarized in (d). The angle (θ) of the detector is zero at positive *z*-axis ($+\hat{\mathbf{k}}$) and it goes to □180° at negative *z*-axis ($-\hat{\mathbf{k}}$).

2.4 Conclusion

We have demonstrated that DDA is a very simple model to predict second harmonic scattering from nanoparticles of various kinds. We have shown how shape and size of nanoparticles influence their nonlinear optical properties. With increasing applications of nanoparticles in optical experiments, this method should be helpful in providing good prediction of nonlinear scattering properties. The model does not restrict itself to specific shapes of scatterers or illumination conditions. We can model a single particle as well as a collection of particles by this method. This is a first step in exploring DDA for applications in nonlinear scattering from small particles. A more detailed analysis of this method is essential. Uncoupled dipole model is a well established for nonlinear scattering and it is numerical much simpler than DDA. Therefore there is need to justify why one should undertake the extra computational effort involved in DDA. There is also a need to find a physical quantity which causes this coupling between the dipoles. Further, like the uncoupled dipole model, DDA can be easily extended to other types of nonlinear scattering. Some of these problems have been investigated in the next chapter.

Note: The contents of this chapter are based on the following paper:

N.K. Balla, P.T.C. So and C.J.R. Sheppard, "Second harmonic scattering from small particles using Discrete Dipole Approximation," Optics Express 18, 21603 (2010).

Chapter 3

Comparison between Coupled and Uncoupled Dipole Models for Nonlinear Scattering

3.1 Introduction

Nonlinear scattering of light by matter has been widely used as a tool for spectroscopy and microscopy. Second harmonic spectroscopy has been used to study liquid interfaces [94] and surfaces of small particles [95]. The three main forms of microscopy which are based on nonlinear scattering of light are second harmonic generation (SHG) microscopy, third harmonic generation (THG) microscopy and coherent anti-Stokes Raman scattering (CARS) microscopy. Nonlinear microscopy is based on endogenous contrast from the sample and therefore does not require an external contrast agent. The nonlinear effect gives 3D sectioning ability to these imaging modalities. Since there is no absorption of photons, photobleaching and photo-toxicity effects do not arise. The principle of nonlinear laser scanning microscopy was first demonstrated by Gannaway and Sheppard [12] in 1978. Under the dipole approximation SHG occurs in noncentrosymmetric structures and therefore it can be used to image chiral structures. SHG microscopy has been used for structural imaging of specially stained cell membranes [96], extracellular matrix [97], myosin [98] and collagen [24, 99, 100] in tissues. THG occurs in all types of materials but due to Gouy phase shift in a focused beam, it is appreciable only at interfaces [101]. As a result, THG microscopy has been used to study morphology of biological specimens [102, 103]. *In vivo* imaging of embryos [104-106] using THG microscopy has been successfully demonstrated by a number of groups. Apart from morphological imaging, nonlinear microscopy can also be used for vibrational imaging of samples by CARS. Unlike harmonic generation microscopy, a CARS microscopy [107, 108] uses two different beams, a pump and a Stokes beam. CARS microscopy can be used to image the distribution of bonds whose energy overlaps with energy difference between two pump photons and one Stokes photon [109]. CARS microscopy has been used to image live cells [110] and lipid droplets [111] within cells.

SHG, THG and CARS microscopy have significantly contributed to the class of 3D optical imaging modalities. Most often, these imaging modalities do not require a contrast agent but they instead rely on the properties of the sample to generate a contrast. However it should be noted that these imaging modalities are based on scattering which is fundamentally different from fluorescence, the more popular source of contrast in optical imaging. The fundamental difference between fluorescence and scattering is that the former is an incoherent process whereas the later is a coherent process. Therefore fluorescence is uniform in all directions and it is directly proportional to the concentration of the contrast agent. Scattering on the other hand is mostly directional and it is proportional to concentration of the contrast agent raised to a value which can lie anywhere between 0 and 2 [112]. The value of this exponent depends on orientation and organization of contrast agents which are simultaneously excited. Inhomogeneities in the distribution of contrast agents in a sample make the process more complicated. Therefore interpretation of results is not always simple. The dipole model introduced by Jerome Mertz and co-workers [30] has been used to study light scattering patterns in nonlinear microscopy. In this model, each scatterer is assumed to be made up of dipoles. Depending on the location and orientation of a dipole in the focal volume, its scattering properties can be calculated from the excitation field it experiences. The net scattered field is then given by coherent summation over all the dipoles present in the focal volume. The scattered field can be propagated to any location in space by using Green's function [89]. This dipole model was used to describe SHG scattering patterns from membranes of giant unilamellar vesicles [113] and from collagen fibers [25, 114]. This model has also been extended to describe THG [89] and CARS [115]. This dipole model however has certain limitations. The dipoles in a scatterer interact with one another and with the incident field. The final distribution of the excitation field is a result of this interaction. Similarly when nonlinear dipoles are induced, they interact among themselves and redistribute the net nonlinear field. This interaction is not captured by the dipole model we have discussed so far. Therefore this model can be aptly referred to as the uncoupled dipole model (UDM). The coupled dipole model (CDM) which takes into account interaction between dipoles was proposed by Purcell and Pennypacker [67], and it was further developed by Draine and coworkers [50, 68, 69]. In chapter 2, we have extended CDM for second harmonic generation from small particles [116]. The uncoupled dipole model is numerically less expensive as compared to the coupled dipole model. In this chapter, we discuss the conditions under which CDM results are more accurate as compared to results from UDM. We have also extended the coupled dipole model to THG and CARS.

3.1 Theory

The theory of macroscopic and microscopic polarization has been briefly discussed in chapter 1. The coupled dipole theory for second harmonic scattering has been discussed in chapter 2 but the equations have been reproduced here for the sake of clarity. If $\mathbf{E}_{inc,i}$ is the incident field of angular frequency ω at the i^{th} dipole and $\mathbf{P}^{(1)}_i$ induced linear dipole, then these quantities are related by equation (3.1):

$$\mathbf{P}_i^{(1)} = \boldsymbol{\alpha}_{\omega,i}\left(\mathbf{E}_{inc,i} - \sum_{j\neq i}^{N}\mathbf{A}_{ij}^{(1)}\mathbf{P}_j^{(1)}\right) \tag{3.1}$$

$$\left.\begin{aligned}
&\mathbf{A}_{ij}^{(1)}\mathbf{P}_j^{(1)} = \frac{\exp(ikr_{ij})}{r_{ij}^{3}}\Big[k^2\mathbf{r}_{ij}\times(\mathbf{r}_{ij}\times\mathbf{P}_j^{(1)}) + \\
&\quad \frac{(1-ikr_{ij})}{r_{ij}^{2}}\left\{r_{ij}^{2}\mathbf{P}_j^{(1)} - 3\mathbf{r}_{ij}\left(\mathbf{r}_{ij}.\mathbf{P}_j^{(1)}\right)\right\}\Big],\ \text{for } j \neq i; \\
&\mathbf{A}_{ij}^{(1)} = \boldsymbol{\alpha}_{\omega,i}^{\ \ -1},\ \text{for } j = i.
\end{aligned}\right\} \tag{3.2}$$

$$\sum_{j=1}^{N}\mathbf{A}_{ij}^{(1)}\mathbf{P}_j^{(1)} = \mathbf{E}_{inc,i} \tag{3.3}$$

The interaction between the dipoles is defined by a Green's function (Eqn. 3.2) where k (= c/ω) is the wavenumber, $\boldsymbol{\alpha}_i$ is the linear polarizability of the i^{th} dipole and $\mathbf{r}_{ij}$ is the displacement vector between dipoles i and j. Equation (1) can be reduced to a simplified form as equation (3.3) and it can be solved using conjugate gradient method. The linear local field ($\mathbf{E}^{(1)}_{loc,i}$) from equation (3.4) can be used to calculate the local driving field for various nonlinear processes:

$$\begin{aligned}
\mathbf{E}_{loc,i}^{(1)} &= \boldsymbol{\alpha}_i^{-1}\mathbf{P}_i^{(1)} \\
&= \left(\mathbf{E}_{inc,i} - \sum_{j\neq i}^{N}\mathbf{A}_{ij}^{(1)}\mathbf{P}_j^{(1)}\right)
\end{aligned} \tag{3.4}$$

$$\mathbf{E}_{SHG,i}^{(2)} = \boldsymbol{\beta}_i\mathbf{E}_{loc,i}^{(1)}\mathbf{E}_{loc,i}^{(1)} \,/\, \boldsymbol{\alpha}_{2\omega,i} \tag{3.5}$$

$$\mathbf{E}_{THG,i}^{(3)} = \boldsymbol{\gamma}_i\mathbf{E}_{loc,i}^{(1)}\mathbf{E}_{loc,i}^{(1)}\mathbf{E}_{loc,i}^{(1)} \,/\, \boldsymbol{\alpha}_{3\omega,i} \tag{3.6}$$

$$\mathbf{E}_{CARS,i}^{(3)} = \boldsymbol{\gamma}_i\mathbf{E}_{loc\ pump,i}^{(1)}\mathbf{E}_{loc\ pump,i}^{(1)}\mathbf{E}_{loc\ Stokes,i}^{(1)} \,/\, \boldsymbol{\alpha}_{\omega_{CARS},i} \tag{3.7}$$

$$\sum_{j=1}^{N}\mathbf{A}_{ij}^{(n)}\mathbf{P}_{x,j}^{(n)} = \mathbf{E}_{x,i}^{(n)} \qquad \text{where } (n,x) = (2,\text{SHG}) \text{ or } (3,\text{THG}) \text{ or } (3,\text{CARS}) \tag{3.8}$$

$\boldsymbol{\beta}_i$ and γ_i are the first and second hyperpolarizabilities respectively of the *i*th dipole. Equations (3.5) and (3.6) were used to calculate SHG and THG driving fields. In the case of CARS two different excitation fields, pump and Stokes, are involved. If $\mathbf{E}^{(1)}_{pump,i}$ and $\mathbf{E}^{(1)}_{Stokes,i}$ are the local pump field and local Stokes fields respectively, as calculated by equation (3.4) then the CARS driving field can be calculated by equation (3.7). The induced nonlinear dipoles can be calculated by using the driving fields (Eq.3.8). In the UDM, these nonlinear dipoles can be calculated directly from the incident field (Eqs. 3.9-11). However it must be noted that when looking at the *i*th dipole, no other dipole comes into picture.

$$\mathbf{P}^{(2)}_{SHG,i} = \boldsymbol{\beta}_i \mathbf{E}^{(1)}_{inc,i} \mathbf{E}^{(1)}_{inc,i} \tag{3.9}$$

$$\mathbf{P}^{(3)}_{THG,i} = \boldsymbol{\gamma}_i \mathbf{E}^{(1)}_{inc,i} \mathbf{E}^{(1)}_{inc,i} \mathbf{E}^{(1)}_{inc,i} \tag{3.10}$$

$$\mathbf{P}^{(3)}_{CARS,i} = \boldsymbol{\gamma}_i \mathbf{E}^{(1)}_{inc\ pump,i} \mathbf{E}^{(1)}_{inc\ pump,i} \mathbf{E}^{(1)}_{inc\ Stokes,i} \tag{3.11}$$

3.3 Results & Discussion

Refractive index of a material is a measure of interaction between the material and light. The higher the magnitude of refractive index, the stronger is the interaction of light with that material. UDM takes into account only a part of this interaction but CDM captures this interaction adequately. Therefore it was hypothesized that with increase in refractive index of a material, the results predicted by UDM and CDM should differ. To test the hypothesis, second harmonic generation from hypothetical myosin fiber bundles was analyzed. Yew and Sheppard [114] had analyzed second harmonic polarization induced due to cross polarization terms in a thin layer of myosin fiber bundles when it is excited by a focused beam of light. When linearly polarized light, say *x*-polarized, is focused through a high numerical aperture (NA) lens, the polarization of light at the focus is not entirely along the *x*-axis but there are significant *y* and *z* polarized components as well. Richards and Wolf [117] calculated the vectorial distribution of light in the focal region of a lens in non-paraxial systems. The distribution of light in the focal region can be described by equations (3.12) and (3.13):

$$\left.\begin{aligned} E_x(\rho,z,\phi) &= -i\left(I_0 + I_2\cos 2\phi\right), \\ E_y(\rho,z,\phi) &= -iI_2\sin 2\phi, \\ E_z(\rho,z,\phi) &= -2I_1\cos\phi. \end{aligned}\right\} \tag{3.12}$$

$$\left.\begin{aligned} I_o(\rho,z,\phi) &= \int_o^{\sin^{-1}NA} \cos^{1/2}\theta\sin\theta(1+\cos\theta)J_0(k\rho\sin\theta)\exp(ikz\cos\theta)d\theta, \\ I_1(\rho,z,\phi) &= \int_o^{\sin^{-1}NA} \cos^{1/2}\theta\sin^2\theta J_1(k\rho\sin\theta)\exp(ikz\cos\theta)d\theta, \\ I_2(\rho,z,\phi) &= \int_o^{\sin^{-1}NA} \cos^{1/2}\theta\sin\theta(1-\cos\theta)J_2(k\rho\sin\theta)\exp(ikz\cos\theta)d\theta. \end{aligned}\right\} \tag{3.13}$$

Here (ρ,z,ϕ) are cylindrical coordinates of a point in the focal region of the lens. Figure 3.1(b) shows the polarization distribution of 800 nm wavelength light in the focal plane of a lens with numerical aperture of 0.87 (= sin 60°). When a thin layer of myosin fiber bundles oriented along the *x*-axis is illuminated by the focal field described above, the induced second harmonic polarization is mainly due to the *z*-polarized excitation rather than the *x*-polarized excitation [114]. This can be explained by the second order susceptibility, $\chi^{(2)}$ of myosin fiber bundles [118]:

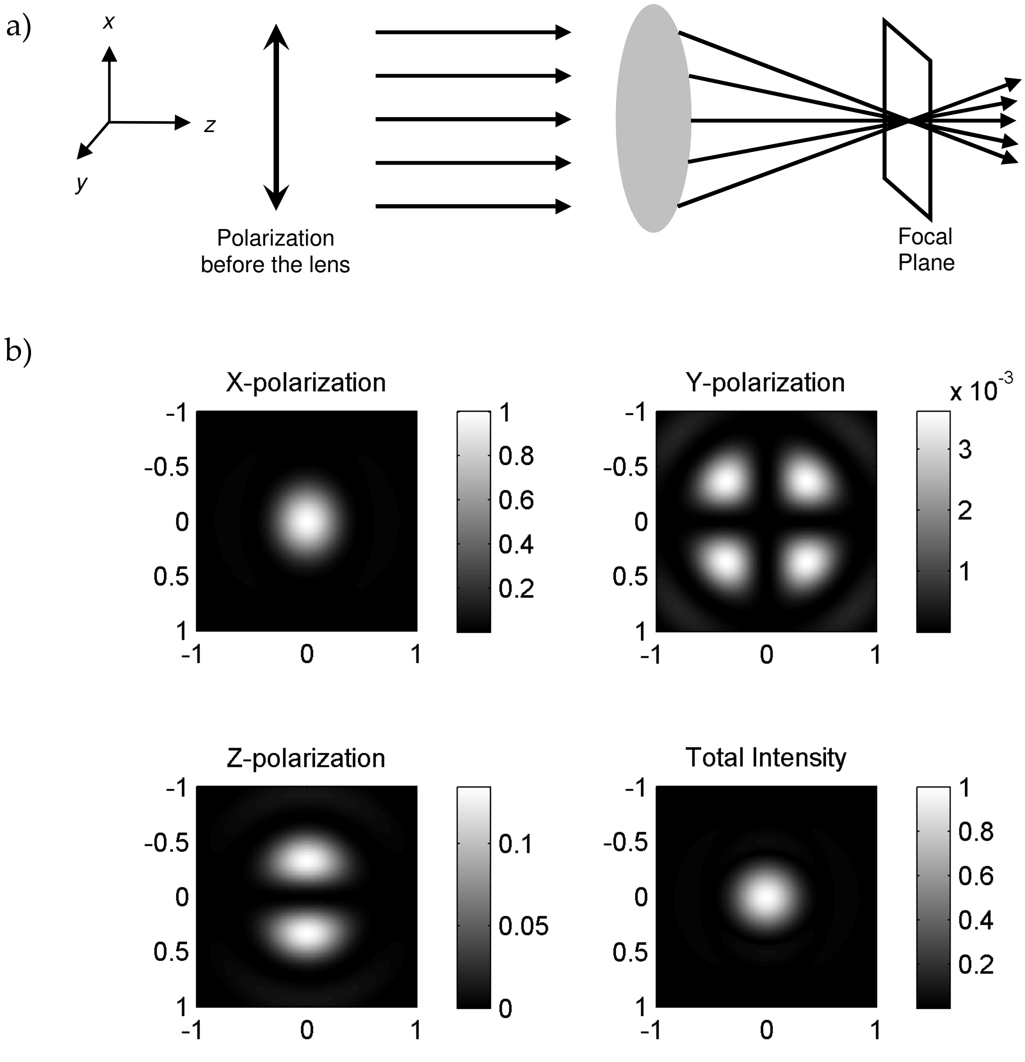

Figure 3.1. a) A schematic of x-polarized light being focused by a lens and b) distribution of polarization in the focal plane. The unit of the axes is μm.

$$\mathbf{P}_{SHG} = \boldsymbol{\chi}^{(2)}\mathbf{EE}$$

$$= \begin{bmatrix} 0.09 & 1 & 1 & 0 & 0 & 0 \\ 0 & 0 & 0 & 1.15 & 0 & 0 \\ 0 & 0 & 0 & 0 & 0 & 1.15 \end{bmatrix} \begin{bmatrix} E_xE_x \\ E_yE_y \\ E_zE_z \\ E_xE_y \\ E_yE_z \\ E_zE_x \end{bmatrix}. \quad (3.14)$$

The induced polarization in the myosin fiber bundle layer can be calculated by either UDM or CDM. Results from both these models were compared (Fig. 3.2). In both the dipole models, the size of a dipole was set at 20 nm. The collagen sheet was assumed to be surrounded by water. Figure 3.2(b) shows the distribution of the induced second order polarization as calculated by UDM. For CDM, refractive index of collagen needs to be included in the model. Depending on the hydration of collagen type I, its refractive index can vary from 1.36 to 1.42 [119]. Here we assumed that the refractive index of myosin fiber bundles lies within a similar range of values. In the CDM results presented here, refractive index values were set at 1.42 (Fig. 3.2(c)) and 1.6 (Fig. 3.2(d)), a hypothetical value to highlight the difference in results. The main difference in figures 3.2(b), (c) and (d) can be noticed in the *x*-component ($P^{(2)}_x$) of the induced second order polarization. With the increase in refractive index, the central lobe becomes stronger and the side lobes become weaker. This is due to interaction of dipoles among themselves.

However this small change is refractive index of should not affect the farfield SHG scattering in a significant manner because of the strong axially induced dipole components ($P^{(2)}_z$). Scatterers with a refractive index of large magnitude are better samples to test the farfield scattering effects. Metal nanoparticles are known to have high magnitudes of refractive index. As discussed in Chapter (2), the results of hyper Rayleigh scattering (HRS) experiments with silver nanoparticles can be predicted with CDM. To explain briefly, Russier-Antoinne *et al.* [93] measured *x*-polarized second harmonic scattering from a suspension of silver nanospheres as the input polarization was rotated through 360°. The average diameter of the silver nanospheres used was 40 nm, 60 nm and 80 nm. These experimental results were simulated using UDM. A comparison between CDM and UDM results shows that UDM fails to capture the effect of change in the size of silver nanospheres (Fig. 3.3). These results support our hypothesis that CDM performs better in terms of accuracy when refractive index of the scatterer is large in magnitude. On the other hand, for low refractive index materials, the difference in results is small and therefore from a computational point of view UDM is sufficient.

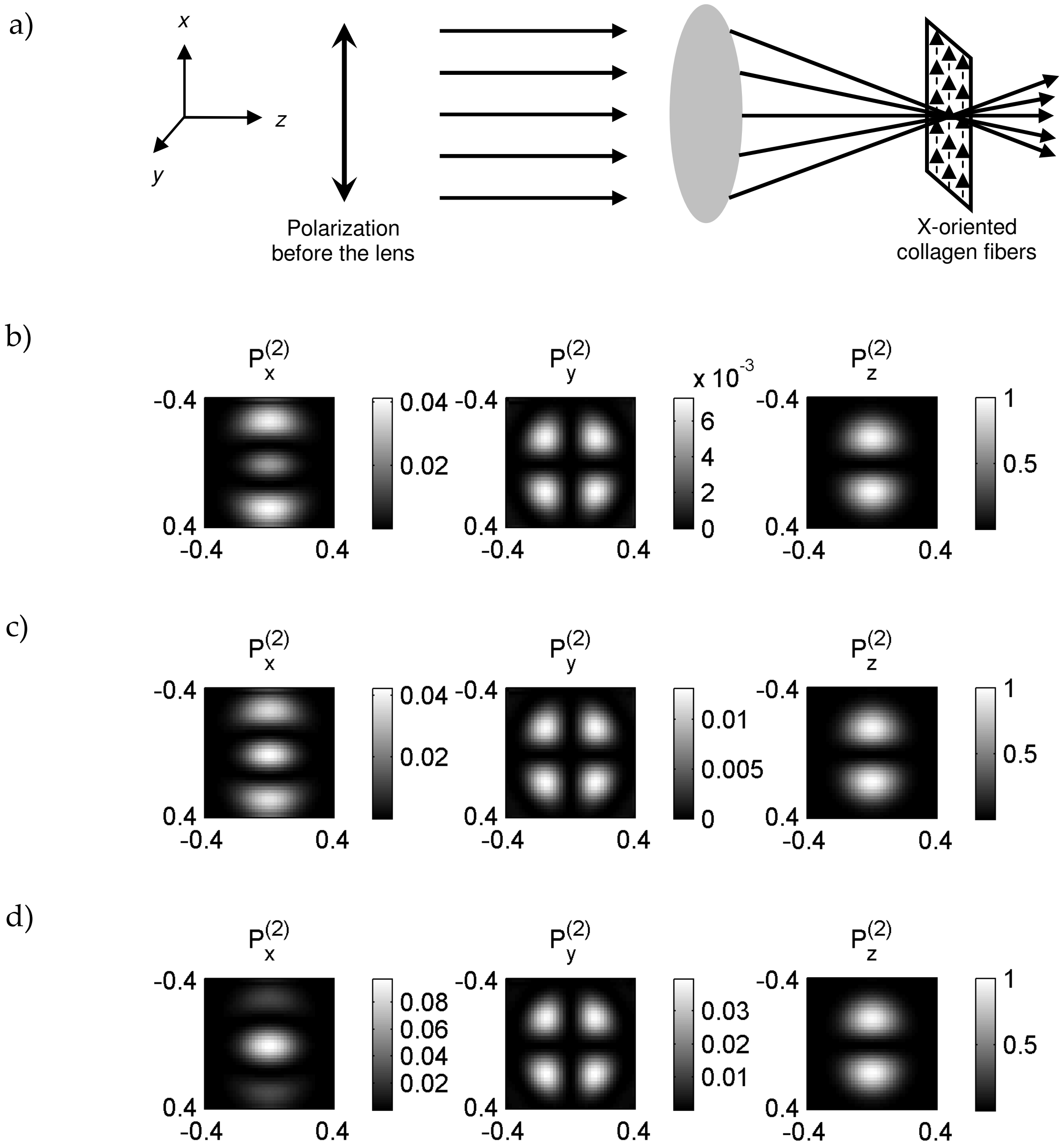

Figure 3.2. a) Schematic of x-polarized light being focused on a thin layer of collagen fibers oriented along x-axis. Distribution of second order polarizations induced in the collagen layer as calculated by UDM (b) and CDM for refractive index values of 1.42 (c) and 1.6 (d). The unit of axes is μm.

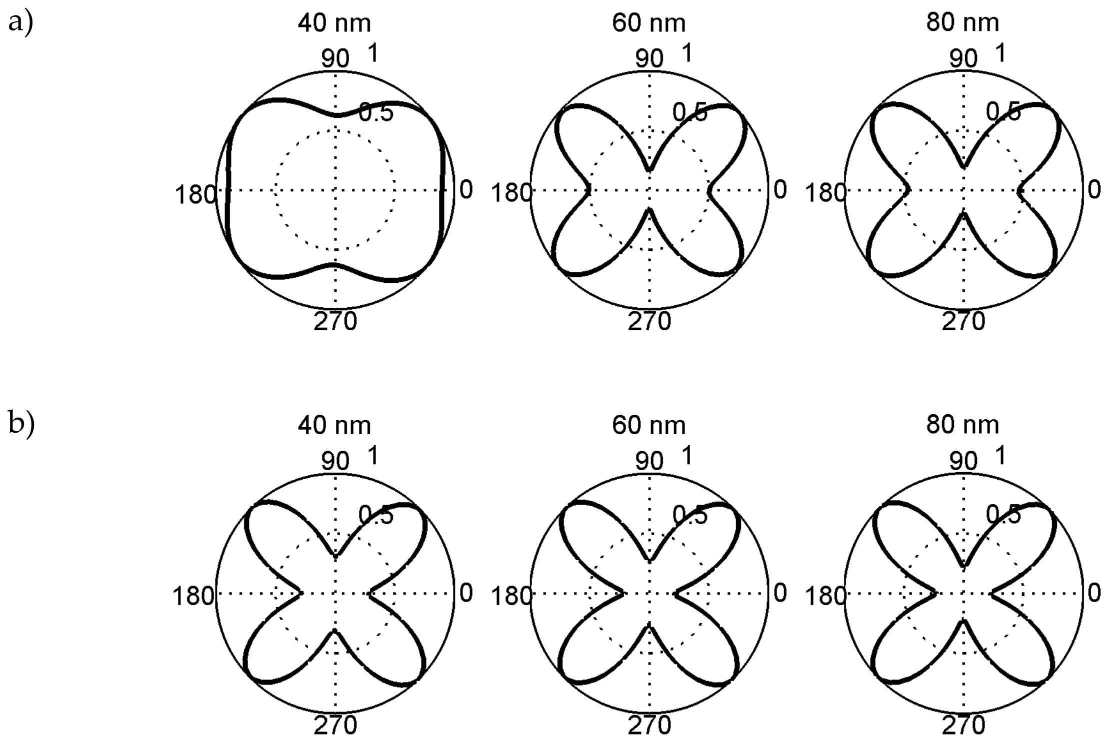

Figure 3.3. Polar plots of *x*-polarized second harmonic scattering from a suspension of silver nanospheres of sizes 40 nm, 60 nm and 80 nm as predicted by CDM (a) and UDM (b). The second harmonic scattering has been plotted against input polarization angle as measured with respect to the experimental *x*-axis.

Like UDM, CDM can be extended to other types of nonlinear scattering. Here we have demonstrated how CDM can be used to simulate two main types of third order scattering processes – THG (Eqs. 3.6 & 3.8) and CARS (Eqs. 3.7 & 3.8). Third harmonic scattering from polystyrene beads was taken as an example for this study. The refractive index of polystyrene was taken to be 1.59 [120]. The beads were assumed to be surrounded by water. Excitation wavelength was 1200 nm and the numerical aperture of the objective was set to 1. The third order polarizability (γ) of polystyrene was assumed to be the same as that of an isotropic material [121]:

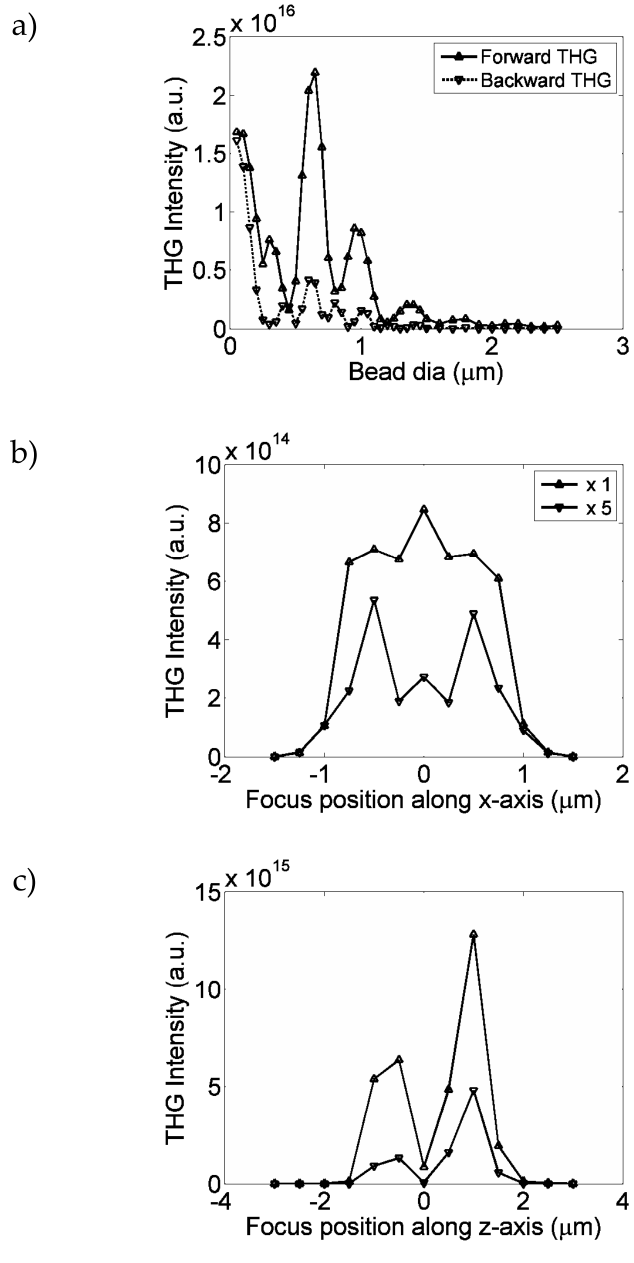

Figure 3.4. a) THG scattering from polystyrene beads of different sizes when excitation beam is focused at the center of the bead. THG scattering from a 2.5μm bead when focal spot is scanned axially (b), and transversely (c), across the center of the bead.

$\gamma_{xxyy} = \gamma_{yyxx} = \gamma_{yyzz} = \gamma_{zzyy} = \gamma_{zzxx} = \gamma_{xxzz}$,

$\gamma_{xyxy} = \gamma_{yxyx} = \gamma_{yzyz} = \gamma_{zyzy} = \gamma_{zxzx} = \gamma_{xzxz}$,

$\gamma_{xyyx} = \gamma_{yxxy} = \gamma_{yzzy} = \gamma_{zyyz} = \gamma_{zxxz} = \gamma_{xzzx}$ and

$\gamma_{xxyy} + \gamma_{xyxy} + \gamma_{xyyx} = \gamma_{xxxx} = \gamma_{yyyy} = \gamma_{zzzz}$.

Assuming that excitation and third harmonic frequencies are far from the resonance frequencies of polystyrene, from Kleinman's symmetry $\gamma_{xxyy}= \gamma_{xyxy}= \gamma_{xyyx}$. THG scattering in the farfield was calculated for both forward and backward directions. Effect of size of polystyrene beads (50 nm to 2500 nm) on the farfield THG when the laser beam is focused at the center of the bead was studied. An oscillatory behavior in the detected THG was observed with increase in the size of the bead. This can be understood from the fact that most of the THG comes from the surface dipoles of the bead because dipoles in the bulk mutually cancel each other's scattering. Therefore with change in the size of the bead, the surface dipoles oscillate sometimes in phase and sometimes out of phase. Besides this, the near field effects enhance the local field at specific location along the bead-water interface [122]. There are two factors which determine the magnitude of THG – phase difference across the bead and strength of the surface fields. For the smallest bead size, the phase difference across the bead is low and surface fields are strong because the entire particle lies within the focus. Therefore strong THG is recorded. As the size increases, the phase difference across the bead increases and strength of surface fields decreases. Therefore with increase in size, the average THG signal decreases in magnitude but it still has an oscillatory behavior because the phase difference oscillates (Fig. 3.4(a)). The backward THG is strong for small particles because of the small number of dipoles. With increase in the size of the beads and hence the number of dipoles, THG becomes predominantly a forward scattering process. The axial scan (Fig. 3.4(b)) and the transverse scan along x-axis (Fig. 3.4(c)) of the focal spot across a 2.5 μm polystyrene bead shows that the scattering is not symmetrical across the two interfaces of the particle as predicted by UDM [89]. Our results are supported by experimental results of THG from an axial scan of a polystyrene bead reported in the literature [123].

The simulations for THG were repeated for CARS from polystyrene beads. The size of beads was varied from 200 nm to 2000 nm. The pump wavelength (λ_p), the Stokes wavelength (λ_s) and the CARS wavelength (λ_c) are 750 nm, 852 nm and 670 nm respectively. This corresponds to a Raman shift of 1600 cm^{-1} in polystyrene beads [122]. The beads were assumed to be surrounded by water. The γ of polystyrene should have resonant and a non-resonant component whereas the γ of water should have only the non-resonant component. The non-resonant component of γ is taken to be of the same form as that in THG calculations. The γ of water, which contributes to background here, is assumed to be 60% in magnitude of the non-resonant γ of polystyrene. For the resonant γ, the ratios of non-zero elements are γ_{xyyx} / γ_{xxxx}

= 3/4, $\gamma_{xxyy} / \gamma_{xxxx}$ = 1/8 and $\gamma_{xyxy} / \gamma_{xxxx}$ = 1/8. Further, resonant γ was taken to be 2.5 times the magnitude of non-resonant γ.

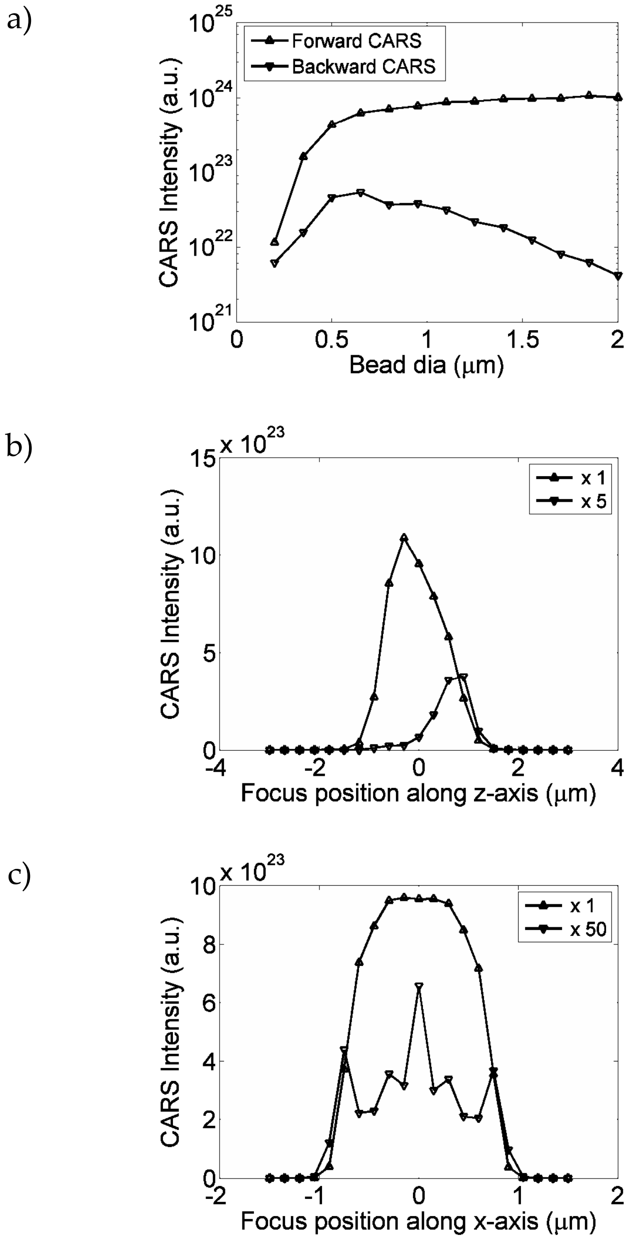

Figure 3.5. a) CARS scattering from polystyrene beads of different sizes when pump and Stokes beams are focused at the center of the bead. CARS scattering from a 1.5μm bead when focal spot is scanned axially (b) and transversely (c) across the center of the bead.

Being a third order scattering process, CARS is present in all materials. The effect of Gouy Phase shift at the focus is partially compensated by the interaction between the pump field and the conjugate Stokes field [124]. Therefore CARS is not restricted to interfaces and it increases with the increase in size of polystyrene beads increases and it saturates once the bead is big enough to cover the whole focal spot (Fig. 3.5(a)). Backward scattered CARS becomes weaker and forward scattered CARS becomes stronger with increase in size of the beads. The axial scan and the transverse scan along the x-axis of the focal spot across a 1.5 μm bead are shown is figures 3.5(b) and 3.5(c) respectively. The backward scattered CARS is much weaker than the forward scattered CARS because of the large size of the bead. The transverse scan shows that the locations of forward and backward CARS peaks do not overlap. These results match very well with experimental results reported earlier [125]. Backward CARS for the transverse scan shows multiple peaks. It has been reported earlier that backward CARS is due to refractive index mismatch between the scatterer and the surroundings [125]. Therefore we believe these peaks arise partly due to edge effects where there is refractive index mismatch.

3.4 Conclusion

A comparison between UDM and CDM shows that the latter gives better results when the refractive index of the scatter is large in magnitude. CDM is also able to predict the field enhancement at interfaces where there is a change of refractive index. The main difference between the two models is the interaction of different parts of the scatterer among themselves. This interaction becomes stronger with increase in the magnitude of refractive index. However, for scatterers with low magnitudes of refractive index, like biological specimen, the farfield scattering results as predicted by UDM and CDM would not differ significantly. Under such circumstances UDM is a better choice because of its lower computational cost as compared to CDM. In the experiments involving strong scatterers like metal nanoparticles or in experiments where surface effects are important, CDM is a better choice. We believe that CDM will be very useful in this era of nanophotonics where optical properties of small particles have assumed great importance.

Note: The contents of this chapter are based on the following paper:

N. K. Balla, Elijah Y. S. Yew, C. J. R. Sheppard and P. T. C. So, "Coupled and Uncoupled Dipole Models of Nonlinear Scattering," Opt. Express (In Press).

Chapter 4.

Bio-inspired nano contrast agents for second harmonic generation microscopy

4.1 Introduction

Gold nanoparticles have garnered much attention as contrast agents for various optical imaging modalities. Two main advantages of gold nanoparticles over conventional fluorophores are their low cytotoxicity [40] and resistance to photobleaching. Gold nanoparticles can be synthesized in a wide variety of shapes and sizes [36, 38, 126-128]. Since geometry is one of the main factors which dictates optical properties of these particle, optical properties of these particles are tunable [77, 129]. The simplest form of gold nanoparticle is a nanosphere. Gold nanospheres are strong scatterers of light and hence have been used as contrast agents for dark-field microscopy [130] and confocal reflectance microscopy [131, 132]. Gold nanoshells are superior to nanospheres in scattering light and their optical resonance can be tuned to the near infrared (NIR) wavelengths which are good for biological imaging. Therefore gold nanoshells have been used as contrast agents for *in vivo* imaging modalities like optical coherence tomography (OCT) [45]. Gold nanorods on the other hand have strong multiphoton luminescence properties [133]. These particles have been extensively used as contrast agents for multiphoton luminescence microscopy for cells and tissues [47, 64]. Gold nanoparticles are also known for their hyper-Rayleigh scattering (HRS) properties [134]. HRS is incoherent second harmonic generation (SHG) observed due to fluctuations in the orientation of scatterers in a colloidal suspension [135]. SHG is very sensitive to symmetry and under the dipolar approximation only non-centrosymmetric scatterers can give rise to SHG. In small gold nanospheres, the imperfect spherical shape of the particles gives rise to dipolar second harmonics scattering. With increase in the size of scatters, retardation effects become prominent and therefore multipolar second harmonic scattering is also observed [92]. The strength of second harmonic scattered light per atom of colloidal gold nanospheres is stronger than that of the best known molecular chromophores [136]. Such strong nonlinear scattering has been attributed to enhancement by plasmon resonance observed in gold nanoparticles. The most common morphologies of gold nanoparticles like rods, spheres and shells are centrosymmetric. In these nanoparticles, SHG arises from the surface where symmetry breaks down. It is possible to create *artificial molecules* [49, 137] out of nanoparticles with desired optical properties. A non-centrosymmetric gold nano-scatterer should give arise to strong SHG. Such nano-scatterer can be of two types – gold nanoparticles with non-centrosymmetric structure, or a non-centrosymmetric assembly of gold nanoparticles. SHG from chiral particles like planar G-shaped [138] and L-shaped [139] gold nanoparticles have been reported earlier. T-shaped gold nanodimers made up of gold nanorods [140] and multi-layered structure made up of gold nanospheres [141] have been reported to show enhanced second harmonic scattering. By carefully tuning the resonance of either chiral gold nanoparticles or chiral assemblies of gold nanoparticles to the excitation wavelength it is possible to create a strong second harmonic probe. It should be noted here that the gold nanoscattterer is being considered as a harmonophore. Some reports have used organic harmonophores in conjugation with metal nanostructures to benefit from the plasmonic enhancement of excitation field [142-144].

One promising approach to assemble nanoparticles into complex patterns is by using biological molecules as scaffolds [145, 146]. Assembly of gold nanoparticles into a double helix using peptide molecules as scaffold has been reported [147, 148]. Viral protein coats, also called capsids, can be used to assemble gold nanoparticles. Capsids are rigid as compared to protein or DNA molecules and they provide a number of specific sites where nanoparticles can be attached to achieve a pattern of interest. Tobacco mosaic virus (TMV) [149-151], cowpea mosaic virus (CPMV) [152] and M13 phage [153] are some of the viruses which have been used as scaffolds for metal nanoparticle assemblies. A. M. Belcher’s group has developed libraries of peptides [154] which can bind to inorganic nanoparticles, and these peptides were used to assemble nanoparticles into large assemblies [155, 156]. This strategy of using biological scaffolds has a number of advantages. The scaffolds can be altered to some extent by genetic engineering tools. These complex artificial molecules can be made in large scale with good structural consistency. The scaffolds are biodegradable. The small nanoparticles (~ 5 nm) used in such assemblies are suitable for renal clearance when administered into small animals. Surface modified viral scaffolds can be used as contrast agents for intravital imaging [157].

Assuming that such complex gold nanoparticle assemblies can be synthesized, we report a numerical study on second harmonic scattering from gold nanohelices with a TMV capsid like cylindrical core. The helix is one of the most common 3D chiral structures which we come across in nature. In nonlinear microscopy of tissues, fibrillar collagen is the main source of second harmonic generation. The unique triple helix structure of fibrillar collagen is responsible for its chiral and nonlinear optical properties [158]. Collagen fibrils are made up of peptide chains which are weak harmonophores. But, when these peptide chains bind together into a compact triple helix, they give rise to strong SHG due to coherent addition of second harmonic scattering by the individual peptides [159]. This effect can be mimicked in gold nanohelices to get enhanced SHG. Gold nanohelices can also be made by direct laser writing [160] but the method cannot be scaled up to synthesize large volumes of particles.

4.2 Theory

Analytical methods cannot be used to study light scattering from complex scatterers like a nanohelix. We therefore used the discrete dipole approximation method (DDA), also referred to as coupled dipole method (CDM). As discussed in chapters (2) and (3), CDM can accurately predict nonlinear scattering from metal nanoparticles. CDM had been used to study linear scattering form silver nanohelices [161]. Here however, in addition to the gold nanohelix, there is a hollow cylindrical core which supports the helix. The cylindrical core is assumed to be a TMV capsid whose optical properties are quite different from the optical properties of gold. Therefore two different kinds of materials are involved apart from the surrounding medium which is assumed to be water.

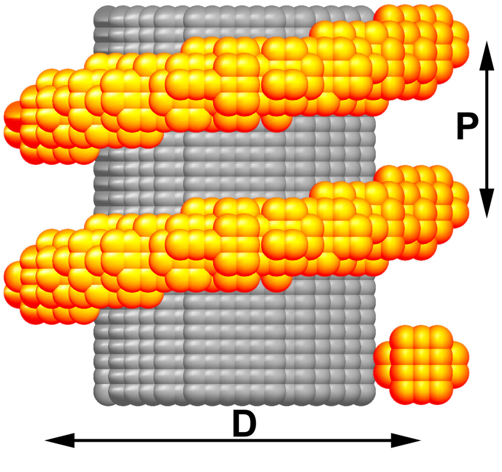

Figure 4.1. Cartoon of the helix (Yellow) over a cylindrical TMV capsid (Gray). The two main geometrical parameterss of the helix are pitch (P) and diameter (D).

The simulations presented here take into account the simultaneous interaction between all the dipoles involved. In other words, every gold dipole interacts with all the other gold and TMV dipoles, and vice versa. Similar multi-material simulation results have been presented earlier for HRS from beads coated with malachite green molecules (Chapter 2) and CARS from beads immersed in water (Chapter 3). However the mathematical manipulation involved in these simulations was not discussed in the earlier chapters so as to avoid deviation from the main focus of those chapters. The hypothetical scatterer proposed here includes a biological scaffold as its integral part and therefore we feel it is important to highlight this computational step. Linear interaction between all dipoles in a scatterer can be summarized in equation (1):

$$\sum_{j=1}^{N} \mathbf{A}_{ij}^{(1)} \mathbf{P}_{j}^{(1)} = \mathbf{E}_{inc,i} \cdot \tag{4.1}$$

In this equation, the term $A^{(1)}{}_{ij}\mathbf{P}_j$ calculates the electric field experienced by the i^{th} dipole due to the j^{th} dipole. Depending on whether the i^{th} dipole is a gold dipole or a TMV dipole, the term $A^{(1)}{}_{ij}$ would change. Therefore the interaction term $A^{(1)}{}_{ij}$ can be written as a sum of two different materials, the TMV core and the gold helix. Once the linear induced polarizations at all the dipoles were calculated, the extinction cross section of the scatterer at that wavelength was calculated to study the spectral response (Eq. 4.2):

$$C_{ext} = \frac{4\pi k}{|\mathbf{E}_{inc}|^2} \sum_{j=1}^{N} \mathrm{Im}(\mathbf{E}_{inc,j}^{(1)*} . \mathbf{P}_j^{(1)}) \quad . \tag{4.2}$$

The local linear electrical field at the dipoles can be calculated from equation (4.1). Since we are considering gold as the source of SHG, here the driving field for SHG was calculated only at the gold dipoles (Eq. 4.2). The elements of gold's first hyperpolarizability matrix ($\boldsymbol{\beta}$) are unknown. Therefore the effect of each of the 18 elements of the $\boldsymbol{\beta}$ was studied one by one by setting that element to 1 and setting all the other elements to 0. For example, in a Cartesian coordinate system, to study the effect of β_{xxx} , the form of the $\boldsymbol{\beta}$ matrix would be as shown in equation (4.3).

$$\mathbf{E}_{SHG,i}^{(2)} = \boldsymbol{\beta}_i \mathbf{E}_{loc,i}^{(1)} \mathbf{E}_{loc,i}^{(1)} / \boldsymbol{\alpha}_{2\omega,i} \quad \text{only for dipoles of gold nanohelix.} \tag{4.3}$$

$$\boldsymbol{\beta} = \begin{bmatrix} 1 & 0 & 0 & 0 & 0 & 0 \\ 0 & 0 & 0 & 0 & 0 & 0 \\ 0 & 0 & 0 & 0 & 0 & 0 \end{bmatrix} \tag{4.4}$$

CDM was used as a tool to calculate absorption spectra and second harmonic scattering properties of helices with different pitch lengths. The diameter of the cylindrical core scaffold was set at 18 nm which is typical diameter of a

TMV capsid. The refractive index of the core was assumed to be 1.57 [162]. Typical assemblies of gold nanoparticles use very small gold nanoparticles, less than 5 nm. Therefore the thickness of the gold helix was assumed to be 5 nm which made the total outer diameter of the entire structure 28 nm. Helices with 2 complete turns were used in the simulations, and only pitch length of the helices was varied. The different pitch lengths used in this study were 10, 15, 20, 25, 30, 35, 40 and 45 nm. The refractive index of the gold was calculated using data from Blanchard *et al.* [90] and it was corrected using the Claussius-Mossotti equation as described by Draine and Flatau [50]. The surrounding medium is assumed to be water, which is close to physiological conditions. In the simulations, the nanoparticles were excited by x-polarized laser light, which was focused by a lens of numerical aperture 0.87 (= sin 60^o). The incident field was calculated using vector theory of diffraction [117]. The relevant equations for focal field are presented in chapter (3). The excitation wavelength used for second harmonic scattering calculations was set at 800 nm. Most plasmonic nanoparticles are highly sensitive to polarization of light. Three different orientations (x, y and z) of the nanohelices were used in the simulations to account for their orientation with respect to polarization of the incident field. The SHG properties of gold nanohelices were compared with that of gold nanorods, which are one of the most common types of gold nanoparticles used as imaging probes. The size and aspect ratio of the gold nanorod was carefully chosen so that the volume and plasmon resonance wavelength of the nanorod and nanohelix are almost same. This allows for a fair comparison between SHG properties of the two nanoparticles. Second harmonic scattering from the nanoparticles was calculated by coherent summation of light scattered by all the constituent dipoles. For imaging probes, the direction of scattered light is an important factor. In bioimaging applications, back scattered light is considered important because it allows non-invasive imaging of optically thick samples. Forward and backward scattering was calculated by summation of second harmonic scattered light over a numerical aperture of 0.87. In order to visualize the scattering pattern from the nanoparticles, light scattered along *x*-*z* and *y*-*z* planes was calculated.

4.3 Results and discussion

For calculating SHG from a nanohelix, it is important to define the form of **β** matrix. A helix has a cylindrical structure and therefore **β** matrix was defined in a cylindrical coordinate system (Eq. 4.5):

$$\boldsymbol{\beta} = \begin{bmatrix} \beta_{\rho\rho\rho} & \beta_{\rho zz} & \beta_{\rho\phi\phi} & \beta_{\rho\rho z} & \beta_{\rho z\phi} & \beta_{\rho\phi\rho} \\ \beta_{z\rho\rho} & \beta_{zzz} & \beta_{z\phi\phi} & \beta_{z\rho z} & \beta_{zz\phi} & \beta_{z\phi\rho} \\ \beta_{\phi\rho\rho} & \beta_{\phi zz} & \beta_{\phi\phi\phi} & \beta_{\phi\rho z} & \beta_{\phi z\phi} & \beta_{\phi\phi\rho} \end{bmatrix}. \tag{4.5}$$

The choice of coordinate system also makes the interpretation of results easier. When calculating the driving field for SHG, the *z*-axis of the coordinate system was aligned parallel to the axis of the nanohelix by a rotation operation. The linear local electric field ($E^{(1)}_{loc,i}$) was recalculated in the cylindrical coordinates system before calculating the SHG driving field ($E^{(1)}_{SHG,i}$). For further calculations, the fields were converted into Cartesian coordinates and rotated back to the laboratory frame.

SHG from nanohelices of 8 different pitch lengths was studied. For each nanohelix, there are 18 elements of **β** matrix and for each element of **β** matrix, there are 3 different orientations of the nanohelix. Therefore altogether, there are 432 different simulations for SHG from nanohelices. It is not possible to analyze all these simulation results in detail at the same time. Therefore the initially the results were filtered out, based on maximum SHG detected in the farfield after summation over the 3 orientations and 18 elements of **β** matrix. The sum of second harmonic scattering intensity in the backward and forward direction, collected over a NA of 0.87 and 3 mm focal length, was considered as SHG detected in the farfield, unless otherwise mentioned.

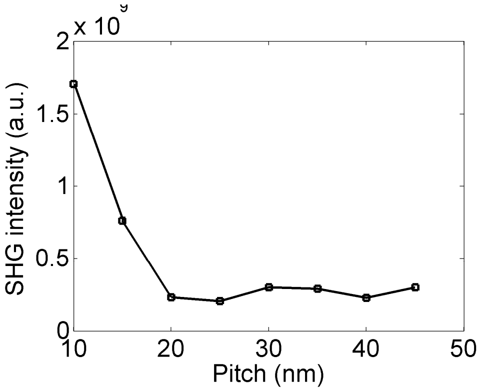

Figure 4.2. SHG detected in the farfield from nanohelices of different pitch lengths. The effects of orientation and elements of β matrix were averaged.

The intensity of SHG detected in the farfield decays rapidly with increase in pitch length from 10 nm to 20 nm and then with further increase in pitch length the intensity oscillates (Fig. 4.2). The high intensity of farfield second harmonic light scattered by small pitch nanohelices may be due to resonance with the excitation or second harmonic wavelengths. Next the effect of individual elements of β was analyzed. The normalized SHG detected in the farfield was plotted against pitch lengths and elements of β (Fig. 4.3). The normalization was achieved by dividing the SHG contribution of each element of β by the sum of contribution from all the elements. This normalization was done individually for each pitch length so that the difference in total SHG intensities does not interfere with the analysis. Here again the orientation effects were avoided by summation over all the 3 orientations.

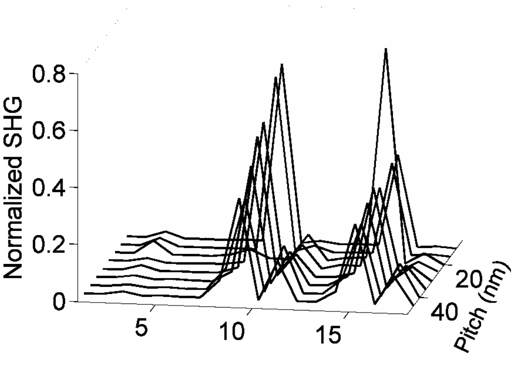

1	$\rho\rho\rho$	7	$z\rho\rho$	13	$\phi\rho\rho$
2	ρzz	8	zzz	14	ϕzz
3	$\rho\phi\phi$	9	$z\phi\phi$	15	$\phi\phi\phi$
4	$\rho\rho z$	10	$z\rho z$	16	$\phi\rho z$
5	$\rho z\phi$	11	$zz\phi$	17	$\phi z\phi$
6	$\rho\phi\rho$	12	$z\phi\rho$	18	$\phi\phi\rho$

Figure 4.3. Comparison of second harmonic scattered light due to different elements of $\boldsymbol{\beta}$. Listed aside are the numbers of different elements of $\boldsymbol{\beta}$ which are plotted along the horizontal axis in the 3-axis plot.

In figure (4.3), the $\boldsymbol{\beta}$ elements have been assigned numbers 1-18 for easier discussion. Elements 1-6 correspond to the cases where the second order polarization is driven along the radial direction of the helix. Similarly, elements 7-12 correspond to the axial direction, and elements 13-18 correspond to the azimuthal direction. Within each of these three categories, the SHG intensity is maximum for elements (3, 9 and 15) driven by azimuthal components ($E^{(1)}_{loc,\phi}$ $E^{(1)}_{loc,\phi}$) of local field, followed by elements (5, 11 and 17) driven by a combination of azimuthal and axial components ($E^{(1)}_{loc,z}$ $E^{(1)}_{loc,\phi}$) of the local field, and so on. This implies that the strength of induced linear local field follows the order $E^{(1)}_{loc,\phi} > E^{(1)}_{loc,z} > E^{(1)}_{loc,\rho}$. From antenna theory it is known that most of the electric field travels through the metallic structure. In this case, the majority of the electric field is channeled through the helix. A helical trajectory can be written as a sum of azimuthal and axial vectors but no radial vector is needed. This explains the difference in the strengths of different components of local field. In this study, only the pitch length of the helices was changed but the diameter of the helix was kept constant. Therefore the relative strength of axial vector which defines the helix should increase with pitch length and the strength of the corresponding azimuthal vector should decrease. This can be clearly seen in the relative strengths of SHG from the pairs of elements (3,5), (9,11) and (15,17) with increasing pitch length. There are other interfering factors like phase matching and resonance which make it difficult to come up with an exact mathematical relation between the components of the electric field. However these observations tell us that the simulations are working in the right manner.

From the above analysis it is evident that the helices with short pitch lengths are better for SHG. The linear spectral response of these helices with pitch lengths of 10 nm, 15 nm and 20 m was calculated for each orientation (*x*, *y* and *z*). The excitation light is almost purely *x*-polarized because at the center of the focal plane of an *x*-polarized beam the *z* and *y* polarized components are zero. *x*-oriented helices were found have a resonance peak around 510 nm (Fig. 4.4(a)), which is normally associated with gold nanospheres of sizes 20 nm and below. This resonance peak should be due to oscillation of plasmons across the thickness of the helices. Therefore the pitch length does not affect the position of the peak. The helices show strong resonance peaks in the infrared region when oriented along the *y*-axis (Fig. 4.4(b)). The estimated peak positions are 820 nm, 820 nm and 840 nm for helices with pitch lengths of 10 nm, 15 nm and 20 nm respectively. The infrared peak is strongest for the helix with 10 nm pitch. It should also be noted that the extinction cross-section of the helices in the blue region of the spectrum is large for the y-orientation. Lastly, when the helices are oriented along the z-axis the spectra again show infrared peaks around 880 nm (Fig. 4.4(c)). The estimated peak positions are 880 nm, 880 nm and 870 nm for pitch lengths of 10 nm, 15 nm and 20 nm respectively. The resonance is strongest in magnitude for 10 nm pitch. Even for z-orientation, the helices have a large extinction cross-section in the blue region of the spectrum. The extinction spectra of gold helices behave very similar to the extinction spectra of silver nanohelices reported earlier [161]. The infrared resonance peaks for y and z-orientations are due to oscillation of plasmons across the width of the helix. Another interesting observation which has not been reported earlier is the enhanced extinction cross-section in the blue region of the spectrum for y and z-orientations, which greatly help SHG in our case.

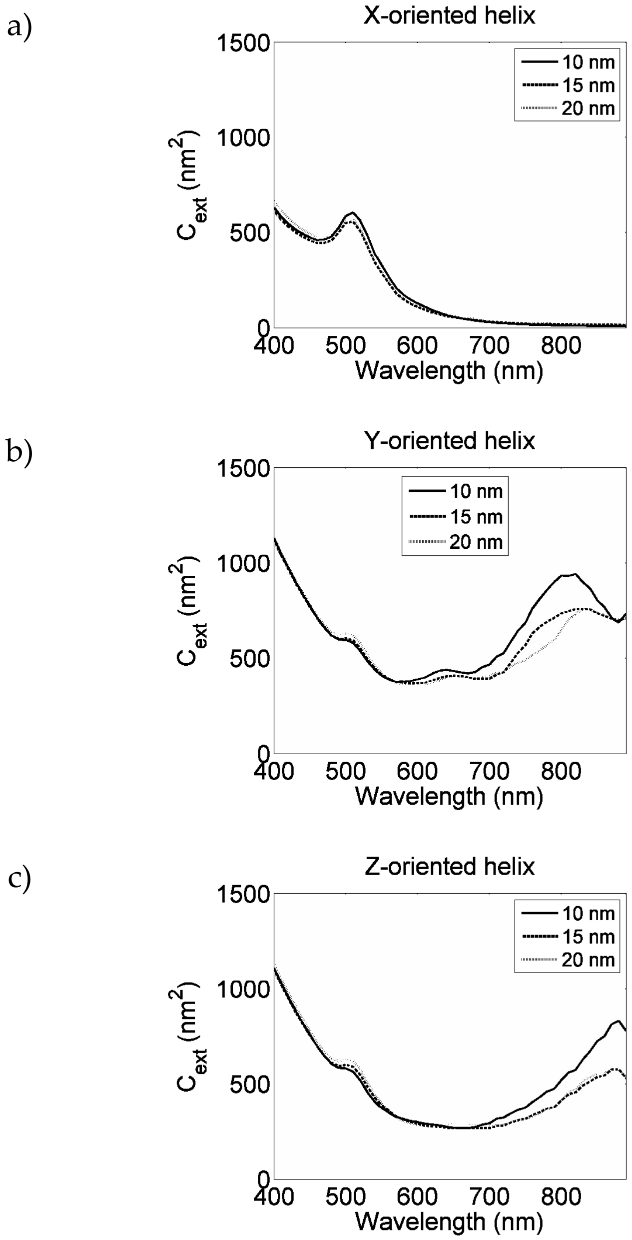

Figure 4.4. Linear spectral response of gold nanohelices with different pitch lengths for all three orientations along – a) x-axis, b) y-axis and c) z-axis.

The farfield SHG results and the linear spectra, both show that the helix with 10 nm pitch length is better for SHG as compared to the helices with other pitch lengths studied here. Since the pitch length has been finalized, it is interesting to compare the SHG properties of this helix with that of a gold nanoparticle commonly used as a contrast agent for nonlinear microscopy. A gold nanorod is centrosymmetric in its structure and therefore the comparison between a gold nanorod and nanohelix would highlight the effects of particle shape on SHG. A gold nanorod with a longitudinal plasmon resonance peak around 800 nm and with a volume similar to that of the helix would be ideal for comparison. The helix with 10 nm pitch has 2861 dipoles of size 1 nm and an approximate volume of 2865 nm^2. It is known that a gold nanorod with an aspect ratio of 4 has longitudinal plasmon resonance around 810 nm when placed in water [78]. Therefore it is easy to calculate the width of the desired rod. A nanorod with 10 nm diameter and 40 nm length has 2952 dipoles of 1 nm size and an approximate volume of 2880 nm^2. The linear extinction spectra of the gold nanorod were calculated for all three orientations (Fig. 4.5).

The gold nanorod closely resembles the helix with 10 nm pitch in volume and plasmon resonance wavelengths. Therefore the second harmonic scattering properties of the gold nanorod were compared with that of the helix. As mentioned earlier, a nanorod has a symmetric shape but its symmetry breaks at the surface. Therefore surface dipoles drive the second order polarization in a gold nanorod. The orientation of this driving force for second order polarization is normal to the surface [91]. A nanorod is made up of two hemispherical caps and a central cylindrical region which joins the two hemispheres. The hyperpolarizability (β) was defined in polar coordinates (Eq. 4.5) for the cylindrical region, and in spherical coordinates (Eq. 4.6) for the hemispherical caps:

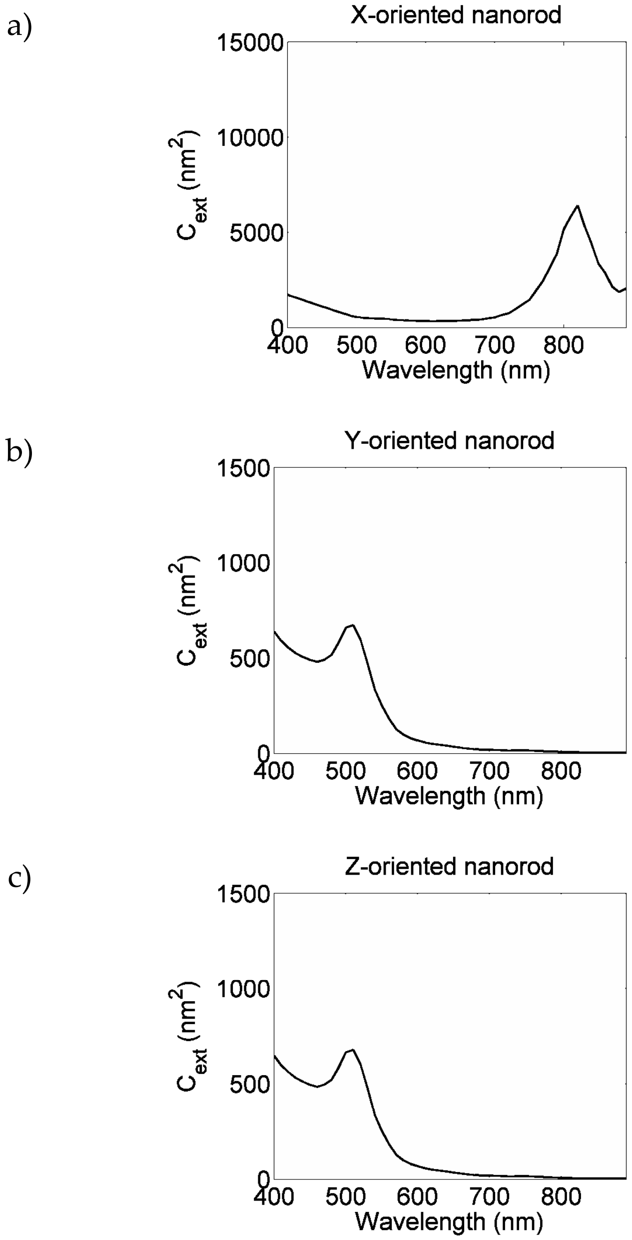

Figure 4.5. Extinction spectrum of 40 nm by 10 nm gold nanorod when oriented along (a) *x*-axis, (b) *y*-axis and (c) *z*-axis. It should be noted the scale along the *y*-axis in figure (a) is one order of magnitude larger than that in figures (b) and (c).

$$\boldsymbol{\beta} = \begin{bmatrix} \beta_{rrr} & \beta_{r\theta\theta} & \beta_{r\phi\phi} & \beta_{rr\theta} & \beta_{r\theta\phi} & \beta_{r\phi r} \\ \beta_{\theta rr} & \beta_{\theta\theta\theta} & \beta_{\theta\phi\phi} & \beta_{\theta r\theta} & \beta_{\theta\theta\phi} & \beta_{\theta\phi r} \\ \beta_{\phi rr} & \beta_{\phi\theta\theta} & \beta_{\phi\phi\phi} & \beta_{\phi r\theta} & \beta_{\phi\theta\phi} & \beta_{\phi\phi r} \end{bmatrix}. \tag{4.6}$$

Only the elements of the first row of **β** matrix were used, one at a time, in the case of SHG from gold nanorods, because these terms are responsible for driving the second order polarization normal to the surface of the rod. The excitation conditions and the farfield detection conditions were kept the same as in the case of the nanohelices. The scattering properties of the nanohelix and the nanorod were compared mainly on the basis of the magnitude of SHG detected in the farfield, and also on the extent of forward and backward scattering. The farfield SHG was calculated along *xz* and *yz* planes as the detector position was rotated through 180° about the origin where the scatterer was located. These calculations were done for each element of **β** matrix and for each orientation of the helix and the rod. It is not possible to present all the scattering plots here and therefore only one plot each, for the rod and helix have been presented here. In the case of the helix, element $\beta_{z\phi\phi}$ causes the strongest SHG when the helix is oriented along the *y*-axis (Fig.6a). Similarly in the case of a rod, element $\beta_{rrr/\rho\rho\rho}$ caused the strongest SHG when the rod is oriented along *x*-axis (Fig. 4.6(a)).

The second harmonic scattering strength of the nanohelix is double that of the nanorod (Fig. 4.6). But a more careful analysis should take into account the strength of drive fields as well. The extinction cross-sections of the nanohelix and the nanorod at 800 nm (excitation wavelength) give an estimate of the linear local field. The square of linear local field strength is proportional to the strength of the local field driving the second order polarization. The ratio of the linear local field strengths of the nanorod and nanohelix is 5.53, and therefore the ratio of driving field strengths is 30.6. Hence the net ratio of SHG from nanohelix and nanorod amounts to about 65. As expected the helical geometry is found to be highly efficient at SHG. The scattering is mostly in the backward direction which is advantageous for biological imaging. The relatively smaller extinction cross-section of the nanohelix has an advantage over the gold nanorod. Gold nanorods cause immense heating due their strong absorption cross-section which can alter the shape of the particles [133]. Such high local heat concentration can also damage the biological samples. A nanohelix would cause less heating due its lower absorption cross-section.

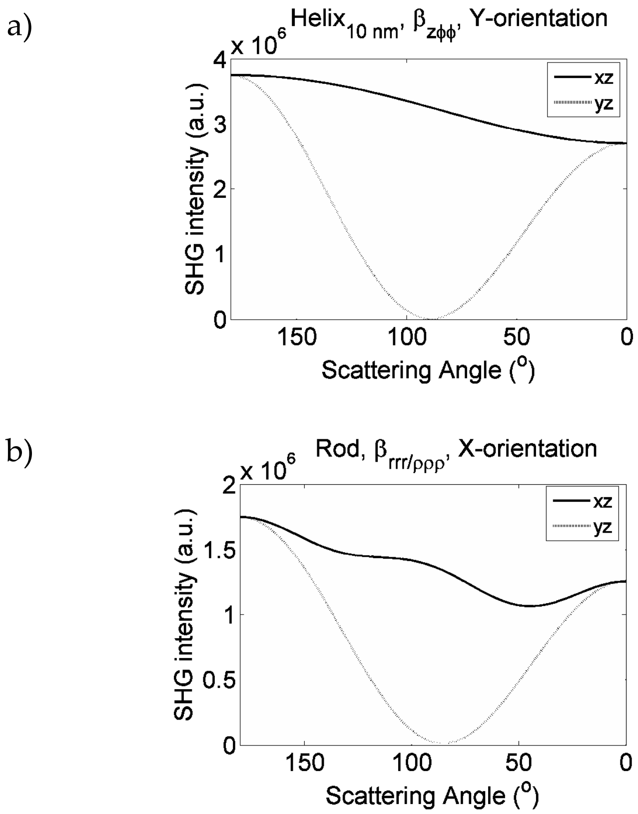

Figure 4.6. Scattering profile of SHG detected in the farfield along planes *xz* and *yz* as the detector was rotated about the origin. The abscissa is the angle made by the detector with the +ve *z*-axis. Therefore 180° represents the backward direction and 0° represents the forward direction.

4.4 Conclusion

With rapid advances in the synthesis techniques and molecular biology, it will be possible to create complex assemblies of nanoparticles on biological scaffolds. The helix, due to its non-centrosymmetric structure, is a good candidate for SHG. Therefore a helical geometry was proposed for an *artificial molecule* made of gold nanoparticles. Using DDA, the structural parameters of the gold nanohelix were optimized for a given excitation wavelength (800 nm in this case). More detailed plots of SHG in farfield and nearfield have been included in the appendix. The nanohelices considered in this study have only 2 complete turns. The efficiency of the nanohelices should improve rapidly with addition of more turns. More detailed studies are required to account for practical issues, like structural imperfections during synthesis of real nanohelices. Artificial molecules with other desired optical particles can be conceived of, and they can be studied using a numerical tool like DDA.

Chapter 5.

Surface Modification and Multiphoton Luminescence Microscopy of Gold Nanorods

5.1 Introduction

In the previous chapters, we have shown that second harmonic generation (SHG) from small particles can be calculated using a nonlinear extension of the discrete dipole approximation (DDA) method. Most of the common types of gold nanoparticles synthesized are symmetric in shape and hence not ideal for SHG. Therefore, we studied the specific case of SHG from a hypothetical gold nanohelix which can be formed using Tobacco Mosaic Virus (TMV) capsid as a scaffold. Due to the chiral structure of a helix, gold nanohelices can be efficient contrast agents for SHG microscopy. However, it is not trivial to make these complex gold nanohelices and optimizing the synthesis techniques for such complex nanoparticle assemblies will take some time. Once synthesized, gold nanohelices have to be modified so that they can be effectively used as contrast agents in biological specimen. These modifications consist of stabilizing gold nanoparticles in biological buffers and coating these nanoparticles with an optimal number of ligand molecules to target a specific type of cells. These surface modifications would be the same as required for any other kind of gold nanoparticles. Therefore the experimental studies on using gold nanorods as contrast agents were carried out by multiphoton luminescence (MPL) microscopy. Freshly synthesized gold nanorods are covered with Cetyl trimethylammonium bromide (CTAB), a surfactant which stabilizes the gold nanorods in water and prevents them from aggregation. CTAB, however, is cytotoxic and hence has to be replaced by a biocompatible molecule that keeps the gold nanorods stable in biological buffers and also facilitates specific targeting by conjugation with ligands. Polyethylene glycol (PEG) is polymer which has been used in the pharmaceutical industry to deliver active molecules into the human body [163]. It has been used to stabilize gold nanorods in various buffers [164] and to eliminate cytotoxicity due to CTAB. Thiol (-SH) and di-sulphide (-S-S-) groups have a strong affinity for gold surfaces [165]. Therefore the most common form of PEG used for conjugation to gold nanoparticles is X-PEG-SH, where X- is either an active group (–NH– or –COOH) to which a ligand can be conjugated or it is an inactive group. Conjugation of PEG to gold nanoparticle surface decreases their non-specific uptake by cells [166] which is very important to improve specificity of targeting. In *in vivo* experiments involving lab animals, pegylated gold nanoparticles have better circulation times and reduced nonspecific accumulation in internal organs [167, 168]. The length [169] and form [170] of the PEG chain also affects the circulation times of the nanoparticles. We used linear PEG molecules of different chain lengths to stabilize the gold nanorods. Specific targeting of cancerous cells was achieved by conjugating the pegylated gold nanorods to anti-epidermal growth factor receptor (anti-EGFR).

Besides developing a methodology to modify surface of gold nanoparticles, we have improved MPL microscopy of gold nanorods. MPL is the most popular form of nonlinear optical contrast from gold nanoparticles. It is an incoherent emission and therefore it is not directly dependent on the shape of the particles. The most important factors affecting MPL are the local plasmon resonance and local field enhancement. Photoluminescence in metals was reported for the first time by Mooradian in 1969 [171]. It was single photon luminescence and the origin is believed to be recombination of electrons from the conduction band with holes in d orbitals in a metal. MPL is caused by nonlinear excitation of the electron-hole pairs. MPL was reported experimentally for the first time as a background in SHG studies from rough metal surfaces [172]. In the first systematic study of the phenomenon [173], MPL was observed only from rough metal surfaces whereas single photon luminescence was observed from both smooth and rough metal surfaces. This led to the conclusion that local field enhancement is necessary for the nonlinear excitation of electron-hole pairs. These results were supported by another study where MPL from gold nanospheres was reported [174]. There are conflicting reports on whether the photon absorption preceding MPL is simultaneous [47, 175] or sequential [176]. The MPL spectrum is broad; starting from below 400 nm and extending beyond 700 nm. Gold nanospheres were used for the first time as contrast agents for MPL microscopy in 2003 [177]. Photoluminescence from gold nanorods is much stronger than that in gold nanospheres [46]. The intensity of photoluminescence increases quadratically with the aspect ratio of the nanorod, and this is popularly referred to as "lightning-effect" of gold nanorods [46]. The suppressed interband damping in gold nanorods as compared to nanospheres is partly responsible for enhanced local fields and photoluminescence in the nanorods [178]. The local field enhancement at the tips of a gold nanorod is responsible for most of the MPL [175, 179, 180]. Gold nanorods have a strong longitudinal plasmon resonance (LPR) in the near infrared region that overlaps with the excitation wavelengths of MPL microscopy. All these factors have made gold nanorods one of the best contrast agents for MPL microscopy. The first report of *in vitro* and *in vivo* MPL microscopy with gold nanorods [47] highlighted the potential of these novel contrast agents in bioimaging. The two photon cross-section of the gold nanorods used in this study was 2320 Göppert-Mayer (GM; 1 GM = 10^{-50}cm^{4}s/photon) at 830 nm. To compare, the two photon cross-section of a Rhodamine 6g molecule is 40 GM [181] at the same wavelength. As a result, gold nanorods can be excited at intensities as low as 35 μW for cellular imaging [64].

However, there are certain drawbacks of using gold nanorods as contrast agents for MPL microscopy. The excitation wavelength generally overlaps with the LPR of gold nanorods. Therefore gold nanorods absorb the excitation photons very efficiently. Only a small fraction of the absorbed photons lead to MPL but most of these photons' energy dissipates as heat within the nanorod, thereby causing local heating. The extent of local heating is sufficient to melt the particle [133, 182]. A suspension of gold nanorods when irradiated with a wavelength which overlaps with its LPR, can causes a sharp rise in temperature [183]. This local heating, when unintended, has adverse effect on biological samples. On the other hand the photothermal effect can be very useful to kill malignant cells by specifically targeting gold nanorods to these cells. Tumor cells can be specifically targeted and destroyed using the photothermal heating of gold nanorods [184]. Further it was observed that gold nanorods localized on the cell membrane are much more effective in cell damage by photothermal heating as compared to the gold nanorods internalized by the cells [185]. Gold nanorods bound to the cell membrane cause membrane blebbing upon being irradiated with wavelengths close to their LPR [186]. The photothermal heating with gold nanorods is also effective against tumor in laboratory animals. Irradiation of untargeted gold nanorods, which have accumulated in a tumor post injection, reduce the growth of the tumor [169]. Intravenous injection of gold nanorods targeted to tumor cells improves the photothermal therapy of the tumor [187]. Apart from photothermal destruction of cells, this effect can be used to selectively release different kinds of molecules like oligonucleotides [66] which were bound to the gold nanorods. So there are two different properties of gold nanorods, MPL and photothermal heating, which have been shown to have wide application in biology. Unfortunately imaging of gold nanorods by MPL microscopy is always accompanied by some local heating and unless excitation laser power is carefully monitored, the damage to biological samples can be significant. One way to solve this problem is to excite MPL in gold nanorods with a wavelength which does not overlap with the LPR of nanorods. This would require slightly more power than the conventional MPL microscopy but photothermal heating would reduce significantly. Composite nanoparticles made of silver and gold have been used in MPL microscopy with excitation wavelengths around 1200-1300 nm [188, 189]. These excitation wavelengths are far away from the plasmon resonances of the composite particles used. The photothermal effect was relative weak with the longer wavelengths. Another major advantage of these longer wavelengths is better tissue penetration [1, 190, 191]. We have demonstrated that femtosecond pulsed lasers operating around 1200 nm are good for MPL microscopy with gold nanorods as contrast agents, and damage due to photothermal heating with these wavelengths is considerably less than that observed with excitation wavelengths close to the LPR of the nanorods.

5.2 Materials and Methods

Synthesis of gold nanorods: Gold nanorods with different aspect ratios were synthesized using the seed-mediated synthesis method [192]. This synthesis method is adapted from a report by Sau and Murphy [193]. Minor changes were made to the protocol to scale up the synthesis volume. The gold seed solution was prepared by mixing 250 µl of 0.01 M gold salt ($HAuCl_4.3H_2O$, Sigma-Aldrich Inc.) in 9.75 ml of 0.1 M CTAB (Sigma-Aldrich Inc.) and reducing this mixture at room temperature by addition of 600 µl of freshly prepared ice-cold 0.01 M sodium borohydride ($NaBH_4$, Sigma-Aldrich Inc.) under continuous stirring. The resultant seed solution was stored at room temperature.

For gold nanorod synthesis, 500 µl of 0.01 M gold salt and 50 µl of 0.01 M of silver nitrate ($AgNO_3$, Sigma-Aldrich Inc.) were added to 9.5 ml 0.1 M of CTAB. This solution was partially reduced by addition of 60 µl of 0.1 M freshly prepared L-ascorbic (Sigma-Aldrich Inc.) acid under continuous stirring. On addition of ascorbic acid, the solution turns colorless. To this reaction mixture, 10 µl-100 µl of seed solution was added, depending on the required aspect ratio of the rods. The solution was gently mixed and left undisturbed at room temperature for 16 hours. A final colored solution of gold nanorods was obtained. These gold nanorods were washed a couple of times by centrifuging at 3500 g for 40 min and re-suspending the pellet in double distilled (DD) water. The particles were analyzed by UV-visible spectrometry (UV-2450, Shimadzu Corp.) and stored at 4°C. Apart from the synthesized gold nanorods, one batch of gold nanorods (Nanorodz # 30-10-

808) with an LPR of 812 nm was purchased from Nanopartz Inc, Salt Lake City, UT.

Pegylation of gold nanorods: The cytotoxic CTAB on the surface of gold nanorods was replaced with PEG. PEG is not known to be cytotoxic, and it also prevents gold nanoparticles from aggregating in biological buffers like phosphate buffer saline (PBS). Linear methoxy/amine PEG with thiol (MeO-PEG-SH) terminus was obtained from Celares GmbH. The size of PEG molecules used in the experiments reported here is 5 KDa. Pegylation was carried out by adding 500 ◎l solution of PEG in DD water to 1 ml gold nanorods suspension with a LPR of magnitude 1.0. PEG was added while sonicating the gold nanorods, and the mixture was left for overnight shaking [194]. Excess PEG and the displaced CTAB were removed by centrifugation at 2500 g for 30 min. The precipitate of pegylated nanorods was washed twice with DD water and suspended finally in 1X PBS.

Optimizing concentration of PEG: The supernatant from the first centrifugation of pegylated gold nanorods was used to estimate excess PEG by Ellman's reagent (5,59-dithiobis-(2-nitrobenzoic acid, Sigma-Aldrich Inc.) [194]. Ellman's reagent is used for quantification of thiol (-SH) groups in a sample. Ellman's reagent reacts with thiol groups to give 2-nitro-5-thiobenzoate which absorbs strongly at 412 nm. Gold nanorods with LPR at 618 nm were pegylated with 2 KDa MeO-PEG-SH of four different concentrations – 20 μM, 100 μM, 500 μM, and 2.5 mM. The supernatant after first centrifugation of gold nanorods was incubated with Ellman's reagent at room temperature for 30 min and the absorption of the reaction mixture was measured at 412 nm using Infinite-200 microplate reader (Tecan Trading AG).

Protein/antibody conjugation: PEG with an amine terminus (NH_2-PEG-SH) was used instead of MeO-PEG-SH to conjugate gold nanorods with a protein. Glutaraldehyde was used as cross-linker between the pegylated gold nanorods and the protein molecules [195, 196]. 1 ml of pegylated gold nanorods were centrifuged and resuspended in 1 ml of 0.5% (v/v) of glutaraldehyde. The suspension was left in a shaker for 3 hours at room temperature. Glutaraldehyde attaches to the primary amines of PEG molecules on gold nanorods. The excess glutaraldehyde was removed by washing the gold nanorods twice with 1X PBS. To 1 ml of the glutaraldehyde activated nanorods, 5 μg of chilled protein was added and the mixture was left in a chilled shaker for another 3 hours. The glutaraldehyde on the gold nanorods binds to the primary amine groups on the outer surface the protein. The gold nanorods were washed twice in 1X PBS and stored at 4^{o}C.

Cell Culture: Human epidermoid carcinoma cells (A431), human cervical cancer cells (HeLa) and rat skeletal myoblasts (SKMB) were used in this study. Cell culture medium consists of 10% fetal bovine serum (FBS) and 1% penicillin –streptomycin (pep-strep) mix in Dubelco's Modified Eagle's Medium (DMEM). Cells were grown in T75 and T25 tissue culture flasks at 37°C. Once confluent, cells were detached using either 0.25% (A431 cells) or 0.05% (HeLa and SKMB cells) Trypsin. The detached cells were washed in cell culture medium and cultured again with a dilution factor of 1/4. For imaging purposes, these cells were grown either over 13 mm circular coverslips placed in 12-well plates or in 8-well chambered coverglass (Lab Tek™, Thermo Fisher Scientific Inc.).

Multiphoton Luminescence Imaging: Custom-built multiphoton microscopes were used for imaging (Fig 5.1). Femtosecond laser operating at center wavelengths of 824 nm (Mira900, Coherent Inc) and 1200 nm (OPO, Coherent Inc) were used for excitation. Laser light was coupled to FV300 laser scan head (Olympus Corp). The scanned beam was directed into either 1X71 inverted microscope (Olympus Corp) or a custom built table-top microscope with a detector (PMT, R3896, Hamamatsu Photonics) for non-descanned detection.

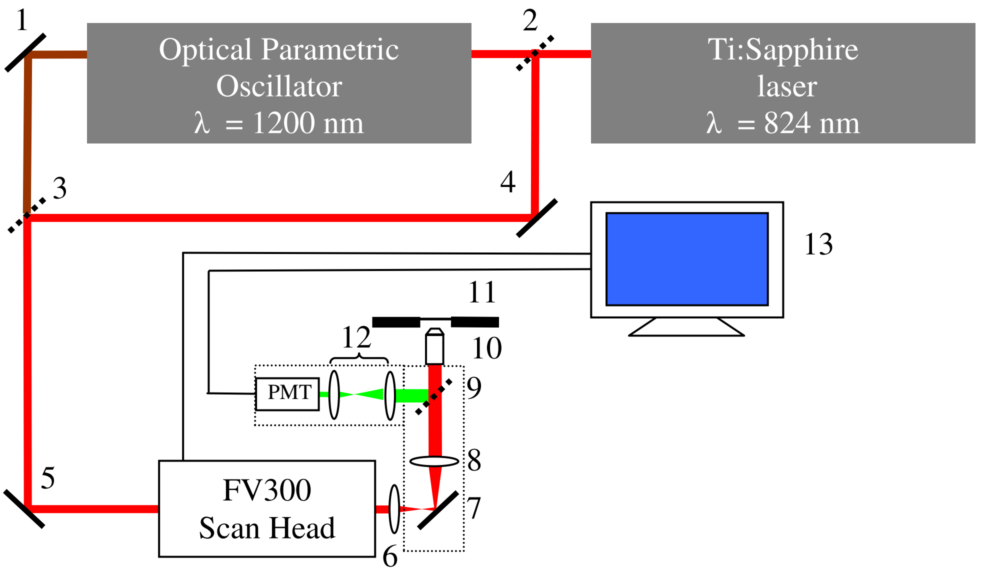

Figure 5. 1. Custom built MPL microscope used for imaging gold nanorods. The parts numbered in the schematic are - (1, 4, 5, 7) mirrors, (2) beamsplitter, (3) beam combiner, (6) scan lens, (8) tube lens, (9) dichroic mirror, (10) microscope objective, (11) microscope stage, (12) demagnifying lens combination, and (13) computer to control scanning and to acquire data.

The table top microscope was built with 2 inch optical elements which are large as compared to the optical elements found in most commercial microscopes. The large size optics improves the light throughput of the microscope.

5.3 Results and Discussion

Synthesis of gold seed yields a bright yellowish brown colored solution. The typical size of a gold seed is less than 4 nm [128]. By adding different volumes of this seed solution to the gold nanorod growth solution, gold nanorods different aspect ratios and hence LPR wavelengths were obtained.

The seed volumes of 10 μl, 20 μl, 60 μl, 80 μl and 100 μl yielded gold nanorods with LPR wavelengths of 605 nm, 618 nm, 650 nm, 677 nm and 709 nm respectively (Fig 5.2).

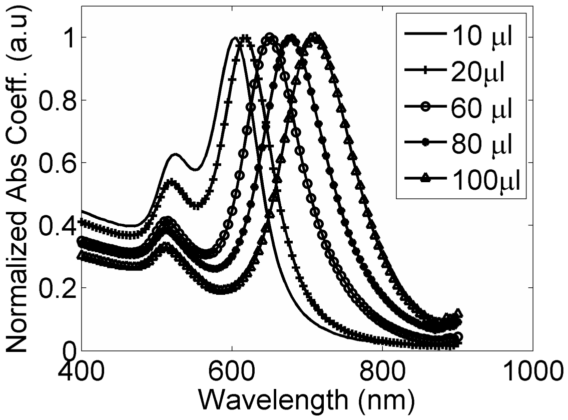

Figure 5.2. Absorption spectra of some of the synthesized gold nanorods. The LPR wavelength of the gold nanorods can be tuned by varying the amount of gold seed solution added to the synthesis mixture.

The CTAB on the surface of gold nanorods can be replaced with PEG molecules. However, the amount of PEG required for completely replacing the CTAB from a defined quantity of gold nanorods is not reported clearly in literature. One of the easiest measures of concentration of gold nanorods in a given suspension is the strength of LPR peak. It is also known that the strength of LPR of gold nanorods increases with aspect ratio. Therefore a suspension of gold nanorods with LPR wavelength at 650 nm and with peak strength 1.0 will contain more nanorods than a suspension of nanorods with LPR wavelength greater than 650 nm and peak strength 1.0. If the concentration of PEG required for gold nanorods with lower LPR wavelength is determined, this concentration will always be sufficient for gold nanorods with greater LPR wavelengths, provided the magnitude of LPR peak and thickness of the nanorods remains same. Gold nanorods with LPR wavelength at 618 nm were used to optimize the concentration of PEG required. For every 1ml suspension of gold nanorods with LPR peak strength 1.0, 500 μl of PEG solution was added. After pegylation, excess PEG in the supernatant was quantified using Ellman's reagent. The amount of PEG in the supernatant increased rapidly when PEG concentrations in excess of 500 μM were used (Fig. 5.3(a)). Therefore 500 μM PEG was used for all the pegylation experiments. After pegylation, the LPR peak of the nanorods shows a small red shift (Fig. 5.3(b)) and broadening.

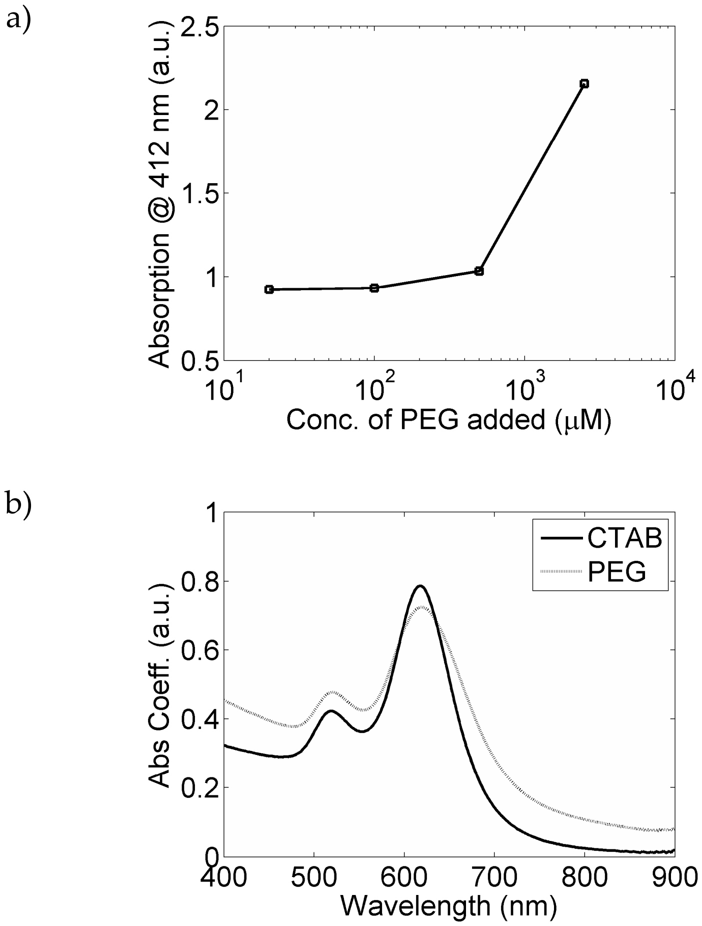

Figure 5.3. (a) Absorption of supernatants after reaction with Ellman's reagent as a function of initial PEG concentrations added to gold nanorod suspension. (b) Absorption spectra of gold nanorods after synthesis (CTAB coated) and after pegylation (PEG coated).

Pegylated gold nanorods are not cytotoxic and they are stable in 1X PBS. But these particles lack specificity for any cell type. In order to achieve specific targeting, gold nanorods have to be conjugated to some ligands. In this study, we used anti-EGFR (sc-120, Santa Cruz Biotechnology, Inc.) as a ligand for targeting cancer cells. For conjugation, NH_2-PEG-SH was used instead of MeO-PEG-SH. Anti-EGFR was conjugated to amine terminus (NH_2-) of PEG chain using glutaraldehyde molecule as a cross-linker. The gold nanorods can be coated with NH_2-PEG-SH or a mixture of NH_2-PEG-SH and MeO-PEG-SH. Only a few antibody molecules can be accommodated on gold nanorod due to steric hindrance. There should be enough NH_2-PEG-SH to saturate gold nanorods with antibody molecules. On the other hand, amine group (NH_2-), being positively charged, gets attracted to negatively charged cell surface causing non-specific binding. Therefore there should not be many free amine groups on the gold nanorods. To determine this critical ratio, we tried three different percentages of NH_2-PEG-SH – 10%, 50% and 100% in NH_2-PEG-SH and MeO-PEG-SH mixture. As a control for anti-EGFR, bovine serum albumin (BSA, sc-2323, Santa Cruz Biotechnology Inc.) was used. After conjugation, absorption spectra of all the six samples were recorded (Fig. 5.4). Gold nanorods coated with 10% NH_2-PEG-SH and conjugated to anti-EGFR had the lowest LPR peak strength of 0.75 among all the 6 samples. Before cell staining experiments, all the samples were diluted to have LPR peak strength of 0.75. This ensured that all the samples had roughly similar concentration of gold nanorods.

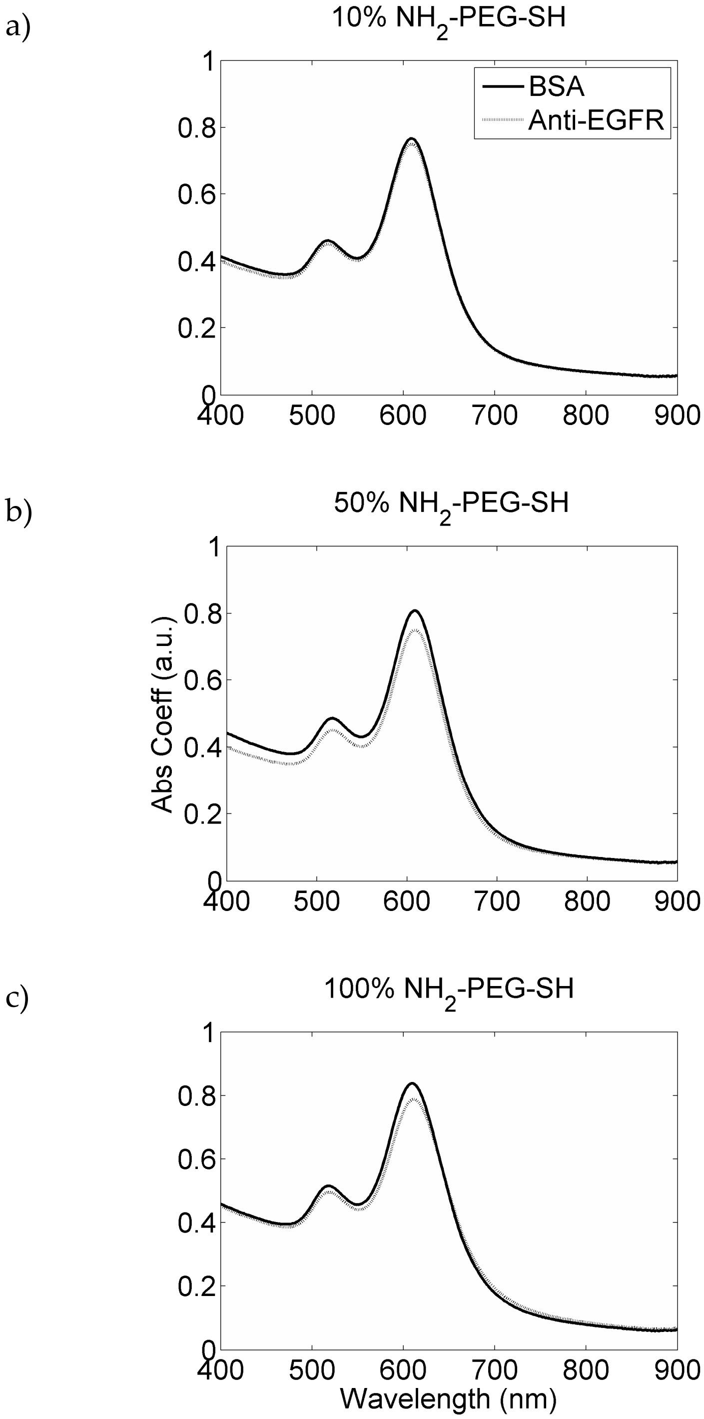

Figure 5.4. Absorption spectra of gold nanorods with (a) 10 %, (b) 50% and (c) 100% of NH_2-PEG-SH on their surface. These gold nanorods were conjugated to anti-EGFR (···) and BSA (–).

For evaluating the targeting efficiency of these gold nanorods, the nanorods were used to stain A431 cells which are known to express EGFRs in large numbers and SKMB cells which express only a few EGFRs. The cells of both types were cultured on 13 mm circular coverslips which were placed 12-well tissue culture plates. Once the cells reached 80 % confluence, they were washed and incubated with 200 μl of gold nanorods conjugated to either BSA or anti-EGFR and 300 μl of cell culture medium per well for 3 hrs. Then the cells were washed and fixed with 2% paraformaldehyde. The coverslips were mounted onto glass slides and sealed with nail enamel to prevent the drying up of the cells. For each cell type (A431 and SKMB) there were 3 different levels (10%, 50% and 100%) of amine grafting on the nanoparticle surface and for each level of amine grafting, there were 2 different proteins (BSA and anti-EGFR) conjugated. These 12 different cases were studied in this experiment. Gold nanorods attached to cell surface were imaged using a multiphoton microscope. The set up consists of modelocked femtosecond laser operating at wavelengths centered on 824 nm, FV300 scanhead and IX71 inverted microscope. The samples were imaged with a 40X/0.9 NA objective (Olympus Corp). Multiphoton luminescence from the gold nanorods was filtered with a shortpass filter (SP01-785RS-25, Semrock, Inc.) and detected using a PMT in the backward direction. Direct scattering from the cells in the forward direction was used to form an image of the cells. 3D imaging of the cells was carried out to map all the particles attached to cell-surface (Fig. 5.5).

a)

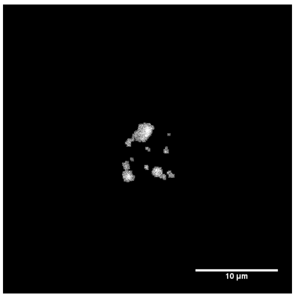

b)

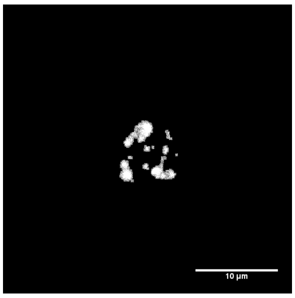

c)

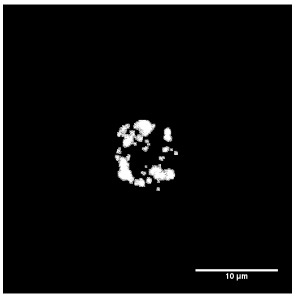

d)

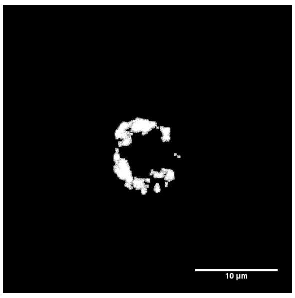

e)

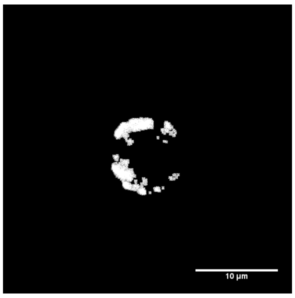

f)

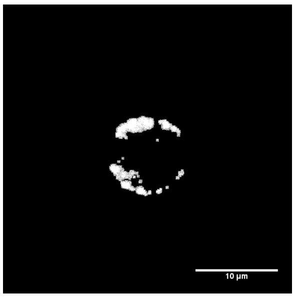

g)

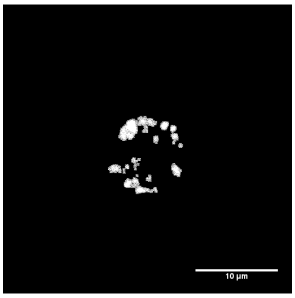

h)

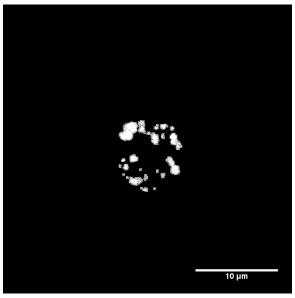

i)

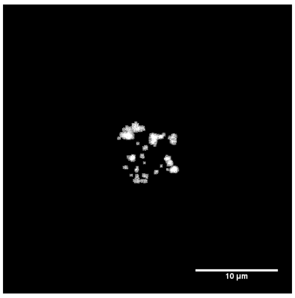

j)

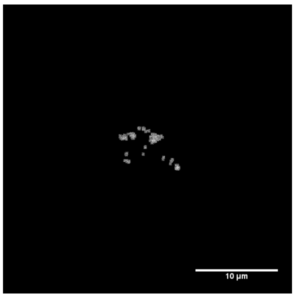

Figure 5.5. Z-stack multiphoton images (a-j) of an A431 cell stained with gold nanorods containing 10% NH_2-PEG-SH and conjugated to anti-EGFR. The images are 0.8 μm apart in depth and the scale bar is 10 μm.

To calculate the targeting efficiency of gold nanorods, all *z*-stack images were projected into a single plane and the area covered by gold nanorods was calculated in terms of number of pixels. The transmission images were used to calculate the area of the cells in a 2D plane. The percentage of cell surface covered by gold nanorods was used as a measure of the targeting efficiency. All the image processing was done using ImageJ software (MBF-ImageJ Bundle). The results (Fig. 5.6) show that 50% NH_2-PEG-SH coating on the surface of gold nanorods is ideal for achieving targeting efficiency against cancerous cells as well for reducing non-specific binding. Too low a percentage (10%) of NH_2-PEG-SH is not sufficient to conjugate protein molecules to nanoparticles. On the other hand, too high a percentage (100%) of NH_2-PEG-SH leaves many positively charged primary amine groups on the surface of gold nanorods. These amine groups stick to the negatively charged cell surface in a non-specific manner, which is undesirable. The process of conjugating gold nanorods to antibody is fairly general and it can be applied to any other type of gold nanoparticle.

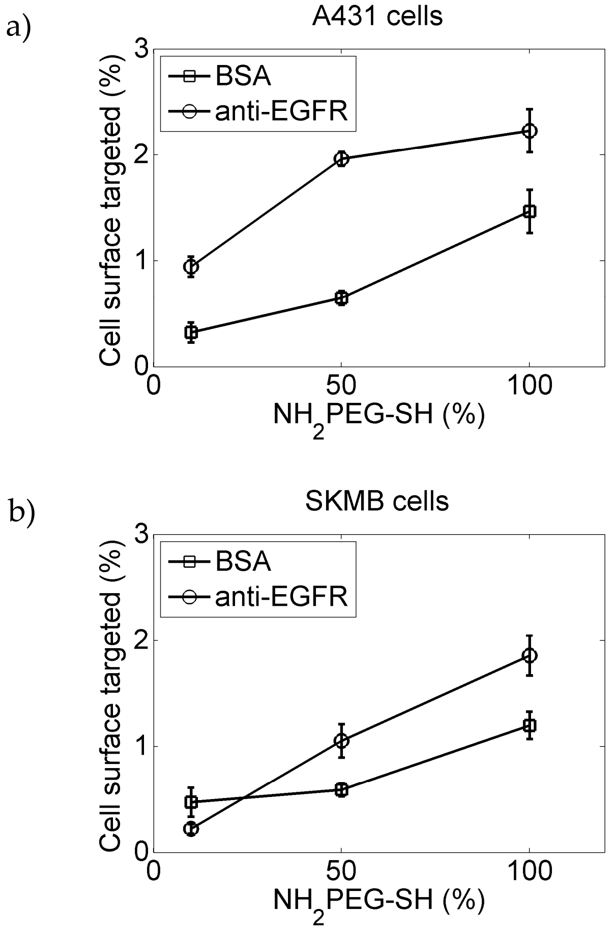

Figure 5.6. Percentage of cell surface covered with gold nanorods as a function of quantity of NH_2-PEG-SH on gold nanorods' surface. Gold nanorods have been conjugated to BSA (-□-) or anti-EGFR (-o-). A431 cells (a) express EGFRs in large numbers whereas SKMB cells (b) express only a few EGFRs.

In this process, we also demonstrated multiphoton microscopy of gold nanorods with LPR peak at 610 nm using excitation wavelength centered at 824 nm. This approach is different from most of the reports on multiphoton microscopy of gold nanorods [47, 64]. The more common approach is to use nanorods whose LPR peak overlaps with laser output. This enhances absorption and hence the subsequent photoluminescence by the nanorods.

Unfortunately only a small fraction of the absorbed photon energy leads to photoluminescence and the rest dissipates as heat. There is also no direct evidence to show that the mechanism of linear absorption is the same as the mechanism of multiphoton absorption. Our imaging results show that gold nanorods can be effectively used for multiphoton microscopy by exciting them away from their linear absorption maxima. To further support our observations, we compared thermal effects of gold nanorods on live cells when excited close to and far away from their absorption peak.

Gold nanorods with LPR peak at 812 nm (Nanopartz, Inc) were coated with 100% NH_2-PEG-SH to make them stick to cell surface. The LPR peak of these gold nanorods overlaps with Ti:Sapphire output which is center at 824 nm. Another laser output from the OPO which is centered at 1200 nm was used for exciting multiphoton luminescence in gold nanorods far away from the LPR peak. Wavelengths greater than 1000 nm have a very poor transmission in commercial microscopes. The OPO output is limited to a maximum of 110 mW, and therefore some modifications were required to minimize power losses in the microscope. All the mirrors used in the set-up were gold coated for efficient reflection of NIR wavelengths and all lenses in the laser path had anti-reflection coating for NIR wavelengths. The two main components a commercial laser scanning microscope are the scanhead and the microscope body. The scanhead is essential for scanning the beam and therefore we could not find a substitute for the scan head. The microscope body on the other hand is a relatively simple design and we replaced it with a table top custom built table-top microscope. This customized microscope uses larger aperture (2 inch) lenses and a large aperture objective (40x/1.3 oil) for efficient collection of light. After these modifications, we were able to get up to 6 mW of 1200 nm laser light from the objective of the microscope, which was sufficient for imaging thin samples. A non-descanned detection path was designed by imaging the back aperture of the objective onto a PMT. The output of the PMT was amplified and fed back to the Olympus A/D card. This allowed us to use the Olympus Fluoview software for image acquisition.

This customized microscope was used to image live A431 cells which were cultured in 8-well chambered coverglass. Before imaging, these cells were incubated with the gold nanorods for 3 hours. This gives sufficient time for some of the gold nanorods to stick to the cell surface. Just before imaging cells in a well, ethidium bromide was added to the well. Ethidium bromide is a nuclear staining dye which cannot penetrate through intact cell membrane. If the cell membrane ruptures due to heating by gold nanorods attached to the cell surface, the dye enters the cell and stains the nucleus. Fluorescence from nucleus-bound ethidum bromide can be excited with our Ti:Sapphire output. Transmission images of the cell were recorded using the 824 nm beam from the Ti:Sapphire laser. These transmission images (Fig. 5.7a, 5.7c, 5.8a & 5.8c) show the morphology of the cells before and after continuous scanning. Stained live cells were continuously scanned with a pixel residence time of 6.3

μs using either 824 nm or 1200 nm. When only 1 mW of laser power was used for 824 nm excitation wavelength, the cells ruptured with visible blebbing (Fig. 5.7(c)) and nuclear staining (Fig. 5.7(d)) by ethidium bromide within 25 s. However when 3mW of 1200 nm excitation wavelength was used, even after 80 s of continuous scanning, no cell damage or nuclear staining was observed (Fig. 5.8). 1200 nm wavelength is not detected my transmission PMT in our microscope. Therefore the transmission image (Fig. 5.8a) of the cells before continuous scanning was acquired using a single scan by 824 nm laser from the Ti:Sapphire. At the end of the continuous scanning by the 1200 nm laser, another transmission image (Fig. 5.8c) was acquired using a single scan by 824 nm laser. The apparent defocus in figure 5.8(c) is due mismatch in focal planes for the two different wavelengths – 1200 nm and 824 nm. The multiphoton intensity of gold nanorods from both the excitation wavelengths is comparable. It should be noted that the bright spots due to gold nanorods appear blurred because the nanorods are not rigidly bound to the cell surface and some of the nanorods are freely moving around in the culture medium. These results demonstrate that multiphoton microscopy of gold nanorods can be carried out much more efficiently with minimal thermal damage to cells by appropriately choosing the excitation wavelengths. NIR wavelengths around 1200 nm have other advantages like minimal scattering by tissue and attenuated absorption water. These long wavelengths cause minimal autofluorescence from biological samples, which is good for high contrast imaging.

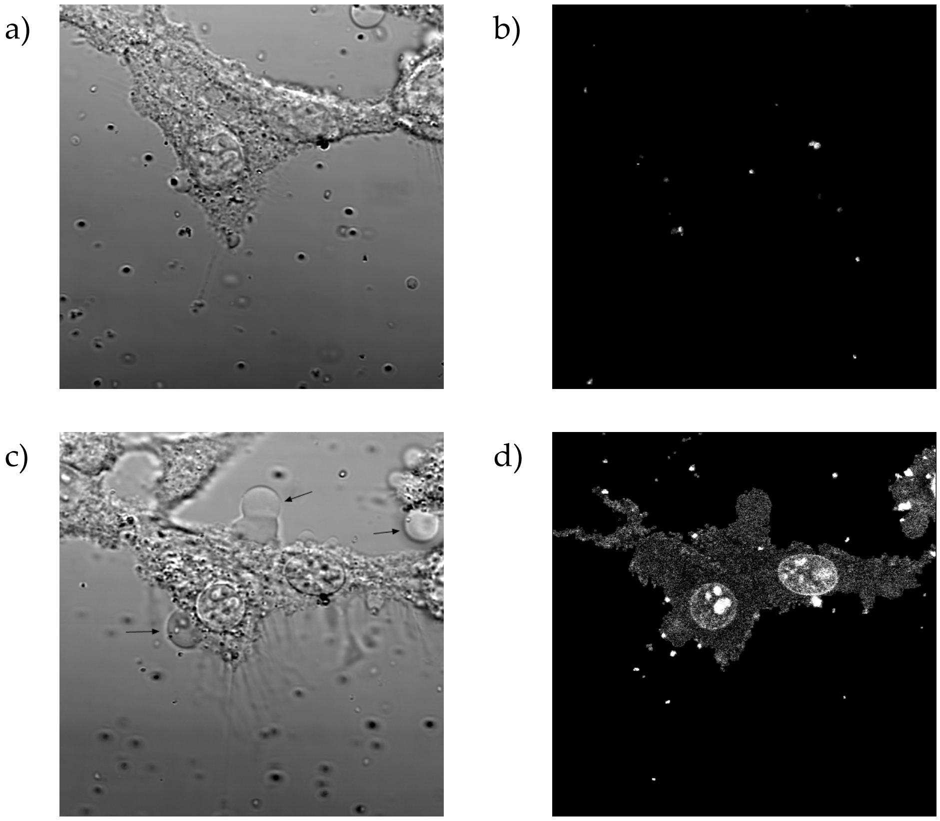

Figure 5.7. Images of A431 cells (a,b) before and (c,d) after 25s of continuous scanning with 1 mW focused femtosecond pulses centered at 824 nm. (a) and (c) are transmission images and (c) and (d) multiphoton luminescence images. Rupture of cell membrane can be inferred from the stained nuclei in image (d) and blebbing marked by arrows in image (c).

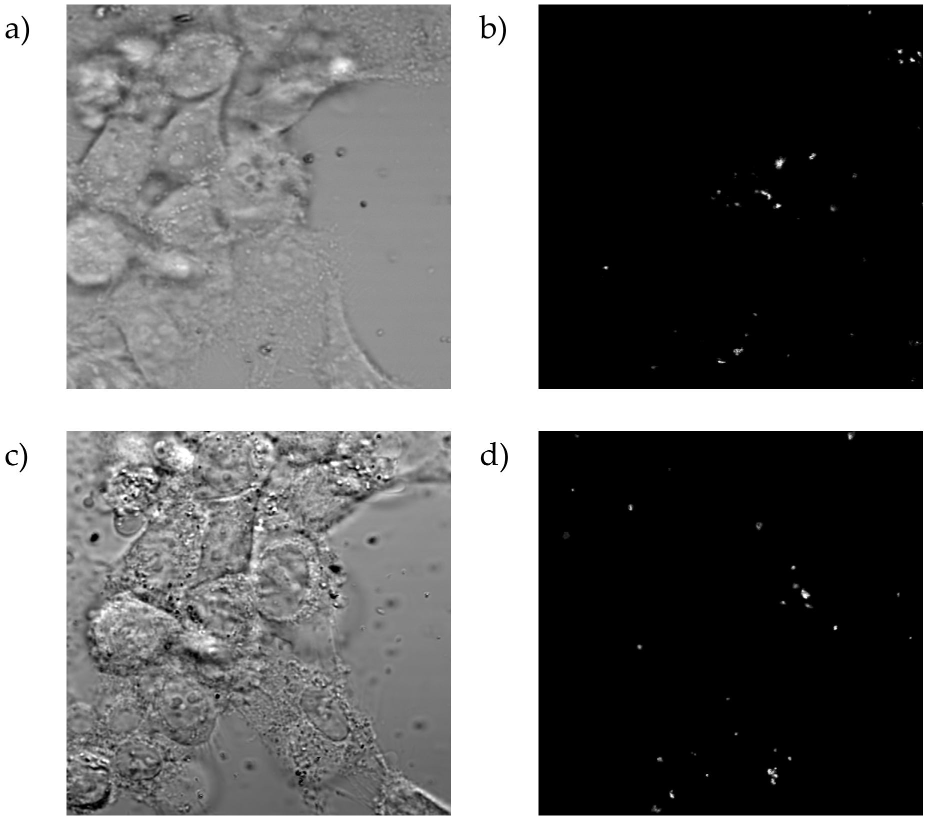

Figure 5.8. Images of A431 cells (a,b) before and after 80 s of continuous scanning with 3 mW focused femtosecond pulses centered at 1200 nm. (a,c) are transmission images whereas (b,d) are multiphoton luminescence images. Images (a,b) were acquired using 1200 nm excitation whereas images (c,d) were acquired using 824 nm. No nuclear staining is observed after prolonged scanning (d) but gold nanorods can be clearly visualized even with 1200 nm excitation (b).

5.4 Conclusions

We have developed a fairly general procedure to modify gold nanoparticles for imaging biological specimen. Gold nanorods were used as samples in this study because of the excellent optical properties like multiphoton luminescence. The gold nanorods of different aspect ratios were synthesized and coated with PEG molecules to make them biocompatible. PEG coated gold nanorods are good for *in vitro* as well as *in vivo* applications. Further, these gold nanorods were conjugated to an optimum quantity of anti-EGFR to target cancer cells. Multiphoton microscopy of gold nanorods with minimal thermal damage to cells was demonstrated by using femtosecond laser operating at 1200 nm.

Chapter 6

Conclusions

Optical properties of gold nanoparticles, their low cytotoxicity and simple surface chemistry make them promising contrast agents for current day optical microscopy. The gold nanoparticles which were initially synthesized were symmetric in shape, like spheres, shells and rods. The optical properties of these particles can be tuned over a wide range of the spectrum. But the symmetric geometry of these nanoparticles is not favorable for strong second harmonic generation (SHG). Non-centrosymmetric scatterers are known to be strong contrast agents for SHG. Gold nano-scatterers with non-centrosymmetric geometry can be synthesized either by lithographic techniques or by assembling very small gold nanoparticles (< 10 nm) into non-centrosymmetric assemblies. It is very useful to theoretically study the nonlinear optical properties of these nanoparticles. It helps us in understanding the interaction of light with small particles and it also helps us in designing nano-scatterers with specific optical activity. In other words, contrast agents for a specific kind of microscopy can be designed[49]. We developed a numerical method to simulate nonlinear interaction of light small particles of any shape. Our method assumes that a scatterer is made up of dipoles which interact with external radiation as well as among themselves.

This method is a combination of two models – the discrete dipole approximation (DDA)[50] for linear scattering, and the uncoupled dipole model for nonlinear scattering[113]. We introduced the concept of dipole coupling from DDA into the uncoupled dipole model for nonlinear scattering. Second harmonic scattering from small particles as predicted by the coupled dipole model agrees well with experimental results reported in the literature. Comparison between coupled and uncoupled dipole models shows that the coupled dipole model gives more accurate results when the magnitude of the refractive index of the scatterer is high, as well as when surface effects are involved. The coupled dipole model is computational expensive as compared to uncoupled dipole model and therefore for scatterers with low magnitudes of refractive index the uncoupled dipole model is better, as long as edge effects are ignored. The coupled dipole model is a conceptually simple model and it can be applied to scatterers of any shape and for any distribution of incident radiation. We used it as a tool to demonstrate how a contrast agent can be designed for second harmonic microscopy. Our design is a gold nanohelix, made up of gold nanoparticles arranged in a helical pattern on a tobacco mosaic virus. Using biological structures as scaffold for patterning nanoparticles has been widely reported and hence it is a plausible design. The influence of pitch of the gold nanohelix on its optical properties was demonstrated. SHG from the gold nanohelix was found to be 65 times stronger than that from a comparable gold nanorod. This example of designing a contrast agent for SHG and evaluating its performance theoretically can be applied to design a nano-scatterer with any other kind of optical activity. The coupled dipole model not only allows us to evaluate the optical properties of existing gold nanoparticles, but it will also help us to propose rational designs of scatterers for a specific application.

Apart from development of the coupled dipole model for nonlinear scattering, we also worked on strategies to target gold nanoparticles to biological cells with high specificity. For this purpose, gold nanorods were used as model particles and multiphoton luminescence microscopy was used to visualize the targeted cells. Gold nanorods were stabilized in biological buffers by coating them with polyethylene glycol (PEG). Amine terminated PEG was used for conjugating gold nanorods to antibody for epidermal growth factor receptor (anti-EGFR). It was further observed that only 50% of amine terminated PEG is necessary to achieve good targeting of cancer cells with minimal background. Finally, comparison of multiphoton luminescence microscopy of gold nanorods with two different excitation wavelengths, one (824 nm) close to the longitudinal plasmon resonance (LPR) of the nanorods and another (1200 nm) far away from the LPR, shows that the former causes more photothermal damage to cells. This photothermal damage is mostly due to LPR enhanced absorption of photons by the nanorods. The longer wavelength is weakly absorbed by gold nanorods and hence photothermal damage is minimal. The longer excitation wavelength also has advantage of deeper penetration into biological tissues. Therefore multiphoton microscopy of gold nanorods with excitation wavelengths centered around 1200 nm was found to be more suitable for bioimaging of tissues.

Chapter 7

Future directions

The coupled dipole model is a useful tool to understand nonlinear scattering from small particles. To the best of our knowledge, we are the first to use this method for simulating nonlinear scattering from small particles. Coupled dipole model is more accurate than the uncoupled dipole model but it is also computationally intensive. Reducing the computational time of coupled dipole model will enhance its utility. We can think of two ways to speed up the calculations of coupled dipole model – parallel computing[71] and graphic processor unit based computing. Both these methods speed up the computational task by dividing it into many small parts. These methods are especially useful when studying freely rotating nanoparticles in solution where a number of orientations of the particle have to be taken into account. These methods are also useful for calculating spectral response of a nanoparticle where a number of wavelengths are involved. Spectral response of a nanoparticle can also be used to calculate its temporal response to a short light pulse[197].

The coupled dipole model, like other numerical methods for nonlinear scattering, is qualitative in nature because nonlinear susceptibility data for most materials is not available. The nonlinear susceptibility of gold nanoparticles and its dependence of wavelength are important for quantitative prediction of nonlinear interactions between light and these particles. The second order susceptibility matrix of gold nanoparticles can be determined by hyper-Rayleigh scattering studies[198]. For example, the second order susceptibility of gold nanoparticles should give us complete information about the direction, polarization and magnitude of SHG. This information is essential for comparing gold nanoparticles with other kinds of contrast agents like fluorescent dyes, nonlinear nanocrystals, etc. Similarly third order susceptibility contains information of two photon absorption as well as third harmonic generation. Two photon microscopy of gold nanorods generally involves exciting the nanorods at their linear absorption maxima. This causes significant heating in the nanorods as demonstrated in chapter (5) of this thesis. With knowledge of third susceptibility of gold nanorods as a function of wavelength, it is perhaps possible to separate linear absorption maxima from two photon absorption maxima, thus minimizing the heat generated in the particles.

We used a gold nanohelix as an example to demonstrate how non-scatterers can be designed for second harmonic generation. There are a number of gold nanoparticles which can be synthesized in large quantities, but nonlinear optical properties of such particles have not been fully characterized. There are also new type of metal nanoparticles which are made of more than one metal[188]. All such particles can be studied using coupled dipole model and nanoparticles can be sorted according to their nonlinear optical properties. This will assist researchers in choosing nanoparticles with specific nonlinear activity. Comparing nanoparticles with a specific nonlinear activity will give us an insight to correlation between morphological features of nanoparticles and their optical properties.

Strong multiphoton luminescence of gold nanorods and emission in the red region of the spectrum is favorable for deep tissue imaging. We have also demonstrated multiphoton luminescence from gold nanorods can be excited with long excitation wavelengths around 1200 nm which are good for deep tissue imaging. With conventional fluorophores, multiphoton imaging in tissue can be performed up to depths of 1 mm[199]. If gold nanorods are used instead of fluorophores, depth of imaging in biological tissues can be further increased. Imaging depth can be even further increased by using techniques like adaptive optics which negate scattering by the tissue. Plasmonic probes for SHG are expected to further improve the imaging depth by selective back scattering.

Bibliography:

1. R. R. Anderson, and J. A. Parrish, "The Optics of Human Skin," J Investig Dermatol **77**, 13-19 (1981).

2. R. W. Boyd, *Nonlinear Optics* (Academic Press, 2008).

3. T. H. Maiman, "Stimulated Optical Radiation in Ruby," Nature **187**, 493-494 (1960).

4. J. Kerr, "A new relation between electricity and light: dielectrified media birefringent," Philos. Mag. **50**, 337-348 (1875).

5. M. Göppert-Mayer, "Über Elementarakte mit zwei Quantensprüngen," Annalen der Physik **401**, 273-294 (1931).

6. W. Kaiser, and C. G. B. Garrett, "Two-Photon Excitation in CaF_{2}: Eu^{2+}," Physical Review Letters **7**, 229-231 (1961).

7. P. A. Franken, A. E. Hill, C. W. Peters, and G. Weinreich, "Generation of Optical Harmonics," Physical Review Letters **7**, 118-119 (1961).

8. R. W. Terhune, P. D. Maker, and C. M. Savage, "Measurements of Nonlinear Light Scattering," Physical Review Letters **14**, 681 (1965).

9. R. W. Terhune, P. D. Maker, and C. M. Savage, "Optical Harmonic Generation in Calcite," Physical Review Letters **8**, 404-406 (1962).

10. N. Bloembergen, R. K. Chang, S. S. Jha, and C. H. Lee, "Optical Second-Harmonic Generation in Reflection from Media with Inversion Symmetry," Physical Review **174**, 813-822 (1968).

11. C. J. R. Sheppard, and R. Kompfner, "Resonant scanning optical microscope," Appl. Opt. **17**, 2879-2882 (1978).

12. J. N. Gannaway, and C. J. R. Sheppard, "Second-harmonic imaging in the scanning optical microscope," Optical and Quantum Electronics **10**, 435-439 (1978).

13. J. Valdmanis, and R. Fork, "Design considerations for a femtosecond pulse laser balancing self phase modulation, group velocity dispersion, saturable absorption, and saturable gain," Quantum Electronics, IEEE Journal of **22**, 112-118 (1986).

14. W. Denk, J. H. Strickler, and W. W. Webb, "Two-photon laser scanning fluorescence microscopy," Science **248**, 73-76 (1990).

15. B. R. Masters, and P. T. C. So, eds. *Handbook of Biomedical Nonlinear Optical Microscopy* (Oxford University Press, 2008).

16. J. Mertz, "Nonlinear microscopy: new techniques and applications," Current Opinion in Neurobiology **14**, 610-616 (2004).

17. F. Helmchen, and W. Denk, "Deep tissue two-photon microscopy," Nat Meth **2**, 932-940 (2005).

18. A. Diaspro, G. Chirico, and M. Collini, "Two-photon fluorescence excitation and related techniques in biological microscopy," Quarterly Reviews of Biophysics **38**, 97-166 (2006).

19. M. D. Cahalan, I. Parker, S. H. Wei, and M. J. Miller, "Real-time imaging of lymphocytes in vivo," Current Opinion in Immunology **15**, 372-377 (2003).

20. B. A. Molitoris, and R. M. Sandoval, "Intravital multiphoton microscopy of dynamic renal processes," Am J Physiol Renal Physiol **288**, F1084-1089-F1084-1089 (2005).

21. W.-C. A. Lee, H. Huang, G. Feng, J. R. Sanes, E. N. Brown, P. T. So, and E. Nedivi, "Dynamic Remodeling of Dendritic Arbors in GABAergic Interneurons of Adult Visual Cortex," PLoS Biology **4**, e29 EP --e29 EP - (2006).

22. B. R. Masters, P. T. So, and E. Gratton, "Multiphoton excitation fluorescence microscopy and spectroscopy of in vivo human skin," Biophysical journal **72**, 2405-2412 (1997).

23. K. König, "Clinical multiphoton tomography," Journal of Biophotonics **1**, 13-23 (2008).

24. P. J. Campagnola, A. C. Millard, M. Terasaki, P. E. Hoppe, C. J. Malone, and W. A. Mohler, "Three-Dimensional High-Resolution Second-Harmonic Generation Imaging of Endogenous Structural Proteins in Biological Tissues," Biophysical Journal **82**, 493-508 (2002).

25. R. M. Williams, W. R. Zipfel, and W. W. Webb, "Interpreting Second-Harmonic Generation Images of Collagen I Fibrils," Biophysical Journal **88**, 1377-1386 (2005).

26. E. Y. S. Yew, and C. J. R. Sheppard, "Second harmonic generation polarization microscopy with tightly focused linearly and radially polarized beams," Optics Communications **275**, 453-457 (2007).

27. M. Han, G. Giese, and J. Bille, "Second harmonic generation imaging of collagen fibrils in cornea and sclera," Opt. Express **13**, 5791-5797 (2005).

28. M. Winkler, B. Jester, C. Nien-Shy, S. Massei, D. S. Minckler, J. V. Jester, and D. J. Brown, "High resolution three-dimensional reconstruction of the collagenous matrix of the human optic nerve head," Brain Research Bulletin **81**, 339-348 (2010).

29. Y. He, C. H. Kang, S. Xu, X. Tuo, S. Trasti, D. C. S. Tai, A. M. Raja, Q. Peng, P. T. C. So, J. C. Rajapakse, R. Welsch, and H. Yu, "Toward surface quantification of liver fibrosis progression," Journal of Biomedical Optics **15**, 056007 (2010).

30. L. Moreaux, O. Sandre, and J. Mertz, "Membrane imaging by second-harmonic generation microscopy," J. Opt. Soc. Am. B **17**, 1685-1694 (2000).

31. B. E. Cohen, "Biological imaging: Beyond fluorescence," Nature **467**, 407-408 (2011).

32. R. Grange, T. Lanvin, C.-L. Hsieh, Y. Pu, and D. Psaltis, "Imaging with second-harmonic radiation probes in living tissue," Biomed. Opt. Express **2**, 2532-2539 (2011).

33. P. Pantazis, J. Maloney, D. Wu, and S. E. Fraser, "Second harmonic generating (SHG) nanoprobes for in vivo imaging," Proceedings of the National Academy of Sciences **107**, 14535-14540 (2011).

34. R. Jin, J. E. Jureller, H. Y. Kim, and N. F. Scherer, "Correlating Second Harmonic Optical Responses of Single Ag Nanoparticles with Morphology," Journal of the American Chemical Society **127**, 12482-12483 (2005).

35. J. Butet, G. Bachelier, J. Duboisset, F. Bertorelle, I. Russier-Antoine, C. Jonin, E. Benichou, and P.-F. Brevet, "Three-dimensional mapping of single gold nanoparticles embedded in a homogeneous transparent matrix using optical second-harmonic generation," Opt. Express **18**, 22314-22323 (2010).

36. J. Yguerabide, and E. E. Yguerabide, "Light-Scattering Submicroscopic Particles as Highly Fluorescent Analogs and Their Use as Tracer Labels in Clinical and Biological Applications: I. Theory," Analytical Biochemistry **262**, 137-156 (1998).

37. J. Yguerabide, and E. E. Yguerabide, "Light-Scattering Submicroscopic Particles as Highly Fluorescent Analogs and Their Use as Tracer Labels in Clinical and Biological Applications: II. Experimental Characterization," Analytical Biochemistry **262**, 157-176 (1998).

38. C. L. Nehl, and J. H. Hafner, "Shape-dependent plasmon resonances of gold nanoparticles," Journal of Materials Chemistry **18**, 2415-2419 (2008).

39. N. Felidj, J. Aubard, and G. Levi, "Discrete dipole approximation for ultraviolet--visible extinction spectra simulation of silver and gold colloids," The Journal of Chemical Physics **111**, 1195-1208 (1999).

40. J. M. EllenÿE. Connor, "Gold Nanoparticles Are Taken Up by Human Cells but Do Not Cause Acute Cytotoxicity13," Small **1**, 325-327 (2005).

41. R. Shukla, V. Bansal, M. Chaudhary, A. Basu, R. R. Bhonde, and M. Sastry, "Biocompatibility of Gold Nanoparticles and Their Endocytotic Fate Inside the Cellular Compartment: A Microscopic Overview," Langmuir **21**, 10644-10654 (2005).

42. J. C. Y. Kah, C. J. R. Sheppard, C. G. L. Lee, and M. C. Olivo, "Application of antibody-conjugated gold nanoparticles for optical molecular imaging of epithelial carcinoma cells," in *Nanobiophotonics and Biomedical Applications III*(SPIE, San Jose, CA, USA, 2006), pp. 609503-609506.

43. K. Sokolov, M. Follen, J. Aaron, I. Pavlova, A. Malpica, R. Lotan, and R. Richards-Kortum, "Real-Time Vital Optical Imaging of Precancer Using Anti-Epidermal Growth Factor Receptor Antibodies Conjugated to Gold Nanoparticles," Cancer Res **63**, 1999-2004 (2003).

44. A. W. H. Lin, N. A. Lewinski, J. L. West, N. J. Halas, and R. A. Drezek, "Optically tunable nanoparticle contrast agents for early cancer detection: model-based analysis of gold nanoshells," Journal of Biomedical Optics **10**, 064035-064010 (2005).

45. J. C. Y. Kah, M. Olivo, T. H. Chow, K. S. Song, K. Z. Y. Koh, S. Mhaisalkar, and C. J. R. Sheppard, "Control of optical contrast using gold nanoshells for optical coherence tomography imaging of mouse xenograft tumor model in vivo," Journal of Biomedical Optics **14**, 054015-054013 (2009).

46. M. B. Mohamed, V. Volkov, S. Link, and M. A. El-Sayed, "The `lightning' gold nanorods: fluorescence enhancement of over a million

compared to the gold metal," Chemical Physics Letters **317**, 517-523 (2000).

47. H. Wang, T. B. Huff, D. A. Zweifel, W. He, P. S. Low, A. Wei, and J.-X. Cheng, "In vitro and in vivo two-photon luminescence imaging of single gold nanorods," Proceedings of the National Academy of Sciences of the United States of America **102**, 15752-15756 (2005).

48. Y. Kim, R. C. Johnson, and J. T. Hupp, "Gold Nanoparticle-Based Sensing of "Spectroscopically Silent" Heavy Metal Ions," Nano Letters **1**, 165-167 (2001).

49. H. Wang, D. W. Brandl, P. Nordlander, and N. J. Halas, "Plasmonic Nanostructures: Artificial Molecules," Accounts of Chemical Research **40**, 53-62 (2007).

50. B. T. Draine, and P. J. Flatau, "Discrete-dipole approximation for scattering calculations," J. Opt. Soc. Am. A **11**, 1491-1499 (1994).

51. E. Adler, "Nonlinear Optical Frequency Polarization in a Dielectric," Physical Review **134**, A728 (1964).

52. G. S. Agarwal, and S. S. Jha, "Theory of second harmonic generation at a metal surface with surface plasmon excitation," Solid State Communications **41**, 499-501 (1982).

53. X. M. Hua, and J. I. Gersten, "Theory of second-harmonic generation by small metal spheres," Physical Review B **33**, 3756 (1986).

54. O. A. Aktsipetrov, P. V. Elyutin, A. A. Nikulin, and E. A. Ostrovskaya, "Size effects in optical second-harmonic generation by metallic nanocrystals and semiconductor quantum dots: The role of quantum chaotic dynamics," Physical Review B **51**, 17591 (1995).

55. A. Guerrero, and B. S. Mendoza, "Model for great enhancement of second-harmonic generation in quantum dots," J. Opt. Soc. Am. B **12**, 559-569 (1995).

56. V. L. Brudny, B. S. Mendoza, and W. Luis Mochán, "Second-harmonic generation from spherical particles," Physical Review B **62**, 11152 (2000).

57. W. L. Mochán, J. A. Maytorena, B. S. Mendoza, and V. L. Brudny, "Second-harmonic generation in arrays of spherical particles," Physical Review B **68**, 085318 (2003).

58. D. Östling, P. Stampfli, and K. H. Bennemann, "Theory of nonlinear optical properties of small metallic spheres," Zeitschrift für Physik D Atoms, Molecules and Clusters **28**, 169-175 (1993).

59. H. Wang, E. C. Y. Yan, E. Borguet, and K. B. Eisenthal, "Second harmonic generation from the surface of centrosymmetric particles in bulk solution," Chemical Physics Letters **259**, 15-20 (1996).

60. J. Martorell, R. Vilaseca, and R. Corbalán, "Scattering of second-harmonic light from small spherical particles ordered in a crystalline lattice," Physical Review A **55**, 4520 (1997).

61. N. Yang, W. E. Angerer, and A. G. Yodh, "Angle-Resolved Second-Harmonic Light Scattering from Colloidal Particles," Physical Review Letters **87**, 103902 (2001).

62. J. I. Dadap, J. Shan, K. B. Eisenthal, and T. F. Heinz, "Second-Harmonic Rayleigh Scattering from a Sphere of Centrosymmetric Material," Physical Review Letters **83**, 4045 (1999).

63. J. I. Dadap, J. Shan, and T. F. Heinz, "Theory of optical second-harmonic generation from a sphere of centrosymmetric material: small-particle limit," J. Opt. Soc. Am. B **21**, 1328-1347 (2004).

64. N. J. Durr, T. Larson, D. K. Smith, B. A. Korgel, K. Sokolov, and A. Ben-Yakar, "Two-Photon Luminescence Imaging of Cancer Cells Using Molecularly Targeted Gold Nanorods," Nano Lett. **7**, 941-945 (2007).

65. Y. Jung, H. Chen, L. Tong, and J.-X. Cheng, "Imaging Gold Nanorods by Plasmon-Resonance-Enhanced Four Wave Mixing," The Journal of Physical Chemistry C **113**, 2657-2663 (2009).

66. A. Wijaya, S. B. Schaffer, I. G. Pallares, and K. Hamad-Schifferli, "Selective Release of Multiple DNA Oligonucleotides from Gold Nanorods," ACS Nano **3**, 80-86 (2009).

67. Purcell, E. M., and Pennypacker, C. R., "Scattering and Absorption of Light by Nonspherical Dielectric Grains," Astrophysical Journal **186**, 705-714 (1973).

68. Draine, B. T., "The discrete-dipole approximation and its application to interstellar graphite grains," Astrophysical Journal **333**, 848-872 (1988).

69. J. J. Goodman, B. T. Draine, and P. J. Flatau, "Application of fast-Fourier-transform techniques to the discrete-dipole approximation," Opt. Lett. **16**, 1198-1200 (1991).

70. B. T. Draine, and P. J. Flatau, "User Guide for the Discrete Dipole Approximation Code DDSCAT 7.0," (2008).

71. A. G. Hoekstra, and P. M. A. Sloot, "Coupled dipole simulations of elastic light scattering on parallel systems," International Journal of Modern Physics C **6**, 663-679 (1995).

72. A. G. Hoekstra, M. D. Grimminck, and P. M. A. Sloot, "Large Scale Simulations of Elastic Light Scattering by a Fast Discrete Dipole Approximation," International Journal of Modern Physics C **9**, 87-102 (1998).

73. Lakhtakia, A., "General theory of the Purcell-Pennypacker scattering approach and its extension to bianisotropic scatterers," The Astrophysical Journal **394**, 494-499 (1992).

74. N. Arzate, B. S. Mendoza, and R. A. Vázquez-Nava, "Polarizable dipole models for reflectance anisotropy spectroscopy: a review," Journal of Physics: Condensed Matter **16**, S4259 (2004).

75. W.-H. Yang, G. C. Schatz, and R. P. Van Duyne, "Discrete dipole approximation for calculating extinction and Raman intensities for small particles with arbitrary shapes," The Journal of Chemical Physics **103**, 869-875 (1995).

76. K. L. Kelly, E. Coronado, L. L. Zhao, and G. C. Schatz, "The Optical Properties of Metal Nanoparticles: The Influence of Size, Shape, and Dielectric Environment," Journal of Physical Chemistry B **107**, 668-677 (2003).

77. P. K. Jain, K. S. Lee, I. H. El-Sayed, and M. A. El-Sayed, "Calculated Absorption and Scattering Properties of Gold Nanoparticles of Different Size, Shape, and Composition: Applications in Biological Imaging and Biomedicine," The Journal of Physical Chemistry B **110**, 7238-7248 (2006).

78. S. W. Prescott, and P. Mulvaney, "Gold nanorod extinction spectra," Journal of Applied Physics **99**, 123504-123507 (2006).

79. B. T. Draine, and P. J. Flatau, "Discrete-dipole approximation for periodic targets: theory and tests," J. Opt. Soc. Am. A **25**, 2693-2703 (2008).

80. F. Bordas, N. Louvion, S. Callard, P. C. Chaumet, and A. Rahmani, "Coupled dipole method for radiation dynamics in finite photonic crystal structures," Physical Review E **73**, 056601 (2006).

81. D. A. Smith, and K. L. Stokes, "Discrete dipole approximation for magneto-opticalscattering calculations," Opt. Express **14**, 5746-5754 (2006).

82. Y. You, G. W. Kattawar, and P. Yang, "Invisibility cloaks for toroids," Opt. Express **17**, 6591-6599 (2009).

83. M. A. Yurkin, K. A. Semyanov, P. A. Tarasov, A. V. Chernyshev, A. G. Hoekstra, and V. P. Maltsev, "Experimental and theoretical study of light scattering by individual mature red blood cells by use of scanning flow cytometry and a discrete dipole approximation," Appl. Opt. **44**, 5249-5256 (2005).

84. P. C. Chaumet, A. Rahmani, A. Sentenac, and G. W. Bryant, "Efficient computation of optical forces with the coupled dipole method," Physical Review E **72**, 046708 (2005).

85. P. Flatau, "Fast solvers for one dimensional light scattering in the discrete dipole approximation," Opt. Express **12**, 3149-3155 (2004).

86. P. J. Flatau, "Improvements in the discrete-dipole approximation method of computing scattering and absorption," Opt. Lett. **22**, 1205-1207 (1997).

87. C. M. J. Wijers, T. Rasing, and R. W. J. Hollering, "Second harmonic generation from thin slabs in the discrete dipole approach," Solid state communications **85**, 233-237 (1993).

88. E. Y. Poliakov, V. A. Markel, V. M. Shalaev, and R. Botet, "Nonlinear optical phenomena on rough surfaces of metal thin films," Physical Review B **57**, 14901 (1998).

89. J.-X. Cheng, and X. S. Xie, "Green's function formulation for third-harmonic generation microscopy," J. Opt. Soc. Am. B **19**, 1604-1610 (2002).

90. N. P. Blanchard, C. Smith, D. S. Martin, D. J. Hayton, T. E. Jenkins, and P. Weightman, "High-resolution measurements of the bulk dielectric constants of single crystal gold with application to reflection anisotropy spectroscopy," Physica Status Solidi (c) **0**, 2931-2937 (2003).

91. G. Bachelier, I. Russier-Antoine, E. Benichou, C. Jonin, and P.-F. Brevet, "Multipolar second-harmonic generation in noble metal nanoparticles," J. Opt. Soc. Am. B **25**, 955-960 (2008).

92. J. Nappa, G. Revillod, I. Russier-Antoine, E. Benichou, C. Jonin, and P. F. Brevet, "Electric dipole origin of the second harmonic generation of small metallic particles," Physical Review B **71**, 165407-165404 (2005).

93. I. Russier-Antoine, E. Benichou, G. Bachelier, C. Jonin, and P. F. Brevet, "Multipolar Contributions of the Second Harmonic Generation from Silver and Gold Nanoparticles," The Journal of Physical Chemistry C **111**, 9044-9048 (2007).

94. K. B. Eisenthal, "Liquid Interfaces Probed by Second-Harmonic and Sum-Frequency Spectroscopy," Chemical Reviews **96**, 1343-1360 (1996).

95. K. B. Eisenthal, "Second Harmonic Spectroscopy of Aqueous Nano- and Microparticle Interfaces," Chemical Reviews **106**, 1462-1477 (2006).

96. P. J. Campagnola, M.-d. Wei, A. Lewis, and L. M. Loew, "High-Resolution Nonlinear Optical Imaging of Live Cells by Second Harmonic Generation," Biophysical Journal **77**, 3341-3349 (1999).

97. A. Zoumi, A. Yeh, and B. J. Tromberg, "Imaging cells and extracellular matrix in vivo by using second-harmonic generation and two-photon excited fluorescence," Proceedings of the National Academy of Sciences of the United States of America **99**, 11014-11019 (2002).

98. S. V. Plotnikov, A. C. Millard, P. J. Campagnola, and W. A. Mohler, "Characterization of the Myosin-Based Source for Second-Harmonic Generation from Muscle Sarcomeres," Biophysical Journal **90**, 693-703 (2006).

99. E. Brown, T. McKee, E. diTomaso, A. Pluen, B. Seed, Y. Boucher, and R. K. Jain, "Dynamic imaging of collagen and its modulation in tumors in vivo using second-harmonic generation," Nat Med **9**, 796-800 (2003).

100. W. R. Zipfel, R. M. Williams, R. Christie, A. Y. Nikitin, B. T. Hyman, and W. W. Webb, "Live tissue intrinsic emission microscopy using multiphoton-excited native fluorescence and second harmonic

generation," Proceedings of the National Academy of Sciences **100**, 7075-7080 (2003).

101. Y. Barad, H. Eisenberg, M. Horowitz, and Y. Silberberg, "Nonlinear scanning laser microscopy by third harmonic generation," Applied Physics Letters **70**, 922 (1997).

102. J. Squier, M. Muller, G. Brakenhoff, and K. R. Wilson, "Third harmonic generation microscopy," Opt. Express **3**, 315-324 (1998).

103. D. Yelin, and Y. Silberberg, "Laser scanning third-harmonic-generation microscopy in biology," Opt. Express **5**, 169-175 (1999).

104. S.-W. Chu, S.-Y. Chen, T.-H. Tsai, T.-M. Liu, C.-Y. Lin, H.-J. Tsai, and C.-K. Sun, "In vivo developmental biology study using noninvasive multi-harmonic generation microscopy," Opt. Express **11**, 3093-3099 (2003).

105. D. Débarre, W. Supatto, E. Farge, B. Moulia, M.-C. Schanne-Klein, and E. Beaurepaire, "Velocimetric third-harmonic generation microscopy: micrometer-scalequantification of morphogenetic movements in unstained embryos," Opt. Lett. **29**, 2881-2883 (2004).

106. D. Oron, D. Yelin, E. Tal, S. Raz, R. Fachima, and Y. Silberberg, "Depth-resolved structural imaging by third-harmonic generation microscopy," Journal of Structural Biology **147**, 3-11 (2004).

107. M. D. Duncan, J. Reintjes, and T. J. Manuccia, "Scanning coherent anti-Stokes Raman microscope," Opt. Lett. **7**, 350-352 (1982).

108. A. Zumbusch, G. R. Holtom, and X. S. Xie, "Three-Dimensional Vibrational Imaging by Coherent Anti-Stokes Raman Scattering," Physical Review Letters **82**, 4142 (1999).

109. P. D. Maker, and R. W. Terhune, "Study of Optical Effects Due to an Induced Polarization Third Order in the Electric Field Strength," Physical Review **137**, A801 (1965).

110. J.-X. Cheng, Y. K. Jia, G. Zheng, and X. S. Xie, "Laser-Scanning Coherent Anti-Stokes Raman Scattering Microscopy and Applications to Cell Biology," Biophysical Journal **83**, 502-509 (2002).

111. H. A. Rinia, K. N. J. Burger, M. Bonn, and M. Müller, "Quantitative Label-Free Imaging of Lipid Composition and Packing of Individual

Cellular Lipid Droplets Using Multiplex CARS Microscopy," Biophysical Journal **95**, 4908-4914 (2008).

112. J. Mertz, and L. Moreaux, "Second-harmonic generation by focused excitation of inhomogeneously distributed scatterers," Optics Communications **196**, 325-330 (2001).

113. L. Moreaux, O. Sandre, M. Blanchard-Desce, and J. Mertz, "Membrane imaging by simultaneous second-harmonic generation and two-photon microscopy," Opt. Lett. **25**, 320-322 (2000).

114. E. Yew, and C. Sheppard, "Effects of axial field components on second harmonic generation microscopy," Opt. Express **14**, 1167-1174 (2006).

115. J.-X. Cheng, A. Volkmer, and X. S. Xie, "Theoretical and experimental characterization of coherent anti-Stokes Raman scattering microscopy," J. Opt. Soc. Am. B **19**, 1363-1375 (2002).

116. N. K. Balla, P. T. C. So, and C. J. R. Sheppard, "Second harmonic scattering from small particles using Discrete Dipole Approximation," Opt. Express **18**, 21603-21611 (2010).

117. B. Richards, and E. Wolf, "Electromagnetic Diffraction in Optical Systems. II. Structure of the Image Field in an Aplanatic System," Proceedings of the Royal Society of London. Series A. Mathematical and Physical Sciences **253**, 358-379 (1959).

118. S.-W. Chu, S.-Y. Chen, G.-W. Chern, T.-H. Tsai, Y.-C. Chen, B.-L. Lin, and C.-K. Sun, "Studies of ◎$^{(2)}$/◎$^{(3)}$ Tensors in Submicron-Scaled Bio-Tissues by Polarization Harmonics Optical Microscopy," Biophysical journal **86**, 3914-3922 (2004).

119. D. W. Leonard, and K. M. Meek, "Refractive indices of the collagen fibrils and extrafibrillar material of the corneal stroma," Biophysical Journal **72**, 1382-1387 (1997).

120. K. Takeda, and et al., "Simultaneous measurement of size and refractive index of a fine particle in flowing liquid," Measurement Science and Technology **3**, 27 (1992).

121. R. W. Boyd, "The Nonlinear Optical Susceptibility," in *Nonlinear Optics (Third Edition)*(Academic Press, Burlington, 2008), pp. 1-67.

122. C. Liu, Z. Huang, F. Lu, W. Zheng, D. W. Hutmacher, and C. Sheppard, "Near-field effects on coherent anti-Stokes Raman scattering microscopy imaging," Opt. Express **15**, 4118-4131 (2007).

123. D. Débarre, W. Supatto, and E. Beaurepaire, "Structure sensitivity in third-harmonic generation microscopy," Opt. Lett. **30**, 2134-2136 (2005).

124. J.-X. Cheng, and X. S. Xie, "Coherent Anti-Stokes Raman Scattering Microscopy: Instrumentation, Theory, and Applications," The Journal of Physical Chemistry B **108**, 827-840 (2003).

125. N. Djaker, D. Gachet, N. Sandeau, P.-F. Lenne, and H. Rigneault, "Refractive effects in coherent anti-Stokes Raman scattering microscopy," Appl. Opt. **45**, 7005-7011 (2006).

126. S. J. Oldenburg, R. D. Averitt, S. L. Westcott, and N. J. Halas, "Nanoengineering of optical resonances," Chemical Physics Letters **288**, 243-247 (1998).

127. N. R. Jana, L. Gearheart, and C. J. Murphy, "Wet Chemical Synthesis of High Aspect Ratio Cylindrical Gold Nanorods," The Journal of Physical Chemistry B **105**, 4065-4067 (2001).

128. B. Nikoobakht, and M. A. El-Sayed, "Preparation and Growth Mechanism of Gold Nanorods (NRs) Using Seed-Mediated Growth Method," Chemistry of Materials **15**, 1957-1962 (2003).

129. S. J. Oldenburg, J. B. Jackson, S. L. Westcott, and N. J. Halas, "Infrared extinction properties of gold nanoshells," Applied Physics Letters **75**, 2897-2899 (1999).

130. D. A. Schultz, "Plasmon resonant particles for biological detection," Current Opinion in Biotechnology **14**, 13-22 (2003).

131. K. Sokolov, M. Follen, J. Aaron, I. Pavlova, A. Malpica, R. Lotan, and R. Richards-Kortum, "Real-Time Vital Optical Imaging of Precancer Using Anti-Epidermal Growth Factor Receptor Antibodies Conjugated to Gold Nanoparticles," Cancer Research **63**, 1999-2004 (2003).

132. J. C. Y. Kah, M. C. Olivo, C. G. L. Lee, and C. J. R. Sheppard, "Molecular contrast of EGFR expression using gold nanoparticles as a reflectance-based imaging probe," Molecular and Cellular Probes **22**, 14-23 (2008).

133. A. Bouhelier, R. Bachelot, G. Lerondel, S. Kostcheev, P. Royer, and G. P. Wiederrecht, "Surface Plasmon Characteristics of Tunable Photoluminescence in Single Gold Nanorods," Physical Review Letters **95**, 267405 (2005).

134. P. C. Ray, "Size and Shape Dependent Second Order Nonlinear Optical Properties of Nanomaterials and Their Application in Biological and Chemical Sensing," Chemical Reviews **110**, 5332-5365 (2010).

135. K. Clays, A. Persoons, and eacute, "Hyper-Rayleigh scattering in solution," Physical Review Letters **66**, 2980 (1991).

136. F. W. Vance, B. I. Lemon, and J. T. Hupp, "Enormous Hyper-Rayleigh Scattering from Nanocrystalline Gold Particle Suspensions," J. Phys. Chem. B **102**, 10091-10093 (1998).

137. A. J. Mastroianni, S. A. Claridge, and A. P. Alivisatos, "Pyramidal and Chiral Groupings of Gold Nanocrystals Assembled Using DNA Scaffolds," Journal of the American Chemical Society **131**, 8455-8459 (2009).

138. V. K. Valev, N. Smisdom, A. V. Silhanek, B. De Clercq, W. Gillijns, M. Ameloot, V. V. Moshchalkov, and T. Verbiest, "Plasmonic Ratchet Wheels: Switching Circular Dichroism by Arranging Chiral Nanostructures," Nano Letters **9**, 3945-3948 (2009).

139. B. Canfield, S. Kujala, K. Jefimovs, J. Turunen, and M. Kauranen, "Linear and nonlinear optical responses influenced by broken symmetry in an array of gold nanoparticles," Opt. Express **12**, 5418-5423 (2004).

140. B. K. Canfield, H. Husu, J. Laukkanen, B. Bai, M. Kuittinen, J. Turunen, and M. Kauranen, "Local Field Asymmetry Drives Second-Harmonic Generation in Noncentrosymmetric Nanodimers," Nano Letters **7**, 1251-1255 (2007).

141. C. J. Addison, S. O. Konorov, A. G. Brolo, M. W. Blades, and R. F. B. Turner, "Tuning Gold Nanoparticle Self-Assembly for Optimum Coherent Anti-Stokes Raman Scattering and Second Harmonic Generation Response," The Journal of Physical Chemistry C **113**, 3586-3592 (2009).

142. H. A. Clark, P. J. Campagnola, J. P. Wuskell, A. Lewis, and L. M. Loew, "Second Harmonic Generation Properties of Fluorescent Polymer-

Encapsulated Gold Nanoparticles," Journal of the American Chemical Society **122**, 10234-10235 (2000).

143. K. Chen, C. Durak, J. R. Heflin, and H. D. Robinson, "Plasmon-Enhanced Second-Harmonic Generation from Ionic Self-Assembled Multilayer Films," Nano Letters **7**, 254-258 (2007).

144. M. Ishifuji, M. Mitsuishi, and T. Miyashita, "Second harmonic generation from multilayered hybrid polymer nanoassemblies enhanced by coupled surface plasmon resonance," Chem. Commun., 1058-1060 (2008).

145. F. Westerlund, and T. Bjørnholm, "Directed assembly of gold nanoparticles," Current Opinion in Colloid & Interface Science **14**, 126-134 (2009).

146. R. Chhabra, J. Sharma, Y. Liu, S. Rinker, and H. Yan, "DNA Self-assembly for Nanomedicine," Advanced Drug Delivery Reviews **62**, 617-625 (2010).

147. X. Fu, Y. Wang, L. Huang, Y. Sha, L. Gui, L. Lai, and Y. Tang, "Assemblies of Metal Nanoparticles and Self-Assembled Peptide Fibrils—Formation of Double Helical and Single-Chain Arrays of Metal Nanoparticles," Advanced Materials **15**, 902-906 (2003).

148. C.-L. Chen, and N. L. Rosi, "Preparation of Unique 1-D Nanoparticle Superstructures and Tailoring their Structural Features," Journal of the American Chemical Society **132**, 6902-6903 (2010).

149. E. Dujardin, C. Peet, G. Stubbs, J. N. Culver, and S. Mann, "Organization of Metallic Nanoparticles Using Tobacco Mosaic Virus Templates," Nano Letters **3**, 413-417 (2003).

150. L. Sang-Yup, and et al., "Improved metal cluster deposition on a genetically engineered tobacco mosaic virus template," Nanotechnology **16**, S435 (2005).

151. T. L. Schlick, Z. Ding, E. W. Kovacs, and M. B. Francis, "Dual-Surface Modification of the Tobacco Mosaic Virus," Journal of the American Chemical Society **127**, 3718-3723 (2005).

152. A. S. Blum, C. M. Soto, C. D. Wilson, J. D. Cole, M. Kim, B. Gnade, A. Chatterji, W. F. Ochoa, T. Lin, J. E. Johnson, and B. R. Ratna, "Cowpea Mosaic Virus as a Scaffold for 3-D Patterning of Gold Nanoparticles," Nano Letters **4**, 867-870 (2004).

153. K. N. Avery, J. E. Schaak, and R. E. Schaak, "M13 Bacteriophage as a Biological Scaffold for Magnetically-Recoverable Metal Nanowire Catalysts: Combining Specific and Nonspecific Interactions To Design Multifunctional Nanocomposites," Chemistry of Materials **21**, 2176-2178 (2009).

154. S. R. Whaley, D. S. English, E. L. Hu, P. F. Barbara, and A. M. Belcher, "Selection of peptides with semiconductor binding specificity for directed nanocrystal assembly," Nature **405**, 665-668 (2000).

155. S.-W. Lee, C. Mao, C. E. Flynn, and A. M. Belcher, "Ordering of Quantum Dots Using Genetically Engineered Viruses," Science **296**, 892-895 (2002).

156. C. Mao, D. J. Solis, B. D. Reiss, S. T. Kottmann, R. Y. Sweeney, A. Hayhurst, G. Georgiou, B. Iverson, and A. M. Belcher, "Virus-Based Toolkit for the Directed Synthesis of Magnetic and Semiconducting Nanowires," Science **303**, 213-217 (2004).

157. J. D. Lewis, G. Destito, A. Zijlstra, M. J. Gonzalez, J. P. Quigley, M. Manchester, and H. Stuhlmann, "Viral nanoparticles as tools for intravital vascular imaging," Nat Med **12**, 354-360 (2006).

158. A.-M. Pena, T. Boulesteix, T. Dartigalongue, and M.-C. Schanne-Klein, "Chiroptical Effects in the Second Harmonic Signal of Collagens I and IV," Journal of the American Chemical Society **127**, 10314-10322 (2005).

159. A. Deniset-Besseau, J. Duboisset, E. Benichou, F. o. Hache, P.-F. o. Brevet, and M.-C. Schanne-Klein, "Measurement of the Second-Order Hyperpolarizability of the Collagen Triple Helix and Determination of Its Physical Origin," The Journal of Physical Chemistry B **113**, 13437-13445 (2009).

160. J. K. Gansel, M. Thiel, M. S. Rill, M. Decker, K. Bade, V. Saile, G. von Freymann, S. Linden, and M. Wegener, "Gold Helix Photonic Metamaterial as Broadband Circular Polarizer," Science **325**, 1513-1515 (2009).

161. Z. Y. Zhang, and Y. P. Zhao, "Optical properties of helical Ag nanostructures calculated by discrete dipole approximation method," Applied Physics Letters **90**, 221501-221503 (2007).

162. A. Ashkin, and J. M. Dziedzic, "Optical trapping and manipulation of viruses and bacteria," Science **235**, 1517-1520 (1987).

163. J. M. Harris, N. E. Martin, and M. Modi, "Pegylation: A Novel Process for Modifying Pharmacokinetics," Clinical Pharmacokinetics **40**, 539-551 (2001).

164. H. Liao, and J. H. Hafner, "Gold Nanorod Bioconjugates," Chemistry of Materials **17**, 4636-4641 (2005).

165. R. G. Nuzzo, B. R. Zegarski, and L. H. Dubois, "Fundamental studies of the chemisorption of organosulfur compounds on gold(111). Implications for molecular self-assembly on gold surfaces," Journal of the American Chemical Society **109**, 733-740 (1987).

166. T. B. Huff, M. N. Hansen, Y. Zhao, J.-X. Cheng, and A. Wei, "Controlling the Cellular Uptake of Gold Nanorods," Langmuir **23**, 1596-1599 (2007).

167. T. Niidome, M. Yamagata, Y. Okamoto, Y. Akiyama, H. Takahashi, T. Kawano, Y. Katayama, and Y. Niidome, "PEG-modified gold nanorods with a stealth character for in vivo applications," Journal of Controlled Release **114**, 343-347 (2006).

168. L. van Vlerken, T. Vyas, and M. Amiji, "Poly(ethylene glycol)-modified Nanocarriers for Tumor-targeted and Intracellular Delivery," Pharmaceutical Research **24**, 1405-1414 (2007).

169. T. Niidome, Y. Akiyama, M. Yamagata, T. Kawano, T. Mori, Y. Niidome, and Y. Katayama, "Poly(ethylene glycol)-Modified Gold Nanorods as a Photothermal Nanodevice for Hyperthermia," Journal of Biomaterials Science, Polymer Edition **20**, 1203-1215 (2009).

170. L. Tong, W. He, Y. Zhang, W. Zheng, and J.-X. Cheng, "Visualizing Systemic Clearance and Cellular Level Biodistribution of Gold Nanorods by Intrinsic Two-Photon Luminescence," Langmuir **25**, 12454-12459 (2009).

171. A. Mooradian, "Photoluminescence of Metals," Physical Review Letters **22**, 185 (1969).

172. C. K. Chen, A. R. B. de Castro, and Y. R. Shen, "Surface-Enhanced Second-Harmonic Generation," Physical Review Letters **46**, 145 (1981).

173. G. T. Boyd, Z. H. Yu, and Y. R. Shen, "Photoinduced luminescence from the noble metals and its enhancement on roughened surfaces," Physical Review B **33**, 7923 (1986).

174. M. R. Beversluis, A. Bouhelier, and L. Novotny, "Continuum generation from single gold nanostructures through near-field mediated intraband transitions," Physical Review B **68**, 115433 (2003).

175. M. D. Wissert, K. S. Ilin, M. Siegel, U. Lemmer, and H.-J. Eisler, "Highly localized non-linear optical white-light response at nanorod ends from non-resonant excitation," Nanoscale **2**, 1018-1020 (2010).

176. K. Imura, T. Nagahara, and H. Okamoto, "Near-Field Two-Photon-Induced Photoluminescence from Single Gold Nanorods and Imaging of Plasmon Modes," The Journal of Physical Chemistry B **109**, 13214-13220 (2005).

177. D. Yelin, D. Oron, S. Thiberge, E. Moses, and Y. Silberberg, "Multiphoton plasmon-resonance microscopy," Opt. Express **11**, 1385-1391 (2003).

178. C. Sonnichsen, T. Franzl, T. Wilk, G. von Plessen, J. Feldmann, O. Wilson, and P. Mulvaney, "Drastic Reduction of Plasmon Damping in Gold Nanorods," Physical Review Letters **88**, 077402 (2002).

179. A. Bouhelier, M. R. Beversluis, and L. Novotny, "Characterization of nanoplasmonic structures by locally excited photoluminescence," Applied Physics Letters **83**, 5041-5043 (2003).

180. K. Imura, T. Nagahara, and H. Okamoto, "Plasmon Mode Imaging of Single Gold Nanorods," Journal of the American Chemical Society **126**, 12730-12731 (2004).

181. M. A. Albota, C. Xu, and W. W. Webb, "Two-Photon Fluorescence Excitation Cross Sections of Biomolecular Probes from 690 to 960 nm," Appl. Opt. **37**, 7352-7356 (1998).

182. S. Link, C. Burda, M. B. Mohamed, B. Nikoobakht, and M. A. El-Sayed, "Laser Photothermal Melting and Fragmentation of Gold Nanorods: Energy and Laser Pulse-Width Dependence," The Journal of Physical Chemistry A **103**, 1165-1170 (1999).

183. C.-H. Chou, C.-D. Chen, and C. R. C. Wang, "Highly Efficient, Wavelength-Tunable, Gold Nanoparticle Based Optothermal Nanoconvertors," The Journal of Physical Chemistry B **109**, 11135-11138 (2005).

184. X. Huang, I. H. El-Sayed, W. Qian, and M. A. El-Sayed, "Cancer Cell Imaging and Photothermal Therapy in the Near-Infrared Region by

Using Gold Nanorods," Journal of the American Chemical Society **128**, 2115-2120 (2006).

185. T. B. Huff, L. Tong, Y. Zhao, M. N. Hansen, J.-X. Cheng, and A. Wei, "Hyperthermic effects of gold nanorods on tumor cells," Nanomedicine **2**, 125-132 (2007).

186. L. Tong, Y. Zhao, T. B. Huff, M. N. Hansen, A. Wei, and J. X. Cheng, "Gold Nanorods Mediate Tumor Cell Death by Compromising Membrane Integrity," Advanced Materials **19**, 3136-3141 (2007).

187. G. von Maltzahn, J.-H. Park, A. Agrawal, N. K. Bandaru, S. K. Das, M. J. Sailor, and S. N. Bhatia, "Computationally Guided Photothermal Tumor Therapy Using Long-Circulating Gold Nanorod Antennas," Cancer Research **69**, 3892-3900 (2009).

188. K.-W. Hu, T.-M. Liu, K.-Y. Chung, K.-S. Huang, C.-T. Hsieh, C.-K. Sun, and C.-S. Yeh, "Efficient Near-IR Hyperthermia and Intense Nonlinear Optical Imaging Contrast on the Gold Nanorod-in-Shell Nanostructures," Journal of the American Chemical Society **131**, 14186-14187 (2009).

189. L. Tong, C. M. Cobley, J. Chen, Y. Xia, and J.-X. Cheng, "Bright Three-Photon Luminescence from Gold/Silver Alloyed Nanostructures for Bioimaging with Negligible Photothermal Toxicity," Angewandte Chemie International Edition **49**, 3485-3488 (2010).

190. B. E. Bouma, G. J. Tearney, I. P. Bilinsky, B. Golubovic, and J. G. Fujimoto, "Self-phase-modulated Kerr-lens mode-locked Cr:forsterite laser source for optical coherence tomography," Opt. Lett. **21**, 1839-1841 (1996).

191. P. Cheng, "Highly efficient upconverters for multiphoton fluorescence microscopy," Journal of Microscopy **189**, 199-212 (1998).

192. A. Lakshmanan, "Synthesis of gold nanorods of controlled aspect ratio to achieve maximum absorption wavelength tunability," in *Division of Bioengineering*(National University of Singapore, Singapore, 2010), p. 74.

193. T. K. Sau, and C. J. Murphy, "Seeded High Yield Synthesis of Short Au Nanorods in Aqueous Solution," Langmuir **20**, 6414-6420 (2004).

194. J. C. Y. Kah, K. Y. Wong, K. G. Neoh, J. H. Song, J. W. P. Fu, S. Mhaisalkar, M. Olivo, and C. J. R. Sheppard, "Critical parameters in the

pegylation of gold nanoshells for biomedical applications: An in vitro macrophage study," Journal of Drug Targeting **17**, 181-193 (2009).

195. "Covalent Coupling," in *TechNotes 205*, I. Bangs Laboratories, ed. (Bangs Laboratories, Inc., 2008), pp. 6-8.

196. H. Greg T, "Chapter 4 - Homobifunctional Crosslinkers," in *Bioconjugate Techniques (Second Edition)*(Academic Press, New York, 2008), pp. 234-275.

197. P. C. Chaumet, K. Belkebir, and A. Rahmani, "Coupled-dipole method in time domain," Opt. Express **16**, 20157-20165 (2008).

198. E. C. Hao, G. C. Schatz, R. C. Johnson, and J. T. Hupp, "Hyper-Rayleigh scattering from silver nanoparticles," The Journal of Chemical Physics **117**, 5963-5966 (2002).

199. D. Kobat, M. E. Durst, N. Nishimura, A. W. Wong, C. B. Schaffer, and C. Xu, "Deep tissue multiphoton microscopy using longer wavelength excitation," Opt. Express **17**, 13354-13364 (2009).

Author's Publications

Journal Publications

1) **N. K. Balla**, Elijah Y. S. Yew, C. J. R. Sheppard and P. T. C. So, "Coupled and Uncoupled Dipole Models of Nonlinear Scattering," Opt. Express (*In Press*).

2) J. B. Zhang, **N. K. Balla**, C. Gao, C. J. R. Sheppard, L. Y. L. Yung, S. Rehman, J. Y. Teo, S. R. Kulkarni, Y. H. Fu, and S. J. Yin, "Surface Modified Gold Nanorods in Two Photon Luminescence Imaging," Australian Journal of Chemistry 65, 290-298 (2012).

3) **N. K. Balla**, P. T. C. So, and C. J. R. Sheppard, "Second harmonic scattering from small particles using Discrete Dipole Approximation," Opt. Express 18, 21603-21611 (2010).

4) C. J. R. Sheppard, S. Rehman, **N. K. Balla**, E. Y. S. Yew, and T. W. Teng, "Bessel beams: Effects of polarization," Optics Communications **282**, 4647-4656 (2009).

5) C. J. R. Sheppard, **N. K. Balla**, and S. Rehman, "Performance parameters for highly-focused electromagnetic waves," Optics Communications **282**, 727-734 (2009).

Conference Presentations

1) **N. K. Balla**, and C. J. R. Sheppard, "Gold nanoparticles as second harmonic contrast agents for imaging live cells," in *Focus on Microscopy* (Osaka-Awaji, Japan, 2008).

2) **N. K. Balla**, and C. J. R. Sheppard, "Non-linear imaging of gold nanoparticles," in *Optics Within Life Sciences-10, Biophotonics Asia 2008* (Singapore, 2008).

3) **N. K. Balla**, P. T. C. So, and C. J. R. Sheppard, "Coupled Dipole Model for Nonlinear Scattering," in *Laser Science XXV* (Optical Society of America, 2009), p. LSWK5.

4) **N. K. Balla**, P. T. C. So, and C. J. R. Sheppard, "Comparison between coupled and uncoupled dipole models for second harmonic scattering," in *Focus on Microscopy* (Shanghai, China, 2010).

5) **N. K. Balla**, C. J. R. Sheppard, and P. T. C. So, "Multiphoton luminescence of gold nanorods upon excitation with wavelengths away from their absorption maxima," in *SPIE Photonics West*(San Francisco, California, USA, 2011).

6) **N. K. Balla**, P. T. C. So, and C. J. R. Sheppard, "Dipole Model for Nonlinear Scattering from Small Structures," in *ICMAT*(Singapore, 2011).

Manuscripts in preparation

N. K. Balla, P. T. C. So, and C. J. R. Sheppard, "Bio-inspired gold nanoparticles for second harmonic generation".

Patents

P. T. C. So, C. J. R. Sheppard and **N. K. Balla**, "Bio-inspired nano contrast agents for nonlinear generation microscopy and its applications" (*US Provisional Patent Application No. 61/597,418*)